O, Mg, and Si isotope distributions in the complex ultrarefractory CAI Efremovka 101.1: Assimilation of ultrarefractory, FUN, and regular CAI precursors

Jérôme Aléon, Johanna Marin-Carbonne, Kevin Mckeegan, Ahmed El Goresy

O, Mg, and Si isotope distributions in the complex ultrarefractory CAI Efremovka 101.1: Assimilation of ultrarefractory, FUN, and regular CAI precursors

Jérôme Aléon[1,2], Johanna Marin-Carbonne[3,4], Kevin D. McKeegan[3] and Ahmed El Goresy[5]

1- Centre de Science Nucléaire et de Science de la Matière, CNRS/IN2P3 – Université Paris-Sud UMR 8609, Bâtiment 104, 91405 Orsay Campus, France

2- Institut de Minéralogie, de Physique des Matériaux et de Cosmochimie, UMR 7590, Sorbonne Université, Museum National d'Histoire Naturelle, CNRS, Univ. Pierre et Marie Curie, IRD, 61 rue Buffon, 75005 Paris, France

3- Department of Earth, Planetary, and Space Sciences, University of California – Los Angeles, 595 Charles Young Drive East, Los Angeles, CA 90095-1567, USA

4- Laboratoire Magma et Volcans, UMR 6524, Univ. Lyon, Univ. Jean Monnet Saint-Etienne, CNRS, Univ. Clermont Auvergne, IRD, 23 rue du Dr Paul Michelon, 42023 Saint-Etienne, France

5- Bayerisches Geoinstitut, Universität Bayreuth, D-95440 Bayreuth, Germany

Submitted revised to *Geochimica et Cosmochimica Acta*

February 12, 2017

*Corresponding author : jerome.aleon@mnhn.fr

Abstract

Oxygen, magnesium, and silicon isotopic compositions in the mineralogically complex, ultrarefractory (UR) calcium-aluminum-rich inclusion (CAI) E101.1 from the reduced CV3 chondrite Efremovka confirm that E101.1 is a compound CAI composed of several lithological units that were once individual CAIs, free-floating in the solar protoplanetary disk. Each precursor unit was found to have had its own thermal history prior to being captured and incorporated into the partially molten host CAI.

Four major lithological units can be distinguished on the basis of their isotopic compositions. (1) Al-diopside-rich sinuous fragments, hereafter sinuous pyroxene, are ^{16}O-rich ($\Delta^{17}O \leq -20‰$) and have light Mg and Si isotopic compositions with mass fractionation down to -3.5‰/amu for both isotopic systems. We attribute these peculiar isotopic compositions to kinetic effects during condensation out of thermal equilibrium. (2) Spinel clusters are ^{16}O-rich ($\Delta^{17}O \sim -22‰$) and have Mg isotope systematics consistent with extensive equilibration with the host melt. This includes (i) δ^{25}Mg values varying between +2.6 ‰ and +6.5 ‰ close to the typical value of host melilite at ~+5‰, and (ii) evidence for exchange of radiogenic ^{26}Mg with adjacent melilite as indicated by Al/Mg systematics. The spinel clusters may represent fine-grained spinel-rich proto-CAIs captured, partially melted, and recrystallized in the host melt. Al/Mg systematics indicate that both the sinuous pyroxene fragments and spinel clusters probably had canonical or near-canonical ^{26}Al contents before partial equilibration. (3) The main CAI host ($\Delta^{17}O \leq -2‰$) had a complex thermal history partially obscured by subsequent capture and assimilation events. Its formation, referred to as the "cryptic" stage, could have resulted from the partial melting and crystallization of a ^{16}O-rich precursor that underwent ^{16}O-depletion and a massive evaporation event characteristic of F and FUN CAIs (Fractionated with Unknown Nuclear effects). Alternatively, a ^{16}O-rich UR

precursor may have coagulated with a ^{16}O-poor FUN CAI having ^{48}Ca anomalies, as indicated by perovskite, before subsequent extensive melting. The Al/Mg systematics ($2.4 \times 10^{-5} \leq (^{26}Al/^{27}Al)_0' \leq 5.4 \times 10^{-5}$, where $(^{26}Al/^{27}Al)_0'$ is a model initial ^{26}Al/^{27}Al ratio per analysis spot) are best understood if the FUN component was ^{26}Al-poor, as are many FUN CAIs. (4) A complete Wark-Lovering rim (WLR) surrounds E101.1. Its Mg and Si isotopic compositions indicate that it formed by interaction of the evaporated interior CAI with an unfractionated ^{16}O-rich condensate component. Heterogeneities in ^{26}Al content in WLR spinels ($3.7 \times 10^{-5} \leq (^{26}Al/^{27}Al)_0' \leq 5.7 \times 10^{-5}$) suggest that the previously reported age difference of as much as 300,000 years between interior CAIs and their WLRs may be an artifact resulting from Mg isotopic perturbations, possibly by solid state diffusion or mixing between the interior and condensate components.

The isotopic systematics of E101.1 imply that ^{16}O-rich and ^{16}O-poor reservoirs co-existed in the earliest solar protoplanetary disk and that igneous CAIs experienced a ^{16}O-depletion in an early high temperature stage. The coagulation of various lithological units in E101.1 and their partial assimilation supports models of CAI growth by competing fragmentation and coagulation in a partially molten state. Our results suggest that chemical and isotopic heterogeneities of unclear origin in regular CAIs may result from such a complex aggregation history masked by subsequent melting and recrystallization.

1. Introduction

As the first solids to have formed in our solar system, Calcium-Aluminum-rich Inclusions (CAIs) from chondritic meteorites provide a snapshot of the state of the solar system at its very beginning, probably as it was a dense protoplanetary disk, when the protosolar cloud envelope was still collapsing (Yang and Ciesla, 2012; Mishra and Chaussidon, 2014; Taillifet et al., 2014). CAIs are of interest for astrophysics because their conditions of formation correspond to those prevailing in the region of telluric planet formation, within the first 1 AU from the protosun. However, in spite of almost five decades of intense study, the astrophysical context of CAI formation is still debated (e.g., Shu et al., 1997; Itoh and Yurimoto, 2003; Boss et al., 2012; Yang and Ciesla, 2012; Taillifet et al., 2014). Particular CAI properties that would be potentially useful for constraining astrophysical models include (1) their ^{16}O and ^{26}Al isotopic anomalies (e.g., Itoh and Yurimoto, 2003; Mishra and Chaussidon, 2014; Aléon, 2016), (2) their high temperature gas-liquid-solid thermal histories (e.g., Richter et al., 2006; Shahar and Young, 2007), and (3) their redox state and the oxygen fugacity in the ambient medium where they formed (e.g., Simon et al., 2005, 2007; Grossman et al., 2008a; Paque et al., 2013). Up to now, most studies have been focused on one or two of these properties in isolation, however it has been recognized recently that many CAIs are compound objects that appear to have formed by aggregation of multiple precursors identified in the petrography (e.g., El Goresy et al., 2002; Aléon et al., 2007; MacPherson et al., 2012; Ivanova et al., 2015) or inferred from the isotopic record (e.g., Simon et al., 2017). Such CAIs most likely grew by coagulation-fragmentation either in the solid or in a partially molten state (Charnoz et al., 2015), thus adding complexity in the interpretation of differing petrological, chemical and isotopic properties in terms of astrophysical environments and processes that could produce mixing of refractory precursors.

94 The goal of our study is to use multiple tracers of the conditions of formation of CAIs
95 on a well characterized compound object in order to disentangle the various steps of its
96 formation history and to shed light on its precursors and on the astrophysical origin of the ^{16}O
97 and ^{26}Al isotopic anomalies. We focused on Efremovka 101.1 (hereafter E101.1), a CAI
98 previously studied in detail for its petrography, trace element and, to a limited extent, ^{26}Al
99 content by El Goresy et al. (2002). Notably, it contains several lithological units interpreted to
100 be CAI xenoliths trapped in a host inclusion. This petrographic stratigraphy provides an
101 opportunity to unravel the sequence of events that led to the CAI formation, growth, and
102 thermal processing, whereas in many large CAIs extensive melting has left only cryptic traces
103 of original formation events. We performed an *in-situ* systematic O, Mg, Si isotope study of
104 all lithological units coupled with complementary petrographic observations, in order to have
105 five isotopic tracers (O, Mg and Si mass fractionations, ^{16}O excesses and radiogenic ^{26}Mg
106 excesses, hereafter $^{26}Mg^*$) to study the thermal history of all components, their relationships,
107 and the interplay between thermal history and the record of the ^{16}O and ^{26}Al isotopic
108 anomalies.
109
110
111

2. Sample and Methods

2.1. CAI Efremovka 101.1

E101.1 is a ~1.6 mm diameter Compact Type A (CTA) inclusion (Fig. 1a) from the Efremovka reduced CV3 chondrite, previously studied by El Goresy et al. (2002) for mineralogy, petrography, and Rare Earth Elements (REE) abundances. Details of its lithological units, including those defined by El Goresy et al. (2002) are given in supplementary information (Fig. S1) and listed in Table 1. Table 1 also summarizes the terminology and CAI-related acronyms used throughout the manuscript. E101.1 is dominated by melilite of typical composition between $Åk_{25}$ and $Åk_{30}$ and it contains numerous clusters of coarse-grained spinel (Fig. S1A). E101.1 exhibits two major properties that are uncommon among CAIs: (1) the presence, in the same half of the inclusion, of several lithological units suggesting incorporation of xenoliths that were once individual CAIs free-floating in the nebula (El Goresy et al., 2002, Fig. S1B), some of which are associated with oxidized secondary phases, and (2) systematic ultrarefractory (UR) REE patterns associated with presence of an aluminous clinopyroxene containing up to 12.9 wt% Sc_2O_3 and up to 5.4 wt% ZrO_2. E101.1 is surrounded by a complete Wark-Lovering rim (WLR, Wark and Lovering, 1977) and exhibits portions of a forsterite-rich accretionary rim (AR, Krot et al., 2001) in its outer part (Fig. S1C). The UR-REE patterns are found throughout the inclusion in all lithological units including both rims and the xenoliths.

The most abundant xenoliths (more than 14) are made of sinuous fragments dominated by Al-diopside with chemistry similar to that often found in fine-grained spinel-rich CAIs or amoeboid olivine aggregates (Krot et al., 2004a,b) and locally including complex associations of fine-grained FeO-rich minerals such as andradite and hedenbergite with wollastonite (El Goresy et al., 2002, Fig. S1B). Fine-grained symplectite intergrowths of spinel, clinopyroxene

and perovskite, reminiscent of the reaction texture found in E49, another compound CAI from Efremovka (Aléon et al., 2007), are associated with the sinuous fragments and attributed to incorporation of small fine-grained CAI fragments (El Goresy et al., 2002).

Two areas dominated by melilite and surrounded by sinuous pyroxene fragments have been defined as subinclusions (El Goresy et al., 2002, Fig. S1B). The host inclusion contains several populations of Y- and Zr-rich perovskite grains distinguished by their ZrO_2/Y_2O_3 ratios. The largest perovskite grains are commonly associated with FeNi metal. The Sc-Zr-rich pyroxene is systematically associated with perovskite and/or metal and defines reaction rims with the host melilite (El Goresy et al., 2002). Several regions at the interface between sinuous pyroxene and host melilite present melt pockets with compositions roughly intermediate between diopside and gehlenite (Fig. S1D). These melt pockets contain dendritic crystals of nearly pure gehlenite (Fig. S1D) and were described as an impact glass (El Goresy et al., 2002), hereafter referred to as the quenched glass. The innermost part of the host CAI is hereafter designated as the core. Three perovskites of differing ZrO_2/Y_2O_3 ratio were analyzed for Ca and Ti isotopes and show both excesses and depletions in ^{48}Ca ($-7.5‰ \leq \delta^{48}Ca \leq +9.8‰$) but, remarkably, all have $\delta^{50}Ti \approx 0‰$. This unusual property is also found in FUN-type (Fractionated with isotopic anomalies of Unknown Nuclear origin) and hibonite-rich CAIs from Murchison (Kööp et al., 2018). The three analyzed perovskite belong to three differing ZrO_2/Y_2O_3 populations and their $\delta^{48}Ca$ range is comparable to that of the FUN-type hibonites, apart from one having a $\delta^{48}Ca$ value of +43‰ (Kööp et al., 2018). El Goresy et al. (2002) reported early Mg isotopes measurements in spinel and melilite with a ~ 1‰ precision (1σ) and in anorthite with a ~4 to ~8‰ precision (1σ). Their Al/Mg systematics yielded a slightly sub-canonical isochron of slope $^{26}Al/^{27}Al_0 \sim 4.3 \times 10^{-5}$ in the sinuous fragments, scattered initial $^{26}Al/^{27}Al$ ratios in the host melilite and little to no ^{26}Mg excesses in anorthite,

thus suggesting partial isotopic re-equilibration during or after ^{26}Al decay (El Goresy et al., 2002).

2.2. Petrographic analyses

Petrographic analyses were done using various electron probes and scanning electron microscopes (SEM) for comparison with isotopic analyses in the same phases. Maps of the distributions of Mg, Al, and Si in melilite were obtained using wavelength dispersive spectroscopy (WDS) with the Cameca SX5 and SX100 electron microprobes at the CAMPARIS facility in the Pierre et Marie Curie University in Paris. Additional chemical analyses of melilite within 10 μm of oxygen isotope analyses pits were obtained with the SX100 electron probe of the CAMPARIS facility. The small extent of some gehlenitic regions, notably around spinel, compared to the spot size of O isotopes may lead to artificial discrepancies in the relationship between melilite chemistry and O isotopes in some cases. To minimize this effect, the Åk content was determined from the Åk map in the exact location of the SIMS spots and this Åk content was preferred over the spot analyses in these cases with strong chemical gradients (Fig. S2). All electron probe analyses are available as supplementary information. Backscattered electron (BSE) images of ion microprobe crater pits, were obtained using the SEMs at the University of California Los Angeles (UCLA) and in the Geosciences Paris Sud (GEOPS) laboratory at the Orsay University, and with the field emission gun SEM (FEG-SEM) in the Geology department at the Ecole Normale Superieure (ENS) in Paris.

2.3. Ion microprobe analysis of O, Mg, and Si isotopes

All isotopic analyses were conducted using the Cameca IMS 1270 ion microprobe at UCLA in two sessions for O isotopes, one session for Mg isotopes, and two sessions for Si isotopes (Fig. 1b). Issues related with instrumental biases such as differences in instrumental mass fractionation (IMF) due to chemical variations in the target (matrix effects) and analyses overlapping on different mineral phases are discussed in supplementary information. Uncertainties arising from these effects were taken into account and untrusted results were not considered in the discussion.

2.3.1 Oxygen isotopes

Oxygen isotope ratios were measured in multicollection mode using a ~ 10 μm primary Cs^+ beam of ~0.2 nA. Negative ions of ^{16}O, ^{17}O and ^{18}O were detected on an off-axis Faraday cup (FC), and on two electron multipliers (EMs, axial and an off-axis), respectively. The mass resolving power (MRP, defined as M/ΔM) was set at ~ 6500, largely sufficient to resolve the $^{16}OH^-$ interference at mass 17. The normal incidence electron gun was used for charge compensation. After a 30 s presputtering with a 0.5 nA beam, ^{16}O, ^{17}O and ^{18}O were counted for 30 cycles of 10 s at typical count rates of 5×10^7 counts per second (cps), 2×10^4 cps and 1×10^5 cps for ^{16}O, ^{17}O and ^{18}O respectively. Liquid nitrogen was used to keep the vacuum at ~ 1×10^{-9} Torr as a routine precaution but the plexiglas mount of E101.1 ensured limited outgassing. Data were corrected for IMF using a San Carlos olivine and a Burma spinel standard, which yielded similar IMF. All analyses were thus corrected with an average IMF. As a whole, matrix effects for O isotopes in the phases investigated here are negligible except for the silicate melt inclusion in metal and possibly for the FeO-rich silicates and the Sc-Zr-rich pyroxene (supplementary information). Results are reported using the standard δ-notation, where $\delta^{17,18}O = (^{17,18}O/^{16}O_{samp} - {}^{17,18}O/^{16}O_{SMOW}) / (^{17,18}O/^{16}O_{SMOW}) \times 1000$ with SMOW being the Standard Mean Ocean Water. Average 2σ uncertainties taking into account

internal precision and reproducibility on standards are 0.48‰ and 0.94‰ on $\delta^{18}O$ and $\delta^{17}O$, respectively. Deviations from the slope 0.52 terrestrial mass fractionation line are given as $\Delta^{17}O$ where $\Delta^{17}O = \delta^{17}O - 0.52 \times \delta^{18}O$. Mass fractionations are noted $\Delta^{18}O_{CCAM}$ and are calculated respectively as isotopic deviations from the classical slope 0.94 Carbonaceous Chondrite Anhydrous Minerals mixing line (Clayton and Mayeda, 1984) along a slope 0.52 line. They are given in ‰/atomic mass unit (‰/amu).

We obtained a total of 128 analyses, sampling most phases (melilite, spinel, forsterite, Al-diopside, FeO-rich assemblages, Sc-Zr-rich pyroxene, perovskite, impact glass, melt inclusion in metal, nepheline ± anorthite) in several lithological contexts including the host CAI, sinuous pyroxene fragments, subinclusions 1 and 2, WLR and AR. Two profiles starting from the rim were done toward the interior of the host CAI (profiles 1 and 2) (Fig. S1E). The core of the host CAI was also targeted, as well as two areas between the sinuous pyroxene fragments and the rim (areas 3 and 4) (Fig. S1E). Both spinel and melilite inside of and in proximity to spinel clusters (clusters 1 to 5) were measured (Fig. S1A); in these regions melilite is significantly more gehlenitic than the typical host melilite.

2.3.2. Magnesium isotopes

Magnesium isotopes were measured using a ~30 µm O^- primary ion beam of 12-15 nA: ^{27}Al and the three Mg isotopes (^{24}Mg, ^{25}Mg and ^{26}Mg) were detected as positive ions in multicollection mode by using four Faraday cups. The MRP was set at ~ 4200, sufficient to completely separate molecular and doubly charged ion interferences ($^{48}Ca^{2+}$ and $^{48}Ti^{2+}$). $^{27}Al^+$, $^{26}Mg^+$, $^{25}Mg^+$ and $^{24}Mg^+$ were counted for 20 cycles of 10 s after a 30 to 50 s presputtering for spinel, pyroxene and olivine and for 100 cycles for melilite analyses except for analyses 60, 61 and 71 to 78 (20 cycles).

Standards used for determination of the instrumental mass fractionation and elemental relative sensitivity factors were Burma spinel, a synthetic pyroxene glass with no ^{26}Mg excess (P0), olivine and pyroxene from San Carlos, and Madagascar hibonite. Measurements of standards were interspersed with sample analyses, thus defining 7 groups of data. For each group, standards data expressed as $1000 \times \ln[(^{25,26}Mg/^{24}Mg)_{measured})/(^{25,26}Mg/^{24}Mg)_{true}]$ were used to calculate an instrumental mass fractionation law, which was used to determine the ^{26}Mg excesses (noted $\delta^{26}Mg^*$) by difference with the expected ^{26}Mg due to mass fractionation only. This instrumental mass fractionation law was preferred to that resulting from CAI evaporation in nature (Davis et al., 2015) because the instrumental effects between the standards were found to be larger than the natural effects observed in E101.1, thus yielding a potentially larger source of uncertainty if improperly corrected. The inaccuracy resulting from this assumption is at most about 0.25‰ and is typically below 0.1‰ (Fig. S3). All isotopic results were subsequently reported in δ-notation as per mil deviations relative to the DSM3 terrestrial reference (Galy et al., 2003). Measurements as an unknown of a synthetic pyroxene glass having ~ 1‰ ^{26}Mg excess (P1) yielded an average ^{26}Mg excess of 1.071 ± 0.080 ‰ (2σ). Al/Mg ratios were determined from the $^{27}Al^+/^{24}Mg^+$ ratios corrected using the relative sensitivity factors (RSF) determined from Burma spinel (spinel), the P0 synthetic Al-Ti-pyroxene glass (Al-diopside, Sc-Zr-rich pyroxene, impact glass) and Madagascar hibonite (melilite). IMF for the $^{25}Mg/^{24}Mg$ ratios were calculated using Burma spinel for spinel analyses, the pyroxene P0 glass (or in one case the San Carlos pyroxene normalized to P0) for Al-diopside, Sc-Zr-rich pyroxene, impact glass and melilite and San Carlos olivine for forsterite. Burma spinel and P0 glass were previously measured relative to USNM forsterite, which composition relative to DSM3 was determined by Galy et al. (2003). We further assumed that San Carlos olivine has the same Mg isotopic composition as USNM forsterite. Given the Earth mantle origin of both olivines, the uncertainty resulting from this assumption

is much smaller than our analytical precision. In the absence of a proper melilite standard for Mg isotopes we initially assumed that hibonite could be used as a standard for the Al/Mg ratio of melilite, a reasonable approximation within uncertainties, and that the P0 glass could be used to determine the Mg isotopes IMF for melilite. Further matrix effect investigations indicate a 5 ± 0.5‰ matrix effect between P0 and Al-rich melilite for Mg isotopes, which was retroactively applied to the sample melilite data. The additional uncertainty due to this correction has been propagated and is included in the reported dataset. Al/Mg ratios for forsterite were not corrected for RSF but were close enough to 0 (average 0.015 ± 0.015, 2σ) to have negligible effects on isochron regressions. Still, we note that the Al^+/Mg^+ ratios on the San Carlos olivine were significantly lower than this (average 2.88 ± 0.06 × 10^{-4}, 2σ), suggesting that minor amounts of Al-rich material (e.g., Al-diopside) were incorporated in the analyses in agreement with SEM imaging of the AR. The precisions obtained for Mg isotopic ratios depend on the Mg content: 2σ errors for $\delta^{25}Mg$ incorporating both internal (within spot) and external reproducibility on standards range between 1.06 ‰ and 1.75 ‰ for melilite and glass, and between 0.37 ‰ and 0.89 ‰ for other minerals. 2σ errors on $\delta^{26}Mg^*$ range between 0.06 and 0.95 ‰, again with larger uncertainties for the Al-rich, Mg-poor phases.

We obtained a total of 85 measurements of Mg isotope ratios from spinel, Al-diopside, Sc-Zr-rich pyroxene, impact glass and melilite. Care was taken to sample the host inclusion, the sinuous pyroxene fragments, subinclusion 1, the WLR and AR as well as five different spinel clusters. Adjacent melilite was measured in 4 of the 5 spinel clusters. Whenever possible, Mg isotopes spots were located within 20 μm of the O isotope analysis pits for a direct comparison. For example, the Mg isotope profiles 1 and 2 were started from the rim and were made in parallel with the O isotope traverse (Fig. S1E).

2.3.3. Silicon isotopes

Silicon isotopes were measured in multicollection mode as negative ions with a ~ 20 µm Cs^+ primary ion beam of 1-1.7 nA. $^{28}Si^-$ and $^{30}Si^-$ were detected simultaneously on two Faraday cups. $^{27}Al^-$ was measured as well as a check on the composition of the analyzed mineral. The mass resolving power was set at 2400, sufficient to separate the $^{29}SiH^-$ interference at mass 30. The normal incidence electron gun was used for charge compensation. Typical secondary ion intensities for $^{28}Si^-$ ranged between 4×10^7 cps in melilite to 7×10^7 cps in olivine. Si isotopic compositions are reported as $\delta^{30}Si$ per mil deviations relative to the NBS 28 international reference. With such conditions, a Poisson counting statistic $\leq \pm 0.1‰$ is obtained after a few minutes integration (30 cycles of 5 s acquisition time and 30 s of presputtering). The IMF was corrected by using San Carlos olivine, P0 pyroxene glass, San Carlos pyroxene and new melilite standards specifically prepared for Si isotope analyses (Marin-Carbonne et al., 2012). Matrix effects are particularly large for silicon isotopes in melilite (Knight et al., 2009), which ionize poorly and have large IMF. This matrix effect is dependent on the Al content and was calibrated using the three melilite standards ($Åk_{10}$, $Åk_{80}$ and a zoned crystal with Åk content ranging between 15 and 70 mol%) and the method described in Marin-Carbonne et al. (2012). Possible matrix effects in pyroxene remained within analytical uncertainty (supplementary information). Typical errors after all corrections including propagation of internal precision and external reproducibility determined on standards are 0.4-0.6 ‰ (2σ).

The mass fractionation in ‰/amu is expressed as *F*Si, where $F\text{Si} = \delta^{30}\text{Si} / 0.501$ where the factor 0.501 is the $(M^{29}Si\text{-}M^{28}Si)/(M^{30}Si\text{-}M^{28}Si)$ ratio, where M^xSi is the exact mass of the ^xSi isotope. Knight et al. (2009) report a mass fractionation factor of 0.518 ± 0.006 between $\delta^{29}Si$ and $\delta^{30}Si$ in evaporated CMAS (Ca, Mg, Al, Si) glasses analogs of CAIs, so that *F*Si as defined here is not strictly identical to $\delta^{29}Si$, however the difference is small with regard to our uncertainties so that it does not affect any interpretation and *F*Si can be compared with

309 δ^{25}Mg. Si isotopic analyses were acquired for 60 spots, preferentially in the vicinity of O and
310 Mg isotope crater pits in order to allow as much intercomparison between the various isotopic
311 systems as possible (within 20-30 μm). For example, Si isotope traverses were made in
312 parallel with the O and Mg isotope profiles (Fig. S1E). Analyzed phases include olivine,
313 pyroxene and melilite from different petrographic contexts of E101.1, including the host
314 inclusion, sinuous pyroxene fragments, subinclusion 1, areas 3 and 4, and the WLR and AR.
315

316 # 3. Results

317

318 *3.1. Petrographic observations*

319

320 New electron probe analyses indicate that in spite of a typical melilite composition in
321 the $Åk_{20}$-$Åk_{30}$ range (El Goresy et al., 2002), melilite can reach nearly pure gehlenite
322 composition (down to $Åk_3$) in contact with spinel, notably near the WLR as in other CAIs
323 (e.g., Fahey et al., 1987; Goswami et al., 1994; Toppani et al., 2006; Aléon et al., 2007;
324 Kawasaki et al., 2012), but around spinel clusters in the interior as well (Fig. S4). These
325 interior spinel clusters correspond to the end of spinel trails reaching the rim of the inclusion.
326 The electron probe mapping of Mg further shows that these spinel trails are systematically
327 associated with aluminous melilite thus defining continuous to semi-continuous channels of
328 aluminous melilite between the spinel clusters and the edge of the CAI (Fig. 2). This is
329 notably the case of spinel clusters 1, 2 and 4 (Fig. 2). Being closer to the rim, cluster 3 is
330 embedded in such a channel. Spinel clusters in the upper part of subinclusion 1 are also
331 located at the end of such trails (Figs. 1 and 2). Cluster 5 and the smaller clusters in the lower
332 left part of Figure 1 also define a swarm of spinel associated with Al-rich melilite and
333 connected to the edge of the CAI, although not as continuous as the upper trails (Fig. 2). Two
334 of these small clusters are labeled as clusters 6 and 7 (Fig. 3). Detailed SEM examination of
335 the spinels throughout the inclusion and especially of those connected to the rim via
336 gehlenitic melilite reveals numerous signs of spinel resorption, which notably include (1)
337 rounded anhedral crystal shapes (Fig. 3a,b), (2) embayments (Fig. 3a-c), (3) a rim around
338 spinel consisting of Al-, Ti-clinopyroxene ± spinel symplectite, locally with perovskite
339 inclusions (Fig. 3). A mineralogical continuum is observed in these rims from pyroxene +
340 abundant microspinel to pyroxene only to pyroxene + perovskite. The Ti content of the

pyroxene can be used to map the symplectite (Fig. 3d). This symplectite is similar to that previously described in E49, another compound CTA inclusion from Efremovka (Aléon et al., 2007). Where the surrounding rim consists of clinopyroxene only, it is strongly reminiscent of the boundary clinopyroxene described around spinel in Type B CAIs and in the mantles of Type B1 CAIs (Paque et al., 2009). This rim is also similar in textural relationship to the Sc-Zr-rich pyroxene rims around perovskite and metal grains (Fig. 4, El Goresy et al., 2002). As in the case of spinels, the perovskite rimmed by the Sc-Zr-rich pyroxene commonly shows embayments and anhedral shapes. FeNi metal is commonly associated with perovskite and rimmed by the Sc-Zr-rich pyroxene. It is predominantly high Ni taenite (35-51 at% Ni) but high Co kamacite (up to 8 at% Co) is also found, usually in heterogeneous grains (see supplementary informations). One grain contains 5-6 at% platinum group elements. Most grains contain inclusions of Fe-V-oxides and Ca-phosphates near their periphery. A troilite inclusion is found once. Three Si-rich glass inclusions were found in one of the metal grains (Fig. 4a).

Although E101.1 was initially described as mostly unaltered, we found nepheline associated with anorthite in replacement of melilite, notably in the vicinity of perovskite + metal nodules (Fig. 4).

3.2. Oxygen isotopes

Oxygen isotope ratios in E101.1 (Table S1) plot along the Carbonaceous Chondrites Anhydrous Minerals mixing line (Clayton and Mayeda, 1984) and span the whole range between the typical ^{16}O-rich composition of spinel in CAIs ($\Delta^{17}O \sim -22$ ‰) and a sub-terrestrial ^{16}O-poor composition (up to $\Delta^{17}O \sim -2$ ‰, Fig. 5a).

Spinel and accretionary rim forsterite are uniformly ^{16}O-rich with $\Delta^{17}O \leq -20.5$ ‰. The isotopic composition of melilite varies from significantly enriched in ^{16}O ($\Delta^{17}O$ down to -19.8 ‰ in the WLR, Fig. 5c) to relatively ^{16}O-poor ($\Delta^{17}O$ up to -1.9 ‰). The most ^{16}O-rich melilite is systematically gehlenitic melilite associated with spinel (Fig. 6), although the reverse is not systematic. This is true for melilite from the WLR and also for gehlenitic melilite associated with coarse-grained spinel clusters in the interior (Fig. 6b). Interestingly, the Åk content of melilite associated with spinel clusters define a trend similar to that in melilite as a function of distance to WLR spinel in profiles 1 and 2 (Fig. 6c). Examination of melilite composition in the various petrographic areas indicates that different regions in the interior of the CAI have statistically different O isotopic compositions (weighted mean ranging from $\Delta^{17}O = -5.01 \pm 0.27$ ‰ to -8.64 ± 0.43 ‰, 2σ, Table 2). The most ^{16}O-enriched regions are encountered in subinclusion 1 and areas 3 and 4, all in the vicinity of the sinuous pyroxene fragments. The reduced χ^2 for $\Delta^{17}O$ within each region ranges from 1.8 to 4.7. By contrast, the average $\Delta^{17}O$ value over all standard analyses is -0.18 ± 0.16 (2σ) with a reduced χ^2 of 1.9. This suggests that melilite in individual regions is not fully homogenized (Table 2). A small amount of mass fractionation relative to the CCAM line (weighted mean $\Delta^{18}O_{CCAM} = 2.33 \pm 0.16$ ‰/amu, 2σ) is observed in the ^{16}O-poor melilite but not in the ^{16}O-rich melilite (weighted mean $\Delta^{18}O_{CCAM} = 0.76 \pm 0.57$ ‰/amu, 2σ, Fig. 7). The amplitude of this effect suggests it is not of instrumental origin (supplementary information). The most ^{16}O-depleted compositions (-2.8 ‰ $\leq \Delta^{17}O \leq -1.9$ ‰) were observed in melilite in the outer portion of profile 1 (see below) and also in (1) nepheline, (2) Sc-Zr-rich pyroxene and (3) one glass inclusion in metal (Fig. 5d).

The Sc-Zr-rich pyroxene (-3.26 ‰ $\leq \Delta^{17}O \leq -2.23$ ‰) appears to be mass fractionated similarly to the ^{16}O-poor melilite (weighted mean $\Delta^{18}O_{CCAM} = 2.49 \pm 0.75$ ‰/amu, 2σ, Fig. 7) but the ^{16}O-rich pyroxenes (Al-rich diopside from the sinuous fragments and pyroxene from

390 the WLR) are not appreciably mass fractionated (weighted mean $\Delta^{18}O_{CCAM}$ = 0.64 ± 0.29
391 ‰/amu, 2σ, Fig. 7). Again, this suggests that the apparent mass fractionation is not of
392 instrumental origin although a matrix effect between diopside and Sc-Zr-rich pyroxene cannot
393 be excluded (supplementary information). Many analyses of the Al-diopside in the sinuous
394 fragments overlap with FeO-rich silicates and show intermediate ^{16}O-excess (Fig. 5b)
395 between pure Al-diopside ($\Delta^{17}O \leq$ -20 ‰) and FeO-rich silicates ($\Delta^{17}O \geq$ -5 ‰). Pure Al-
396 diopside analyses show a correlation between diopside chemistry and ^{16}O-enrichment, with
397 the most refractory pyroxene (with highest Al_2O_3 and lowest SiO_2 contents) being also the
398 most ^{16}O-rich (Fig. 8).
399 Perovskite was found to be variably enriched in ^{16}O (-19 ‰ $\leq \Delta^{17}O \leq$ -9 ‰) but the
400 ^{16}O-excess does not appear to be related to the ZrO_2/Y_2O_3 ratio, which was used by El Goresy
401 et al. (2002) to characterize several populations of perovskite (Fig. 9).
402 Minerals in the WLR and the forsterite-rich accretionary rim are rich in ^{16}O as often
403 observed in CAIs (Krot et al., 2002; Yoshitake et al., 2005; Aléon et al., 2007; Bodénan et al.,
404 2014). Apart from one analysis of WLR pyroxene ($\Delta^{17}O$ = -15.3 ± 0.7 ‰), a few analyses
405 with intermediate composition (-18 ‰ $\leq \Delta^{17}O \leq$ -13 ‰) correspond to WLR melilite and
406 pyroxene + anorthite nodules in the AR.
407 Finally the quenched glass appears to have oxygen isotopic compositions between
408 those of the host melilite and Al-diopside from the sinuous pyroxene fragments (-14 ‰ ≤
409 $\Delta^{17}O \leq$ -10 ‰).
410
411 *3.3. Magnesium isotopes*
412
413 *3.3.1.Initial $^{26}Al/^{27}Al$ ratios.*
414

A trend of increasing $\delta^{26}Mg^*$ with $^{27}Al/^{24}Mg$ is observed but a single well-defined isochron cannot be identified (Fig. 10, Table S2). A spread in $\delta^{26}Mg^*$ beyond analytical uncertainties is observed in melilite and spinel (Fig. 10). In order to evaluate the spread in excess ^{26}Mg and its consequence on the ^{26}Al distribution in the inclusion and on chronology, model initial $^{26}Al/^{27}Al$, denoted $(^{26}Al/^{27}Al)_0'$ ratios have been calculated for individual data points. The $(^{26}Al/^{27}Al)_0'$ ratio is defined as the slope of an isochron going through a given analysis and through the origin.

In the interior, spinels from subinclusion 1, cluster 1 and cluster 5 have $(^{26}Al/^{27}Al)_0'$ ratios consistent with a canonical ratio (i.e., 5.23×10^{-5}, Jacobsen et al., 2008) within error (weighted means of $(5.0\pm0.4) \times 10^{-5}$, $(5.3\pm0.9) \times 10^{-5}$, $(5.6\pm0.4) \times 10^{-5}$, 2σ, respectively, Table 2), but cluster 2 has a distinctly supracanonical weighted mean ($(7.3\pm0.9) \times 10^{-5}$, 2σ, Table 2). Near the CAI periphery, cluster 3 has a subcanonical $(^{26}Al/^{27}Al)_0'$ ratio of $(3.6\pm1.2) \times 10^{-5}$ (2σ, Table 2).

Individual $(^{26}Al/^{27}Al)_0'$ ratios in melilite range between $(5.4\pm0.2) \times 10^{-5}$ and $(2.4\pm0.5) \times 10^{-5}$ (2σ) suggesting secondary perturbations owing to Mg diffusion and isotope exchange in an initially canonical melilite. No clear difference can be observed between different regions in the CAI (Fig. 10), with similar average and spread in $(^{26}Al/^{27}Al)_0'$ ratios of 3.7±0.5, 4.7±0.6, 4.1±0.9, 4.2±0.3, 4.0±0.5, 3.4±0.7, 4.0±0.7 for area 3, area 4, subinclusion 1, core, melilite in the vicinity of spinel clusters, profile 1 and profile 2, respectively (weighted mean given in units of 10^{-5}; uncertainties are 1 standard deviation here rather than 2 standard errors to take into account heterogeneities in melilite within individual areas and to emphasize the similarity of the ratios). In subinclusion 1 and spinel clusters 1 and 5, melilite associated with spinel have comparable $(^{26}Al/^{27}Al)_0'$ ratios between 4.1×10^{-5} and 4.3×10^{-5}, while associated spinels have higher ratios consistent with the canonical ratio (Table 2). Only

439 melilite associated with sub-canonical spinel (cluster 3) has a $(^{26}Al/^{27}Al)_0'$ ratio comparable
440 to that of the associated spinel ((3.3±0.3) × 10^{-5} and (3.6±1.2) × 10^{-5}, respectively, 2σ, Table
441 2). This corresponds to systematic sub-canonical slopes and elevated intercepts in Al/Mg
442 isochrons, with the highest intercept for cluster 2 (Fig. 11), except for cluster 3 where the
443 intercept is consistent with 0. Regressions for subinclusion 1, cluster 1 and cluster 5 are
444 identical within error (Fig. S5).
445 Due to large uncertainties, all estimates of the initial $^{26}Al/^{27}Al$ ratio of the sinuous
446 pyroxene are consistent with the canonical ratio (Fig. 10) and with the average melilite value
447 at the 2σ level.
448 In the WLR, $(^{26}Al/^{27}Al)_0'$ ratios range from canonical ((5.7±0.4) × 10^{-5}) to distinctly
449 subcanonical ((3.7±0.5) × 10^{-5}) in spinel. If both spinel and pyroxene are considered together
450 a regression yields a slope of (4.5±0.8) × 10^{-5} (2σ), which becomes (4.8±0.5) × 10^{-5} (2σ) if
451 forced through the origin. This is identical to the weighted mean of $(^{26}Al/^{27}Al)_0'$ ratios of
452 (4.8±0.2) × 10^{-5} (2σ, Table 2). Given that variations in spinel should affect the determination
453 of the slope, we also investigated the $^{26}Al/^{27}Al$ systematics of the WLR without spinel.
454 Pyroxene data are individually consistent with the canonical ratio and a regression yields a
455 slope of (4.1±3.0) × 10^{-5} (2σ), which becomes (6.0±0.9) × 10^{-5} (2σ) if forced through the
456 origin.
457 The weighted mean of ^{26}Mg excesses ($\delta^{26}Mg^*$) in accretionary rim forsterite is 0.06 ±
458 0.04 ‰ (2σ), which indicates a small but significant excess of ^{26}Mg. The high Al^+/Mg^+ ratios
459 compared to San Carlos olivine suggest Al-rich contamination in the analysis spot, so that this
460 excess is probably intermediate between that of pure olivine and that of the bulk AR. It
461 compares well with previous values in bulk AOA and Fo-rich AR in CAIs (Larsen et al.,
462 2011) as well as with initial $\delta^{26}Mg^*$ in AOAs calculated from internal isochrons (MacPherson
463 et al., 2012; Mishra and Chaussidon, 2014).

464

465 *3.3.2. Mass fractionation.*

466

467 δ^{25}Mg values vary between 6.7±1.8 ‰ and -4.7±0.7 (2σ, Table S2). This ~ 12‰ range
468 is unusual in normal (i.e., non-FUN) CAIs, which commonly have more homogeneous
469 compositions (e.g., Simon et al., 2005; Kita et al., 2012; Bullock et al., 2013). The Mg
470 isotopic compositions of the E101.1 lithological units span a large range between that of light
471 hibonite CAIs from CM chondrites (δ^{25}Mg values as low as -7‰, Liu et al., 2012) and that of
472 classical igneous Type A and B CAIs enriched in heavy isotopes (-1‰ ≤ δ^{25}Mg ≤ +11‰,
473 Davis and Richter, 2014).

474 The most negative values are systematically found in the sinuous pyroxene fragments
475 with δ^{25}Mg values between -4.7 and -2.4 ‰. In most of the inclusion, melilite has positive
476 values between 1.9‰ and 6.5‰ with a mean value around ~ +5‰. Intermediate δ^{25}Mg values
477 are found in melilite in areas 3 and 4 and in the subinclusion 1, all in close vicinity of the
478 sinuous pyroxene (-1.5‰ ≤ δ^{25}Mg ≤ +2.1‰). Spinels in clusters 1 to 4 have positive values
479 comparable to that of the associated melilite and close to the typical host melilite value (Fig.
480 12, Table 2). In cluster 5, spinels have lower δ^{25}Mg values (~ 2.6‰). One associated melilite
481 has a comparable low value (3.7 ‰) whereas another melilite is more typical of the host
482 melilite (6.1‰). Both spinels and melilite in subinclusion 1 have near 0‰ δ^{25}Mg values. In
483 the WLR, the δ^{25}Mg values of pyroxene range between -1.2‰ and positive values
484 approaching those of the interior melilite at + 3‰. WLR spinel and forsterite from the AR all
485 have δ^{25}Mg values around 0 ± 1.5‰.

486

487 *3.4. Silicon isotopes*

488

The δ^{30}Si values in E101.1 span a very large range, from -9.0 ± 1.3 to +19.9 ± 1.3, which corresponds to *F*Si values between -4.5 ± 0.6 ‰/amu and +10.0 ± 0.6 ‰/amu where errors correspond to 2σ uncertainties (Table S3). This ~ 15‰/amu range is comparable to that of δ^{25}Mg or slightly larger. Again it is highly unusual in non-FUN CAIs, which commonly have a more homogeneous composition (Shahar and Young, 2007; Bullock et al., 2013). The lightest Si isotopic composition (most negative *F*Si values) corresponds to the strongest negative mass fractionation ever reported for a CAI. By contrast, the heaviest Si isotopic compositions of E101.1 reach those of the heavy (although not the heaviest) FUN CAIs (having δ^{29}Si values commonly larger than +5 ‰, Davis and Richter, 2014). This corresponds to a positive mass fractionation even stronger than that for Mg.

As is the case for Mg isotopes, the most negative *F*Si values are also found in the sinuous pyroxene fragments (-4.5 ± 0.6 ‰/amu to -2.4 ± 0.6 ‰/amu). *F*Si values in the host melilite are by contrast systematically positive and range between +3.9 ‰/amu and +8.5 ‰/amu with an average and representative value at +5.9‰/amu, approaching the transition between normal and FUN CAIs (Davis and Richter, 2014). Melilite in areas in close vicinity to the sinuous pyroxene fragments (sub1, area 3 and 4) have *F*Si values intermediate between those of the host melilite and those of the sinuous pyroxene, although they can reach the host melilite values (+1.2 ±0.4 ‰/amu ≤ *F*Si ≤ +8.8 ± 0.6 ‰/amu). AR olivines have slightly negative *F*Si values within 2σ errors of the average value (*F*Si between -1.9 ±0.4 ‰/amu and -0.5 ± 0.6 ‰/amu, average *F*Si= -1.2 ± 0.6‰/amu) and pyroxenes in the WLR have *F*Si values ranging between those of the AR and those of the interior melilite (-0.3±0.3 ‰/amu ≤ *F*Si ≤ +6.2 ± 0.6 ‰/amu) with one value at +10.0 ± 0.6 ‰/amu. The latter analysis corresponds to Ti-rich pyroxene finely intergrown with spinel, interior to the Al-diopside layer of the WLR. It must be treated with caution as the analysis overlapped significantly with spinel.

514

515 *3.5. Profiles*

516

517 Possible isotopic variations between the interior of the CAI and its outer part were
518 investigated with two profiles, starting from the rim toward the interior, and with the areas 3
519 and 4 (see Fig. 1A). Due to large ion beam spot sizes compared to the usual WLR layers, rim
520 analyses were acquired where the thickness allowed it. No transect was done within the WLR
521 and the profiles started inside the spinel layer without including the WLR. The chemical
522 composition of melilite shows large variations between $Åk_{20}$ and $Åk_{40}$ (profile 1, Fig. 13a) in
523 the CAI interior, (also visible in the Mg map; Fig. 2). In the outermost 200 μm the
524 composition of melilite is rather homogeneous at ~$Åk_{25}$, except in the vicinity of the rim,
525 where the Åk content suddenly drops towards nearly pure gehlenitic composition. This drop
526 occurs ~30 μm inward from the WLR in profile 1 and ~70 μm inward from the rim in profile
527 2 (Fig. 13a). This enrichment in gehlenite toward the rim is commonly observed in Type A
528 CAIs (e.g., Fahey et al., 1987; Goswami et al., 1994; Aléon et al., 2007; Simon et al., 2011,
529 2016; Katayama et al., 2012, Kawasaki et al., 2012, 2017).

530 The change in Mg content of melilite along profiles 1 and 2 is correlated with an
531 isotopic evolution. Along profile 1, the δ^{25}Mg value is around +4.5‰ in the interior of the
532 CAI, where melilite is the most magnesian. In the $Åk_{25}$ zone, it is rather homogeneous around
533 + 5.5‰ until the point where the Åk content drops (Fig. 13b). Unfortunately, it was not
534 possible to acquire a Mg isotope analysis in the 30 μm region immediately inside the WLR
535 without overlapping with spinel. However, because the point where the Åk content drops in
536 profile 2 is further away from the rim at ~70 μm toward the interior, several analyses were
537 obtained in this particular region. In the interior part of profile 2, the δ^{25}Mg value barely
538 decreases from +6.7‰ down to +5.1‰ until the 70 μm boundary (Fig. 13b). In the outer 70

539 μm, it decreases from + 5‰ down to + 2‰ (Fig. 13b). Such an evolution from heavy,
540 positive values in the interior toward values closer to 0 has already been observed in some
541 Type A CAIs (Goswami et al., 1994; Simon et al., 2005), although the reverse has also been
542 observed (e.g., CAI Leoville 144A, Simon et al., 2005). Areas 3 and 4 also show an isotopic
543 evolution with distance but are generally much closer to 0, with δ^{25}Mg values evolving from
544 about +2‰ down to ~0‰ toward the rim (Fig. 13b).

545 This coupled chemical - stable Mg isotopic evolution of melilite is also roughly
546 associated with a radiogenic Mg isotopic evolution. $(^{26}Al/^{27}Al)_0'$ ratios are scattered between
547 $\sim 4 \times 10^{-5}$ and $\sim 2 \times 10^{-5}$ in the interior of the CAI but increase toward the rim, notably
548 outward of the 70 μm limit in profile 2, to reach roughly canonical values near the rim (Fig.
549 13c) as also found by Simon et al. (2005) for CAIs with supracanonical ratios in their interior.

550 By contrast, the Si isotopic composition does not show any appreciable evolution with
551 distance from the interior to the rim (Fig. 13d). Profiles 1 and 2 are flat with homogeneous
552 *F*Si values typical of the interior CAI near ~+6‰/amu. Areas 3 and 4 also have seemingly
553 homogeneous compositions but at different *F*Si values near +3‰ (area 4) and +1‰ (area 3),
554 although only 1 value without significant overlap is available for the latter.

555 Similarly to Si, the O isotope profiles do not show clear trends along the profile. Δ^{17}O
556 values along profile 1 cluster around -6‰ with a significant spread as discussed above. Still,
557 the outermost two analyses show Δ^{17}O values near -2‰ near the rim (Fig. 13e). Profile 2
558 shows comparable values (Fig. 13e) but a slight decrease in Δ^{17}O is observed toward the
559 exterior before increasing again in the outer 70 μm. This increase and the least negative
560 values of profile 1 may indicate a systematic increase in Δ^{17}O near the rim. Such an increase
561 in Δ^{17}O is uncommon in Type A CAIs (e.g., Aléon et al., 2007; Kawasaki et al., 2012; Simon
562 et al., 2016) but has been observed previously (e.g., CAI Allende A37, Simon et al., 2011,
563 2016). Areas 3 and 4 show significantly lower Δ^{17}O values (near -8‰, see above), again with

564 some scatter. Contrary to profiles 1 and 2, $\Delta^{17}O$ values tend to decrease toward the exterior in
565 area 3 and 4. The mass fractionation relative to the CCAM line is highly variable and does not
566 show any systematic trends (Fig. 13f).
567

4. Discussion

The coupled isotopic and petrologic observations summarized above point to a complex origin for E101.1. Here, we present model calculations to determine the nature of the E101.1 precursor materials based on observed isotopic compositions. The models reported in sections 4.1 and 4.2 are depicted schematically in Figure. 14. Theoretical endmember components are listed in Table 1; their compositions are given in supplementary information (Table S4).

4.1. Origin of the sinuous pyroxene

4.1.1. Thermal history of the sinuous pyroxene

The very light Si and Mg isotopic compositions of the sinuous pyroxene fragments with δ^{25}Mg and *F*Si values both of about -3.5‰, are unusual in igneous CAIs, which are commonly enriched in heavy isotopes due to Rayleigh distillation during evaporation (e.g., Clayton et al., 1988; Grossman et al., 2008b). These compositions are drastically different from those of the surrounding host CAI, which is enriched in heavy Si and Mg isotopes. This is indicative of a strong degree of disequilibrium and confirms the hypothesis inferred from textural and petrographic analysis (El Goresy et al., 2002) that the sinuous pyroxene lithologies are indeed xenolithic fragments that were captured by the main host and escaped complete assimilation.

Isotopically light values of Mg have already been reported for many platy hibonite crystals (PLACS) from the Murchison and Paris CM chondrites, with δ^{25}Mg values occasionally reaching -7‰ and possibly as low as -10‰ (Fahey et al., 1987; Ireland, 1988,

593 1990; Sahijpal et al., 2000; Liu et al., 2012, Kööp et al. 2016a,b). The proposed interpretation
594 for such low δ^{25}Mg values is kinetic isotopic effects during condensation (Liu et al., 2012), at
595 a temperature lower than the equilibrium condensation temperature. The competition between
596 kinetic and equilibrium effects has been investigated theoretically for the evolution of Mg
597 isotopic composition during condensation of forsterite (Richter, 2004) and experimentally for
598 the evaporation of a melt of CAI composition (Richter et al., 2007). The amount of Mg
599 isotope mass fractionation due to kinetic effects can reach -10 to -14‰/amu, depending on
600 temperature. A contribution of Mg and Si condensed under thermal disequilibrium thus
601 appears to be a possible explanation for the negative δ^{25}Mg and *F*Si of the sinuous fragments.
602 A key parameter in the extent of the kinetic effects is the ratio between the
603 condensation timescale and the timescale for the temperature change of the ambient medium
604 (Richter, 2004). If the condensation is much faster than the change in ambient temperature,
605 then condensation mostly proceeds at equilibrium and the isotopic fractionation is negligible
606 in the considered range of temperatures. By contrast, if the change in ambient temperature is
607 faster than condensation, then condensation proceeds at a temperature lower than expected
608 (undercooling) and large kinetic isotopic fractionation effects are to be expected (Richter,
609 2004; Simon and DePaolo, 2010; Simon et al., 2017). Kinetic isotopic fractionation during
610 condensation thus appears as a possible explanation for the negative δ^{25}Mg and *F*Si values of
611 the sinuous pyroxene if condensation proceeded during a rapid temperature drop (Richter et
612 al., 2004) allowing a significant degree of undercooling (Simon and DePaolo, 2010; Simon et
613 al., 2017). Either the sinuous pyroxene contains a small fraction of a strongly fractionated
614 component or a large fraction of a component having a few per mil fractionation (e.g. a few
615 degrees of undercooling as calculated for Ca and Ti isotopes, Simon et al., 2017). Such a
616 temperature drop could be due to fast removal by rapid transport of condensing precursors
617 from a region of high temperature in the protoplanetary disk, where Mg and Si start to

618 condense in solids, to a region where the ambient temperature is suitable for pyroxene
619 condensation. Alternatively rapid temperature fluctuations are required.

620 Interestingly, the sinuous pyroxene exhibits the UR REE pattern typical of E101.1,
621 wherein the relative abundances of REEs are controlled by their respective volatilities, the
622 most refractory REEs being the most abundant. The UR REE pattern is established by
623 condensation as solid solutions in the most refractory minerals that can accommodate REEs,
624 namely ZrO_2, Y-oxides, hibonite and perovskite. As hibonite is the first major condensate, the
625 UR pattern is established in the first few degrees below the onset of hibonite condensation
626 (Simon et al., 1996; Davis and Richter, 2014). Such REE patterns can only be preserved in
627 the highest temperature condensate (hibonite ?) if it is rapidly removed from the gas. One may
628 expect a significant amount of thermal disequilibrium during this removal of the UR-carrier
629 from the ambient gas, which possibly accounts for Ca and Ti isotopic mass fractionation
630 (Davis et al., 2018; Simon and De Paolo, 2010; Simon et al., 2017). Whether it also accounts
631 for the negative Mg and Si isotopic fractionation is unclear. A separate condensation event
632 may be required due to the large difference (~200 K) in condensation temperatures between
633 Ca and Ti on one hand, and Mg and Si on the other hand. Examination of UR-CAIs for which
634 both REE patterns and Mg isotopes are available indeed shows that CAIs with UR REE
635 patterns often have negative δ^{25}Mg values between 0 and -10‰, albeit with relatively large
636 uncertainties (Hinton et al., 1988; Fahey et al., 1994; Simon et al., 1996, 2002; Liu et al.
637 2009). The only known UR CAI with δ^{25}Mg > 0 ‰ (CAI 3483-3-10 in Mighei, MacPherson
638 and Davis, 1994) is an altered fragment with a WLR. The combination of heavy Mg isotopic
639 composition and presence of a WLR suggests that it once was an igneous CAI having
640 undergone evaporation.

641 One possible scenario to explain the REE and isotopic data is that the sinuous
642 pyroxene formed from hibonite-rich precursors that were rapidly removed from the high

643 temperature regions where the UR REE pattern was established and then transported to a
644 region where the temperature, about 200 K lower, was favorable for diopside condensation.
645 The rapid transport would have resulted in preservation of the UR REE pattern at the onset of
646 removal and in subsequent kinetic isotopic fractionation during Si and Mg condensation.
647
648 *4.1.2. Partial assimilation of the sinuous pyroxene.*
649
650 The systematic comparison of the O, Si and Mg isotopic compositions of melilite
651 throughout the inclusion shows that the melilites from areas 3 and 4 and from the
652 subinclusion 1 have isotopic compositions intermediate between those of the Al-diopside
653 sinuous pyroxene fragments ($\Delta^{17}O \sim -20‰$, $\delta^{25}Mg$ and FSi $\sim -3.5‰$) and the remaining
654 melilite of the host inclusion, which cluster around $\Delta^{17}O \sim -6‰$, $\delta^{25}Mg \sim +5.5‰$ FSi$\sim$
655 +6.5‰. These intermediate isotopic compositions can be reproduced by a single mixture
656 between the Al-diopside sinuous pyroxene and the E101.1 main host (Fig. 15) with the
657 exception of two spots in subinclusion 1 (Fig. 15c). The shape of the mixing hyperbolae
658 depends on the relative concentrations of the elements, but by considering the O, Mg and Si
659 isotope compositions we can calculate the mixing proportions in the main E101.1 host by
660 assuming a composition for the second end-member (Fig. 14). The sinuous fragments are
661 dominated by Al-diopside with Al_2O_3 typically in the 2-5 wt% range. For the calculation, we
662 thus assumed that this endmember is pure diopside ($CaMgSi_2O_6$) having the isotopic
663 composition of the sinuous pyroxene. If we further assume that the second end-member
664 consists only of the five elements Ca, Al, Mg, Si and O, we find that the three mixing
665 hyperbolae cannot be reproduced simultaneously by any known mineral having the isotopic
666 composition of melilite. For example, the $\Delta^{17}O$-$\delta^{25}Mg$ mixing line could be matched by
667 mixing diopside with melilite in the $Åk_{10}$-$Åk_{30}$ range with a best match for $\sim Åk_{20}$, but even

668 Åk$_{10}$ would still be too Si-rich to provide a match for the Δ^{17}O-*F*Si mixing line. Rather, this
669 suggests that the mixing occurred between Al-diopside and a CMAS melt having isotopic
670 compositions equal to those observed in melilite. With the final assumption that such a melt
671 had a solar Ca/Al ratio, as expected for most CAIs (e.g., Simon and Grossman, 2004;
672 Grossman et al., 2008b), the data can be fit by mixing hyperbolae corresponding to an
673 extremely refractory CMAS melt having approximately 49 wt% Al_2O_3, 39 wt% CaO, 10 wt%
674 SiO_2 and 2 wt% MgO. This implies that the sinuous Al-diopside fragments are relicts from a
675 xenolith mostly made of ^{16}O-rich diopside with light Mg and Si isotopic compositions that
676 was captured by an extensively molten, highly refractory, ^{16}O-poor melt. They were partially
677 assimilated in this melt, which subsequently crystallized as melilite with intermediate isotopic
678 compositions in area 3 and 4 and in subinclusion 1, while the remaining melilite preserved the
679 initial melt composition upon crystallization. This melt is hereafter referred to as the step 1
680 parental melt (Table 1). The two points in subinclusion 1 not matched by this mixing are
681 instead well reproduced by using an endmember of almost pure gehlenitic composition. This
682 suggests that the CMAS melt was partly crystallized as gehlenite within subinclusion 1, when
683 the sinuous pyroxene was captured. The existence of such a partially crystallized region may
684 explain why some sinuous pyroxene fragments distribute around subinclusion 1. The
685 observed compositions are reproduced if 2 to 5 mol% of sinuous pyroxene was assimilated in
686 areas 3 and 4, while this proportion reach 10 mol% in subinclusion 1.

687 Most likely all the sinuous pyroxene fragments derived from a single proto-CAI as
688 indicated by (1) similar, unusual mineralogy and isotopic compositions and (2) the mixing
689 lines between the sinuous fragments, areas 3 and 4, subinclusion 1 and the main host, which
690 do not require more than one trapped xenolith. Detailed examination of the REE patterns (El
691 Goresy et al., 2002) suggests that the sinuous pyroxene fragments are genetically related to
692 the rest of the E101.1 CAI. Indeed, all UR CAIs have distinct REE patterns that record

complexities in condensation events. These differences are seen most clearly in the abundances of light REE (LREE) relative to those of the heavy REE (HREE) and in the relative proportions of Lu, Er and Ho, the most refractory REEs. In E101.1, all units except a few Sc-Zr-rich pyroxene spots have abundant LREE relative to the HREE. In addition, Lu, Er and Ho are present in comparable abundances in E101.1. Given that these elements have different volatilities, direct condensation should result in Lu > Er > Ho (Davis and Grossman, 1979; Simon et al., 1996; Davis and Richter, 2014). Their comparable or reversed abundances are usually attributed to fractional condensation and removal of an UR mineral with uniform REE activity coefficients, such as ZrO_2, that would preferentially remove Lu and then Er from the gas before establishment of the UR pattern in the main hibonite or perovskite condensate (Simon et al., 1996). The sinuous pyroxene fragments share both the LREE and Lu/Er/Ho features with the rest of E101.1 indicating that they may have been initially related with the host inclusion, perhaps by common UR precursors in spite of a totally different thermal history.

It has been suggested that these diopside-rich xenoliths could represent a former generation of WLR (El Goresy et al., 2002). However, our data do not allow a firm identification of the sinuous pyroxene precursor. Several features indeed compare well with WLRs such as its layered structure, the Al-diopside chemistry of pyroxene commonly found as the outer layer of WLRs and the common association of diopside with anorthite. It is not clear if the sinuous pyroxene is a former WLR fragment but several hypotheses can probably be discarded. The sinuous pyroxene is unlikely to be a fragment from the E101.1 WLR pushed inside because its Mg and especially Si isotopic composition are more negative than those found in the WLR of E101.1 and because the latter contains a Ti-rich fassaitic pyroxene layer inside diopside instead of anorthite (El Goresy et al., 2002). The sinuous pyroxene is also unlikely to be a remant of WLR associated with subinclusion 1. If our analysis is correct,

718 subinclusion 1 is just a region of the host resulting from assimilation of a large fraction of
719 sinuous pyroxene. Its rounded shape is probably fortuitous. Furthermore, in several places the
720 sinuous pyroxene fragments around subinclusion 1 contain diopside in contact with
721 subinclusion 1 and anorthite outside, which is the reverse of the commonly observed WLR
722 sequence. It further lacks the spinel layer ubiquitous in WLR.

723 A similar approach can be used to investigate if the quenched glass areas with relict
724 pyroxene and skeletal gehlenite (Fig. S1) derive from a secondary impact melting event, as
725 initially proposed (El Goresy et al., 2002), or represent a residual melt from the trapping and
726 partial assimilation of the sinuous fragments. Here caution must be taken as (1) only one Mg
727 isotope analysis (Mg36) and no Si isotope analysis has been performed because numerous
728 fine-grained mineral inclusions in the glass prevented more analyses, and (2) matrix effects
729 in Mg isotopic analyses in glass relative to stoichiometric pyroxene or melilite may result in
730 incorrect Mg isotopic ratios. If the analysis is treated as a pyroxene glass, the mixing
731 calculation shows that the O and Mg isotopic compositions of the quench melt regions are
732 matched by the mixing hyperbola calculated for the refractory CMAS parental-melt described
733 above (Fig. S6), in which case the quench glass may be a residual melt. In contrast, if a matrix
734 effect intermediate between that of pyroxene and melilite is applied to account for the glass
735 composition intermediate between diopside and melilite, then the mixing is more consistent
736 with mixing the sinuous pyroxene with a melilite component ~ $Åk_{30}$ in composition (Fig. S6).
737 In this case an impact origin is possible. Dendrites in this melt require rapid cooling, which
738 may imply a two stage history. Note that the presence of Fe in the quenched glass (FeO up to
739 0.9 wt%) indicates a contribution of the FeO-rich regions associated with the sinuous
740 pyroxene, which may have locally changed the composition of the mixture toward a less
741 refractory and more ^{16}O-poor composition. The presence of FeO in the glass indicates the
742 FeO-rich regions must have predated formation of the quenched glass (see section 4.6).

743

744

745 *4.2. Thermal history of the main host*

746

747 The main host precursor as inferred from the mixing calculation between Al-diopside
748 and present-day host melilite is a highly refractory CMAS melt enriched in the heavy Si and
749 Mg isotopes. The Si and Mg isotopic fractionations imply a significant amount of
750 evaporation, but it is not clear whether this evaporation was sufficient to explain the
751 ultrarefractory composition of the CMAS parental melt that was highly depleted in Si and
752 Mg. The Si isotopic composition (FSi ~+ 6.5 ‰) is comparable with that of several F- and
753 FUN inclusions (e.g., TE, CG-14, EK-1-4-1, Clayton et al., 1988; Mendybaev et al., 2013) as
754 well as that of evaporation residues produced in the conditions expected for the formation of
755 FUN CAIs (Mendybaev et al., 2013, 2017). However, the Mg isotopic composition (δ^{25}Mg
756 ~ +5‰) is closer to that of regular CAIs, whereas Mendybaev et al. (2013, 2017) show that
757 δ^{25}Mg values between + 10 and + 15 ‰ are expected from evaporation experiments and up to
758 +20‰ are found in natural FUN CAIs (e.g., CG-14, EK-1-4-1) with FSi comparable to that of
759 E101.1, the lowest δ^{25}Mg values being from evaporation of a forsterite-rich precursor
760 (Mendybaev et al., 2017). The larger degree of mass fractionation in Mg than in Si in these
761 experiments is due to the evaporation of Mg as Mg and Si as SiO, which fractionates less due
762 to its higher mass. Either the E101.1 compositions are indicative of unusual evaporation
763 conditions or the Si and Mg isotopic fractionations were decoupled to some extent. In light of
764 the capture and partial assimilation of the sinuous pyroxene, another capture event can
765 possibly explain the low Mg isotopic composition if the captured material is Mg-rich and Si-
766 poor, such as spinel, and has the usual δ^{25}Mg value expected from equilibrium condensation
767 near 0 ‰ if formed from a reservoir with normal planetary Mg isotopic composition. The

768 CMAS composition of the parent melt predating this second capture event is hereafter
769 referred to as the step 2 precapture melt.
770 To understand the origin of the parent material of the E101.1 main host, we calculated
771 what would be its pre-evaporation chemical composition and the extent of Si and Mg loss,
772 based on the measured Si and Mg isotopic compositions and the CMAS composition of the
773 step 1 parental melt calculated above. To account for possible spinel capture, we considered
774 several cases: (1) no additional material, (2) assimilation of condensate spinel with $\delta^{25}Mg = 0$
775 ‰ so that the initial melt composition had a $\delta^{25}Mg$ of +10 ‰ and (3) assimilation of
776 condensate spinel so that the initial melt composition had a $\delta^{25}Mg = +15$ ‰. In cases of
777 assimilating spinel mass balance considerations indicate that the +5‰ $\delta^{25}Mg$ value is
778 achieved if half of the Mg comes from spinel (case 2) or two-thirds of Mg comes from spinel
779 (case 3). These contributions correspond to a mass fraction of spinel vs CMAS melt of 3.6
780 wt% and 4.8 wt%, respectively, which is not unreasonably large. The step 2 precapture
781 composition of the parental melt is thus calculated by removing the Al and Mg contribution of
782 these amounts of spinel from the step 1 parental composition. Pre-evaporation calculations
783 were subsequently done in the three cases, (1) assuming that Si and Mg evaporate as $SiO_{(g)}$
784 and $Mg_{(g)}$, (2) using the Rayleigh equation for kinetic evaporation and (3) using either the
785 fractionation factors determined in Knight et al. (2009) for a sub-liquidus temperature of Type
786 B inclusions of 1400°C, or the fractionation factors determined by Mendybaev et al. (2013)
787 for the production of FUN inclusions at 1900°C, thus yielding six possible pre-evaporation
788 compositions referred to as step 3 compositions.
789 The results presented in Fig. 16, show first that the contribution of captured spinel
790 does not change significantly the composition of the parental melt (step 2) relative to the
791 products of equilibrium condensation as calculated in Grossman et al. (2008b). In each of the
792 three cases, it is close to the first condensate expected at high temperature, near the field of

melilite + krotite ($CaAl_2O_4$) condensation. However, the heavy Si and Mg isotopes indicate that this cannot be the initial composition of the parental E101.1 host melt. Second, using any set of kinetic fractionation factors yields comparable results. All six step 3 pre-evaporative compositions calculated with any amount of spinel removed at step 2 are found to match nicely with the theoretical composition of a condensate (Fig. 16) in the hibonite + perovskite + melilite field at 10^{-3} to 10^{-4} bar (Mendybaev et al., 2017).

The precursor material of the E101.1 parental melt is thus consistent with an extremely refractory condensate, much more refractory than typical Type A CAIs, that subsequently underwent evaporation. In the model without spinel assimilation, the fractions of Si and Mg lost are 47% and 42%, respectively, using the fractionation factors of Knight et al. (2009) and 47% and 29%, respectively using those of Mendybaev et al. (2013). Assuming that the Mg-Si isotopic decoupling is due to condensate spinel assimilation, the fraction of Mg lost reaches 66% / 50% (depending on the fractionation factor) for an initial δ^{25}Mg value of +10‰ and 80% / 64% for an initial δ^{25}Mg value of +15‰.

The highly refractory composition of the precursor condensate, in the stability field of hibonite, perovskite and melilite, is well in line with the presence of large perovskite grains. It also agrees with the UR REE pattern, which points to a condensation temperature range corresponding to that of hibonite and perovskite, the highest temperature major condensates that carry REE (e.g., Lodders, 2003). The excesses and depletions in ^{48}Ca (-7.5‰ $\leq \delta^{48}$Ca $\leq$ +9.8‰) in three perovskite grains analyzed previously (El Goresy et al., 2002) suggests a possible connection with FUN inclusions, agreeing with the strong mass fractionation by evaporation indicated by the *F*Si values. Although unusual, such ^{48}Ca anomalies without associated ^{50}Ti anomalies have also been found in hibonite-rich FUN inclusions from Murchison (Kööp et al., 2018). Together with the calculated hibonite-rich precursor composition and the UR pattern, often attributed to hibonite condensation (e.g. Davis et al.,

818 2018), this suggests a link between the precursor of E101.1 and hibonite-rich FUN inclusions.
819 Whether the fractionated component (F) is initially the same as the carrier of the nuclear
820 anomalies in ^{48}Ca in E101.1 is unclear because the subsequent capture of xenolithic material
821 renders the characterization of the initial material subject to uncertainties. The precursor
822 material of E101.1 can be viewed as an ultrarefractory FUN inclusion resulting from
823 extensive melting and evaporation of an UR condensate precursor with isotopic anomalies of
824 nucleosynthetic origin. Alternatively, the UR component with nuclear anomalies (the UN
825 component) recorded in the pristine condensate perovskite may have been aggregated to a
826 highly mass fractionated component (the F component) before they were partially melted
827 together. In this case the F and UN components could have been initially decoupled as
828 suggested by the existence of F CAIs without nuclear isotopic anomalies (Clayton et al.,
829 1984; Caillet Komorowski et al., 2007; Krot et al., 2014). The lack of large mass fractionation
830 in O isotopes in perovskite may support this conclusion. However, many FUN inclusions
831 contain unfractionated components issued from the first crystallization stages before the melt
832 was completely evaporated (Thrane et al., 2008; Krot et al., 2014), which may well be the
833 case for perovskite.

834 Recent studies indicate that FUN CAIs are related to normal CAIs (Park et al., 2014;
835 Krot et al., 2014). On the one hand, Ca, Ti and ^{26}Al isotopic anomalies define a continuum
836 between FUN inclusions and normal CAIs (Park et al., 2014, 2017). On the other hand, the
837 coupled petrographic and O isotope study of twelve FUN inclusions shows that they are
838 petrographically similar to normal CAIs and exhibit O isotope mass fractionation effects of
839 variable amplitude not correlated with the isotopic anomalies (Krot et al., 2014). This was
840 attributed to variable conditions of partial melting and evaporation and variable sampling of
841 reservoirs with diverse presolar components (Krot et al., 2014; Park et al., 2017). If this is
842 correct, and in light of the multiple aggregation history of E101.1 revealed by the present

study, which probably includes assimilation of a FUN component, it is reasonable to consider that most igneous CAIs may have been formed by the aggregation and partial melting of various precursors, among which were a proportion of FUN material with inherited presolar isotopic anomalies.

4.3. Insights on the nature of the UR precursor of E101.1 from perovskite

Differences in the chemistries of perovskite grains in E101.1, notably in their ZrO_2/Y_2O_3 ratios, have been interpreted as indicating the presence of four distinct populations of perovskite (El Goresy et al., 2002). These populations include perovskite grains with (1) chondritic ZrO_2/Y_2O_3 ratios ~2.7, suggesting an origin by condensation and (2) grains with ZrO_2/Y_2O_3 ratios ~ 0.4, typical of crystal-liquid fractionation indicative of crystallization from a melt. The two other perovskite grains are either (3) devoid of ZrO_2 or (4) have intermediate ZrO_2/Y_2O_3 ratios between 0 and ~2.7. Different perovskite populations can also be recognized based on their textural context, although it is not clear if chemical and textural populations can be linked: large anhedral perovksite grains are commonly associated with metal and/or V-Fe-oxide indicative of interactions with metal, and are rimmed by the Sc-Zr-rich pyroxene (Fig. 4). Such textures are suggestive of partial melting and reaction of pre-existing perovskite with a silicate melt and agree with considerations from minor and trace elements (El Goresy et al., 2002). Other grains, usually much smaller, are euhedral and enclosed within pyroxene, sometimes within pyroxene ± spinel rims around spinel (e.g., in cluster 5, Fig. 3d), suggesting late crystallization either from a Ti-rich partial melt or at the solid state. The abundance of perovskite in E101.1 suggests a perovskite-rich UR precursor of bulk chemistry in the hibonite + perovskite + melilite condensation field The chemical and textural diversity of perovskite further indicates contribution of perovskite with (1) diverse

868 condensation histories and (2) variable post-aggregation histories including reaction with a
869 partial melt, new crystallization from a partial melt and solid state equilibration with the
870 surrounding phases.

871 Perovskite grains analyzed for O isotopes are large anhedral grains and have a range
872 of ZrO_2/Y_2O_3 ratios. This includes (i) chondritic perovskite (per B), (ii) Zr-free perovskite (4
873 grains) and (iii) perovskite with intermediate ratios (2 grains). Large variations in $\Delta^{17}O$ are
874 observed. On one hand, some grains enriched in ^{16}O to a level approaching that of spinel
875 ($\Delta^{17}O$ = -19.2 ‰) are found in different populations (Fig. 9). On the other hand, both ^{16}O-rich
876 grains and ^{16}O-depleted grains with $\Delta^{17}O$ up to -8.9 ‰ are found in a single population (Zr-
877 free perovskite). Because (i) the Sc-Zr-rich pyroxene that rims perovskite is among the most
878 ^{16}O-poor mineral in E101.1 and most likely records the composition of the melt, and because
879 (ii) the diffusivity of O in solid perovskite is rapid (Gautason and Muehlenbachs, 1993;
880 Sakaguchi and Haneda, 1996), a plausible interpretation is that all perovskite grains were
881 initially ^{16}O-rich and experienced partial re-equilibration with the enclosing Sc-Zr-pyroxene,
882 either sub-solidus or between solid perovskite and melt. All grains analyzed here have
883 comparable sizes in the 20-30 μm size range and all analyses include most of the grains, so
884 that it has not been possible to evaluate the extent of O isotopic zoning in perovskite, thus
885 rendering the latter hypothesis impossible to confirm or negate.

886 The anhedral shapes of the ^{16}O-rich perovskite grains are consistent with the idea that
887 they represent partially melted relict grains. These grains belong to the population with close-
888 to-chondritic ZrO_2/Y_2O_3 ratios (Per B) and to the population with ZrO_2 content near or below
889 the detection limit of the electron probe (Fig. 9). Whereas the chondritic population can be
890 understood as resulting from direct condensation from a solar gas, the origin of the Zr-free
891 grains remains unclear. Because Zr-oxides have already been observed in UR CAIs (Ivanova
892 et al., 2012) and because Zr is an ultrarefractory element that condenses at equilibrium as

ZrO_2 before corundum and hibonite condense (i.e., at higher temperature, Lodders, 2003), a possibility is that the Zr-free perovskite is an UR condensate that formed after a fractionation due to previous condensation of ZrO_2. As mentioned above such a fractional condensation is in line with the comparable abundances of Lu, Er and Ho in E101.1 instead of Lu > Er > Ho as expected from relative volatilities (Simon et al., 1996). Both the chondritic and the Zr-free perovskite probably represent end-member products of the condensation of UR minerals due to slight variations of the condensation conditions (temperature or pressure). We also note that some of the Zr depletion in perovskite probably arose from the late solid-state diffusion into the Sc-Zr-rich pyroxene (El Goresy et al., 2002). A reasonable interpretation is thus that the large perovskite grains were initially part of a ^{16}O-rich UR inclusion (or several) condensing in the hibonite + perovskite + melilite field and containing precursor UR oxides inherited from condensation steps above 1700 K (e.g., Simon et al., 1996), such as those described in other compound CAIs (e.g., Ivanova et al., 2012). Such an UR inclusion could be the carrier of the UN isotopic anomalies suggested by ^{48}Ca excesses and deficits in perovskite. It may have experienced a ^{16}O-depletion during the melting event associated with extensive Mg, Si evaporation and isotopic fractionation that transformed the E101.1 precursor into a FUN inclusion. In this case, the ^{16}O-rich perovskite would represent the starting material of the FUN inclusion and melilite ± Sc-Zr-rich pyroxene would represent the final crystallization product after equilibration with the ^{16}O-poor gas (Krot et al., 2014). The lack of strongly mass fractionated O isotope component corresponding to the heavy Si component would then be explained by the peculiar chemistry of E101.1, which lacks intermediate minerals with slow oxygen diffusivities recording the composition of the evaporating melt, such as spinel, forsterite or pyroxene. The O isotopic compositions of initial perovskite and final melilite + Sc-Zr-rich pyroxene compare well with those of initial spinel and final melilite, respectively, in some FUN inclusions having Si isotopic compositions similar to that

of the E101.1 parental melt (e.g., CG14, EK1-4-1, Krot et al., 2014). This scenario would also agree with the residual O isotope mass fractionation observed in Sc-Zr-rich pyroxene and some of the ^{16}O-poor melilite (Fig. 7). Alternatively, the ^{16}O-rich UR perovskite-rich precursor could have coagulated with a F(UN)-like proto-CAI previously mass fractionated and both were partially melted together.

4.4. Extraneous origin of the spinel clusters

Beside evidence of perovskite partial melting, there are numerous examples of spinel resorption (e.g., rounded shapes, embayments) in E101.1. These features, as well as the presence of the pyroxene-rich symplectite around spinels, and the chemical and isotopic zonation of melilite (enriched in gehlenite and often in ^{16}O at the contact with spinel; Fig. 6) are indicative of a coronitic reaction resulting in spinel dissolution. Interestingly, a spinel + liquid = anorthite + melilite + clinopyroxene reaction has been observed in the CMAS system (O'Hara and Biggar, 1969; Schairer and Yoder, 1969; Yang et al., 1972; Onuma and Kimura, 1978). Although it has not been observed directly, such a reaction has been inferred during closed-system crystallization of Type B CAI liquids, based on the proportions of spinel as a function of temperature (Stolper, 1982). A similar reaction in the highly silica-poor system of Type A CAIs may therefore result in a comparable reaction where anorthite is absent in favor of highly gehlenitic melilite and highly aluminous pyroxene (reaction 1).

(1) spinel + liquid = gehlenite + clinopyroxene

We suggest that the coronitic textures observed around spinel are the signature of this reaction. It would explain all resorption features in spinel, the presence of the pyroxene ±

spinel symplectite and the coupled enrichment in ^{16}O and Al_2O_3 in melilite at the contact with spinel (Fig. 6).

Whether reaction (1) occurred in closed or open-systems cannot be deduced from the coronitic textures alone. Additional insights come from Mg isotopes (Fig. 11,12). Most spinel clusters have $\delta^{25}Mg$ values near 5-6‰, close to each other and within error of the associated melilite (Fig. 12). However some heterogeneities point to incomplete homogenization. Although the exact spinel-melilite difference can possibly be subject to small uncorrected matrix effects, the range of $\delta^{25}Mg$ values in spinel from 2.6‰ (cluster 5) to 6.6‰ (cluster 4) with an intermediate 4.3‰ (cluster 3) is beyond 2σ analytical uncertainties (< 1‰). The Al/Mg systematics of spinel clusters and associated melilite are mostly comparable from cluster to cluster (Table 2, Fig. 11) but heterogeneities exist as well. Intercepts in the Al/Mg regressions from the various clusters (Fig. 11) yield a range from 0.11 ± 0.28 ‰ to 0.87 ± 0.22 ‰, again beyond 2σ errors. Finally, spinel clusters from subinclusion 1 have Mg isotope systematics similar to the others in terms of radiogenic Mg and spinel-melilite stable isotope equilibration, albeit for a much different $\delta^{25}Mg$ value near 0‰ (Fig. 12), which has been shown to result from mixing between the host inclusion and the sinuous pyroxene fragments (Fig. 15).

In a first interpretation, most melilite and spinel have identical Mg isotopic composition and Al/Mg systematics. In this hypothesis, supracanonical spinel in cluster 2 (Table 2, Fig. 11) and light melilite near cluster 5 (analysis Mg58) must be considered special as well as subinclusion 1, possibly another xenolith of its own in this case. Our favorite interpretation is however that these heterogeneities result from incomplete homogenization between spinel clusters and the host melilite/melt, including in subinclusion 1, where the analyzed spinel seem to belong both to the spinel swarms and to subinclusion 1 (Fig. 1,2). In this hypothesis, the supracanonical spinel in cluster 2 results from diffusive exchange with

surrounding melilite (see section 4.6) and the light δ^{25}Mg value at 3.7‰ near cluster 5 (Mg58) may indicate a contribution of light Mg from spinel, in agreement with O isotopes indicating a contribution of spinel-derived ^{16}O-rich oxygen (Fig. 6).

We therefore suggest that all spinel clusters initially had a stable Mg isotopic composition different from that of the host E101.1 CAI, and thus a different origin. They subsequently underwent Mg isotope exchange with the surrounding melilite or parental melt owing to rapid Mg self-diffusion in spinel (Sheng et al., 1992) up to the point of complete or near-complete equilibration (clusters 1, 2 and 4). At 1300 to 1400°C, typical of melilite crystallization, Mg isotope exchange in a 10 μm spinel is complete in 2 to 10 hours. This isotopic disequilibrium is in line with chemical evidence for several spinel populations with varying V, Ti and Cr content (El Goresy et al., 2002). For comparable Cr content, host spinels (i.e., spinel clusters) and some spinels in subinclusion 1 have the highest V content. Because the diffusion of V in spinel is rapid compared to that of Cr (Connolly and Burnett, 2003), this indicates a significant degree of equilibration with the host melt or melilite for these spinels.

Taken together, the coronitic textures, the distribution of gehlenitic melilite and the O and Mg isotope systematics suggest introduction of the parental material of the spinel clusters by capture of solid material into a partially molten CAI host droplet, confirming the suggestion of El Goresy et al. (2002) based on the minor element chemistry of spinel. Spinel clusters can thus be considered to represent ^{16}O-rich, spinel-rich proto-CAIs captured by the host inclusion and partially dissolved into the host melt. It is interesting to note that cluster 3, the least equilibrated of the upper 4 clusters (Fig. 1) is also the outermost. Clusters 1 to 4 may have been fragments of the same initial proto-CAI captured in a single event and increasingly equilibrated with melilite as they are deep within the channel.

Such a ^{16}O-rich spinel-rich proto-CAI may have been a fine-grained-spinel-rich CAI (FG-sp-rich CAI, e.g., Krot et al., 2004a) in which minerals other than spinel, i.e., having

992 lower melting temperature (e.g., pyroxene ± melilite ± anorthite), would have been entirely
993 dissolved in the host melt, possibly contributing to an additional local enrichment in Al and
994 ^{16}O. In this case, the subhedral crystal shapes observed in many grains of the spinel clusters
995 would have to result from recrystallization or annealing of fine-grained aggregates of spinel.
996 Unaltered FG-sp-rich CAIs are homogeneously rich in ^{16}O (e.g., Aléon et al., 2002, 2005;
997 Fagan et al., 2004; Bodénan et al., 2014; Ushikubo et al., 2017) and are commonly devoid of
998 heavy Mg because they escaped extensive melting and evaporation. Their δ^{25}Mg values are
999 usually near 0‰ or slightly negative (e.g., Clayton et al., 1988; MacPherson et al., 2010;
1000 Ushikubo et al., 2017). As a result, capture of such spinel-rich material is consistent with the
1001 Mg-Si isotopic decoupling inferred in the parental CMAS melt of the host inclusion (section
1002 4.2), as well as the lower δ^{25}Mg value of cluster 5. We calculated that the contribution of the
1003 spinel-rich material should be of a few wt% to account for the Mg-Si isotopic decoupling,
1004 which agrees with the abundance of spinel as visible on the E101.1 polished section.
1005 Removing the spinel clusters from the host CAI mineralogy leaves an initial precursor with
1006 melilite + perovskite mineralogy, essentially devoid of spinel, which agrees with the
1007 calculated precursor chemistry falling in the hibonite + perovskite + melilite domain if
1008 hibonite has been completely resorbed in favor of a more gehlenitic melilite. We conclude
1009 that the capture of extraneous fine-grained spinel-rich proto-CAIs well accounts for the
1010 properties of the spinel clusters as well as the isotopic systematics of the host parental melt.
1011 The capture of ^{16}O-rich spinel-rich CAIs by a ^{16}O-poor melilite dominated host
1012 inclusion is analogous to the situation in E49, another CTA compound inclusion from
1013 Efremovka (Aléon et al., 2007). In other CAIs, spinel and melilite have been shown to
1014 occasionally be in Mg isotopic equilibrium (e.g., Fahey et al., 1987; Kita et al., 2012) and in
1015 some cases show evidence of Mg isotope disequilibrium (e.g., Paque et al., 2013; Goswami et
1016 al., 1994), with spinel being either heavier or lighter than coexisting melilite by at most 1 or 2

1017 ‰. With the caveat that matrix effects are important in Mg isotopic analysis by SIMS and
1018 need to be carefully taken into account to investigate the spinel-melilite isotopic difference at
1019 the sub-permil level (e.g., Kita et al., 2012; Paque et al., 2013), this suggests that spinel of
1020 extraneous origin that underwent subsequent partial to complete isotopic re-equilibration may
1021 be common in CAIs.
1022
1023
1024 *4.5. Formation of the margins and rims of the host CAI*
1025
1026 *4.5.1. Forsterite-rich accretionary rim*
1027
1028 The multi-isotope study of E101.1 can also be used to shed light on the origin of the
1029 outermost envelopes of igneous CAIs, the WLR and the forsterite-rich accretionary rims (AR,
1030 e.g., Krot et al., 2001). ARs are thought to be somewhat analogous to AOAs. They are
1031 composed primarily of highly magnesian olivine aggregates, commonly anhedral and porous.
1032 Some are more compact with triple junctions suggesting secondary annealing (Krot et al.,
1033 2001, 2004b). Numerous CAI-like nodules mostly composed of Ca-clinopyroxene ± anorthite
1034 ± spinel are often interspersed with forsterite (Krot et al., 2004b). The commonly held view is
1035 that AR are aggregates of fine-grained nebular condensates of relatively low temperature, in
1036 the range of forsterite condensation (Krot et al., 2001), subsequently aggregated onto larger
1037 CAIs and eventually partially reprocessed on the parent-body (Krot et al., 2001). The Mg and
1038 Si isotopic compositions of forsterite from the AR in E101.1 correspond to δ^{25}Mg and *F*Si
1039 close to 0 ‰ or slightly negative, which is in good agreement with the expectation for
1040 equilibrium condensation (Fig. 17) and with previously published Mg isotopic analyses of AR
1041 and AOAs (Larsen et al., 2011; MacPherson et al., 2012; Mishra and Chaussidon, 2014). The

1042 ^{16}O-rich composition of forsterite indicates that the gas from which they condensed was ^{16}O-
1043 rich as inferred from other AR and AOAs (Krot et al., 2002).
1044
1045 *4.5.2. Wark-Lovering rim*
1046
1047 In contrast to the ARs, the origin of WLR is more debated. They typically consist of
1048 close to monomineralic layers mimicking the condensation sequence from spinel ± hibonite ±
1049 perovksite at the contact with the host inclusions to Al-Ti-pyroxene ± melilite ± anorthite, to
1050 Al-diopside (e.g., MacPherson, 2014) toward the edge of the CAI. In some cases, the
1051 outermost layers consist of pure diopside and/or forsterite. Different origins have been
1052 proposed, which can be grouped into two categories: condensation models and flash heating
1053 models. Condensation models include (1) successive deposition onto a CAI of various layers
1054 of condensation (Wark and Lovering, 1977) with decreasing temperature from the innermost
1055 spinel ± hibonite ± perovskite to the outermost forsterite layers, (2) growth of isolated nucleus
1056 islands deposited onto the interior CAI (Bolser et al., 2016) and (3) diffusive equilibration of
1057 the edge of the CAI with the gas (Ruzicka, 1997; Simon et al., 2005; Simon et al., 2016).
1058 Light stable Mg isotopic composition supports these condensation models (Taylor et al.,
1059 2004; Cosarinsky et al. 2005a,b; Simon et al., 2005) but enhanced REE abundances in the
1060 rims and REE patterns identical to the host inclusion favor flash heating hypotheses (e.g.
1061 Wark and Boynton, 2001). These conflicting interpretations could potentially be reconciled if
1062 WLR formed by condensation of nebular gas and a melted outer layer is involved at some
1063 stage (Toppani et al., 2006; Keller et al., 2013; Simon et al., 2016). Mg isotopes and Ti
1064 valence have been used to argue that the WLR formed at a much higher fO_2, closer to that of
1065 chondrites, than the inner host formed at a solar fO_2 (Simon et al., 2005; Dyl et al., 2011)
1066 although this is debated (Simon et al., 2007). Finally, Mg isotopes also suggest that WLR

have crystallization ages commonly younger than their host inclusions by about 200,000 to 300,000 years (Taylor et al., 2004; Cosarinsky et al., 2005a,b; Simon et al., 2005). Even larger time intervals of at least 590,000 and 690,000 years have recently been reported (Mane et al., 2015)

In E101.1, the outermost WLR pyroxenes exhibit the UR-REE pattern typical of the host inclusion (El Goresy et al., 2002), including the specific LREE/HREE and Lu/Er/Ho relative proportions, which suggests a contribution from the interior inclusion. In one case (Mg34) the δ^{25}Mg value of the WLR pyroxene of E101.1 shows an enrichment of +3 ‰, close to that of interior melilite, but in all other cases, both pyroxene and spinel have δ^{25}Mg values near 0 ‰, similar to those of the AR forsterite. By contrast, the *F*Si values span the whole range between the slightly negative values of the AR forsterite and those of the average main host melilite (Fig. 17), possibly up to +10 ‰. The Mg isotopic composition is in agreement with expectations from equilibrium condensation in most cases but in the case of spot Mg34 also shows the contribution from interior Mg. The Si isotopic composition indicates a more balanced mixture between Si of condensation origin, similar to Si in the AR forsterite, and Si from the interior with enrichment in the heavy isotopes due to evaporation. Both the REE patterns and the stable Mg, Si isotopic compositions thus indicate some contribution from the interior CAI. Such an influence strongly hints that the WLR did not form by successive deposition of condensate layers at decreasing temperatures or grew from isolated nucleus islands disconnected from the interior inclusion. Nevertheless, both Mg and Si do indicate a contribution of a condensate component. Although analysis Si15 in the innermost WLR pyroxene must be treated with caution, its *F*Si value of +10‰, heavier than in interior melilite, may be the additional signature of a strong evaporation from a melt. Thus our data support models based on open system behavior in which the WLR formed by a combination of (i) melting of the inner host that preserved the most refractory elements and a

1092 fraction of the less refractory Mg and Si and (ii) condensation into the melt of nebular Mg and
1093 Si. Such a scenario has already been proposed from the TEM study of a WLR from a Type B1
1094 CAI from Vigarano (Toppani et al., 2006). The latter study also documented secondary
1095 alteration phases at the sub-µm scale. Although the NanoSIMS study of WLR from CV
1096 chondrites shows variations of ^{16}O content (Simon et al., 2011, 2016), the study of WLR in
1097 unaltered chondrites favors a parent-body origin for these variations (Bodénan et al., 2014;
1098 Krot et al., 2017), in agreement with the TEM observations. Our data favor a systematic ^{16}O-
1099 rich composition of primordial unaltered WLR (this work, Yoshitake et al., 2005; Aléon et al.,
1100 2007; Bodénan et al., 2014; Kawasaki et al., 2017; Krot et al., 2017). Most likely, the gas with
1101 which the CAI equilibrated during WLR formation was ^{16}O-rich.
1102
1103 *4.5.3. Zoning of the outer portion of the host CAI*
1104
1105 This scenario of WLR formation explains the isotopic composition of the rim, and also
1106 the O, Mg and Si isotopic zoning observed in the outer part of CAIs (e.g., Simon et al. (2016)
1107 for O). In E101.1, chemical and isotopic profiles indicate that the distribution of Mg in the
1108 outer part of the CAI (Fig. 13) was affected by a process resulting in (1) an enrichment in Al
1109 or loss in Mg toward the exterior, (2) an enrichment in unfractionated Mg, (3) an enrichment
1110 in undisturbed near-canonical ^{26}Al. In the framework of the WLR formation by condensation
1111 from nebular gas into a partially melted CAI layer, these profiles are well understood by a
1112 global loss of interior Mg in the periphery together with a progressive enrichment in nebular
1113 Mg. Whether the observed profiles result from solid-state diffusion, partial melting and
1114 recrystallization or a combination of both is unclear. By contrast, the Si and O isotopic
1115 compositions do not show any relationship with proximity to the WLR (Fig. 13d,e). In the
1116 case of Si isotopes, this agrees with the WLR systematics, which shows a much greater

1117 contribution of interior Si than of interior Mg in the rim (Fig. 17). Interestingly, the width of
1118 the zone affected by this interaction varies between profile 1 (30-50 μm) and profile 2 (70-
1119 100 μm) (Fig. 13a-c) suggesting small variations in the thermal regime or in the CAI response
1120 to the WLR-forming event. Parameters such as temperature, chemical gradients due to
1121 differences in total and partial pressures in the gas and to differences in CAI chemistry
1122 probably induce even larger variations of thickness of this zone between different CAIs with
1123 different thermal histories. An extreme case of intra-CAI variations may be bowl-shaped
1124 CAIs with different WLR mineralogy in their concave and convex faces suggesting different
1125 degrees of heating attributed to a lack of spinning in the nebula (Ivanova et al., 2014). Inter-
1126 CAI variations of thermal regime during WLR formation probably also explain why Mg and
1127 O gradients are not always present simultaneously. Many Type A CAIs show for instance an
1128 enrichment in gehlenite toward the exterior, in some cases associated with a Mg isotopic
1129 composition evolving toward lower δ^{25}Mg values (Fahey et al., 1987; Goswami et al., 1994;
1130 Simon et al., 2005; Cosarinsky et al., 2006), in some cases associated with an enrichment in
1131 ^{16}O (Aléon et al., 2007; Katayama et al., 2012; Kawasaki et al., 2012, 2017). Similarly to
1132 E101.1, a decrease in δ^{25}Mg values together with little variation in Si isotopic composition
1133 has been observed in the outer mantles of Type B1 CAIs (Bullock et al., 2013). Bullock et al.
1134 (2013) conclude that these profiles would be best explained by a secondary "ad-hoc" process.
1135 We suggest that this process is in fact WLR formation. In the cases where the interior CAI is
1136 almost unaffected by WLR formation (i.e., where the transition region has a thickness near 0),
1137 the CAIs may have preserved pre-WLR zoning reflecting high temperature interaction of a
1138 solid CAI with nebular gas such as sublimation of Mg and Si from the solid state (e.g., CAI
1139 Leoville 144A, Simon et al., 2005; Shahar and Young 2007) or diffusion of ^{16}O-poor oxygen
1140 from the gas (e.g., CAI Allende A37, Simon et al., 2011, 2016). Given the decoupling
1141 between O and Mg in E101.1, the two outermost ^{16}O-poor analyses in profile 1 may reflect

1142 the preservation of such an initial ^{16}O-poor composition of the melt due to equilibration with
1143 ^{16}O-poor gas before trapping of the xenoliths and WLR formation.
1144
1145
1146 *4.6. Al/Mg chronology and disturbances*
1147
1148 The lack of a well-defined Al/Mg isochron in E101.1 host melilite, the evidence of
1149 isotopic disequilibrium between spinels and host melilite, and the insufficient precision on the
1150 slopes and intercept of isochrons deduced from analyses of pyroxene preclude a simple
1151 chronological analysis of E101.1 crystallization. Still, the distribution of model $(^{26}Al/^{27}Al)_0'$
1152 ratios with location in the CAI or between subcomponents can shed light on the origin of
1153 Al/Mg systematics perturbations and on the putative initial ^{26}Al/^{27}Al ratio prior to these
1154 perturbations (Table 2).
1155 As mentioned in section 4.4, the lack of complete stable Mg isotope equilibrium
1156 between spinel clusters and adjacent melilite is visible to some extent with the radiogenic
1157 isotopes. The Al/Mg systematics in paired spinel and melilite are illustrated in Fig. 11. Three
1158 cases can be distinguished.
1159 In cluster 2 (Fig. 11a), sub-canonical mellite is associated with supercanonical spinel.
1160 All 4 analyses define a single linear relationship, which yields an initial ^{26}Al/^{27}Al slope of
1161 $(2.9\pm0.3) \times 10^{-5}$ and a distinctly positive initial δ^{26}Mg* intercept of 0.87 ± 0.22 ‰ (2σ errors).
1162 This behavior is characteristic of a closed-system redistribution of Mg isotopes between
1163 spinel and associated melilite, pivoting around the bulk composition which would be
1164 coincident with the canonical isochron if the system initially had ^{26}Al/^{27}Al = 5.2×10^{-5}.
1165 In subinclusion 1 (Fig. 11b), spinel has a canonical abundance of ^{26}Mg*, but the two
1166 melilite analyses in the vicinity of spinel define a linear array with the spinel with a

subcanonical slope of (3.5±0.4) × 10^{-5} and a positive intercept of 0.45 ± 0.16 ‰. Such slope and intercepts are also indicative of closed-system exchange in the spinel-melilite system, although spinel seems to have been little affected by this perturbation. One possible explanation is an initially sub-canonical bulk composition. This would indicate a younger crystallization age for subinclusion 1, as young as 400 ± 100 thousand years after canonical. However, when considering all melilite analyses in subinclusion 1, the canonical $(^{26}Al/^{27}Al)_0'$ ratio of analysis Mg50 is not in a favor of such a chronological interpretation (Fig. 10). Rather it may indicate the variable contribution of a ^{26}Al-poor component (see below).

In contrast, spinel and the associated melilite of cluster 3 (Fig. 11c) define a linear array with a slope of (3.3±0.4) × 10^{-5} that passes through the origin (intercept = 0.11 ± 0.28 ‰). If this 2-point line is considered to be an isochron, it would yield a crystallization age of 480 ± 120 thousand years after canonical. Such an age may represent the age of cluster 3 trapping in the host CAI, however it would not be consistent with the closed-system interactions in other spinel clusters - melilite pairs implying that either the trapping of cluster 3 is a late isolated event or that the linear correlation does not correspond to the crystallization age. Another possible interpretation for this cluster closest to the edge of the CAI is an open-system re-equilibration of both spinel and associated melilite with a reservoir of lower ^{26}Al content (e.g., Simon and Young, 2011). This reservoir is unlikely to be the meteorite matrix as near canonical $(^{26}Al/^{27}Al)_0'$ ratios are observed in melilite in close contact with the WLR in profile 1 and in areas 3 and 4 (Fig. 13c). Thus, it has to be exchange with a nebular reservoir of low ^{26}Al content.

The distribution of model $(^{26}Al/^{27}Al)_0'$ ratios in melilite as function of distance from the rim (Fig. 13c) is helpful in interpreting the overall Al/Mg isotope systematics of E101.1. As mentioned above, profile 2 and areas 3 and 4 display near canonical $(^{26}Al/^{27}Al)_0'$ ratios in the vicinity of the rim. Apart from one analysis with a low $(^{26}Al/^{27}Al)_0'$ ratio in profile 1, a

1192 progressive decrease in $(^{26}Al/^{27}Al)_0'$ ratios toward the interior is visible everywhere in the
1193 outermost 80 μm of the CAI, down to about 3×10^{-5}, inward of which scattered ratios are
1194 found. Interestingly, the isotopic composition of cluster 3 is consistent with this lower limit,
1195 cluster 3 being located ~ 100 μm inside the CAI. As the outer part of the CAI and the WLR
1196 cannot be older than the interior CAI, this suggests a secondary perturbation with the WLR
1197 and the outermost melilite having best preserved the initial near-canonical composition.
1198 A possible interpretation based on the relationship between the parental E101.1 melt
1199 and FUN inclusions discussed above is that E101.1 crystallized from different proto-CAIs
1200 with different initial ^{26}Al contents. Indeed, many FUN inclusions are known to be devoid of
1201 or depleted in ^{26}Al (e.g., Esat et al., 1978; Clayton et al., 1984; Davis et al., 1991; Holst et al.,
1202 2013; Park et al., 2017) and mixing of a FUN precursor of low ^{26}Al content with xenoliths
1203 having canonical or near canonical ^{26}Al content will induce strong confusion of the Al/Mg
1204 isotope systematics in the final E101.1 CAI. These perturbations are likely to be more
1205 significant in the interior of the CAI than on the exterior, where re-equilibration with the
1206 regular canonical CAI reservoir, from which xenoliths are issued, will be favored. Such a
1207 ^{26}Al-poor FUN component may be the nebular reservoir required to explain the isotopic
1208 composition of cluster 3.
1209 To summarize, the Al/Mg isotope systematics of E101.1 can be understood as
1210 resulting from the mixing of parental FUN material depleted in ^{26}Al with xenoliths having
1211 abundant (the sinuous pyroxene) up to canonical (the spinel clusters) ^{26}Al content. In the hot
1212 CAI interior, local closed-system interactions between spinel/pyroxene and melilite resulted
1213 in scattered $(^{26}Al/^{27}Al)_0'$ ratios. Closer to the outside of the CAI, open-system resetting of Mg
1214 (e.g. Simon and Young, 2011) due to mixing of canonical and ^{26}Al-poor material led to
1215 intermediate Al/Mg apparent isochrons resulting from the subsequent decay of ^{26}Al (cluster
1216 3). Finally, the outermost portion of the CAI equilibrated with the ambient gas having

canonical or near-canonical ^{26}Al content. This is consistent with the initial $\delta^{26}Mg^*$ of forsterite in the AR being comparable to that determined from AOAs and AR of igneous CAIs with canonical $^{26}Al/^{27}Al$ ratios (Larsen et al., 2011; MacPherson et al., 2012; Mishra and Chaussidon, 2014).

A chronological constraint on the formation of E101.1 could in principle be obtained from its WLR formation, the last melting event suffered by the CAI. However, time intervals as small as 2-3 × 10^5 years between the formation of the interior CAI and that of the WLR (Simon et al., 2005; Taylor et al., 2005a,b; Cosarinsky et al., 2006) must be treated with caution. A problem is that the required high precision Al/Mg dating of individual minerals in WLR is extremely difficult to achieve due to the small size of the crystals. Large errors and uncertainties on the Mg isotopic closure for instance due to Mg self-diffusion in spinel make it difficult to obtain good chronological constraints. Here we show that the range of model initial $^{26}Al/^{27}Al$ in WLR spinel from E101.1 varies between (3.7±0.5) × 10^{-5} and (5.7±0.4) × 10^{-5}, i.e., corresponding to an apparent age interval of 460,000 years between the first and last spinel crystallized, although it is within error consistent with a 240,000 years interval between the last and the canonical spinels (Fig. 18). In a first approximation, this estimate is consistent with most previous results (Simon et al., 2005; Taylor et al., 2005a,b; Cosarinsky et al., 2006), except those larger than 590,000 years measured in anorthite (Mane et al., 2015) but anorthite is a mineral highly susceptible to Mg isotope re-equilibration and may not provide an accurate age of WLR formation. However, if the range in E101.1 spinel were to correspond to Mg exchange with a reservoir with different ^{26}Al content, the age conclusion would also be erroneous. For instance, a local and variable contribution of interior FUN material devoid of ^{26}Al to the WLR could potentially explain the ^{26}Al variations in WLR spinel. Such an explanation would be in line with the contribution of isotopically heavy Si

(and occasionally Mg) from the interior (Fig. 13) and with low $(^{26}Al/^{27}Al)_0'$ ratios observed in the outer part of profile 1 (Fig. 13c).

We also considered what could be the extent of secondary Al-Mg disturbances in the WLR due to solid state exchange with a reservoir devoid of ^{26}Al. The range of model initial $^{26}Al/^{27}Al$ ratios corresponds to a ~20 % exchange for a 1µm spinel crystal during a 6 months heating at 1000 K (Fig. 18) using the self-diffusion coefficient of Mg in spinel from Sheng et al. (1992). This exchange duration becomes 2.5 My at 750 K and 30 My at 720 K. The composition of the co-existing pyroxene can be further calculated in similar conditions using the self-diffusion coefficient of natural diopside averaged over the crystallographic axes as a first approximation (Zhang et al., 2010) and corresponds to a 11 % exchange for 1µm pyroxene crystals at 1000 K (Fig. 18). At lower temperature and for longer durations, the amount of exchange in the pyroxene becomes closer to that in spinel (e.g., 18% at 720 K). Within analytical error, the pyroxene data cannot be distinguished from a canonical isochron, nor from a younger value, nor from an exchanged value (Fig. 18). This calculation shows that late reheating in the solar nebula (e.g., for the highest temperatures) or parent-body metamorphism (e.g., for the lowest temperatures) are possible sources of chronological disturbance and younger apparent WLR ages because spinel may not have preserved the initial ratio. The range of composition in E101.1 spinel is a possible hint for this process, which may has affected all WLR spinels in other CAIs. We note that 750 K may still be too high for the peak metamorphic temperature undergone by Efremovka for which the maximal temperature is probably closer to ~ 600 K by analogy with Leoville and Vigarano of petrologic type and thermal history close to those of Efremovka (Huss and Lewis, 1994; Bonal et al., 2006), which would require unreasonably long duration of metamorphism for

1265 Mg isotope exchange in spinel. However, interpretation of WLR ages in more
1266 metamorphosed meteorites such as Allende must be treated with caution.

1267 Given the uncertainties on the variations of ^{26}Al content in WLR spinel, the initial
1268 $^{26}Al/^{27}Al$ ratio and age of the WLR are probably best given by the converging values of
1269 profile 2 and area 4 where the initial value seems best preserved at the contact with the WLR.
1270 This initial ratio of $(5.2\pm0.1) \times 10^{-5}$ (2σ) agrees well with that obtained by a regression
1271 through WLR data if the three spinel analyses with evidence of disturbances are removed, that
1272 is $(5.2\pm0.8) \times 10^{-5}$ (2σ) (Fig. 18). We conclude that the WLR of E101.1 most likely formed
1273 with a canonical initial $^{26}Al/^{27}Al$ ratio. If the canonical ratio corresponds to the time of ^{26}Al
1274 homogenization in the early solar system (e.g., Sahijpal et al., 2000; Mishra and Chaussidon,
1275 2014; Young et al., 2005) and the beginning of its chronological use, this constrains the epoch
1276 of E101.1 closure to capture of xenolithic materials to within a ~100,000 years interval. More
1277 generally, the measured ages of formation of WLR and their age difference with the interior
1278 may not be representative of their true age of formation and many WLR may be essentially
1279 contemporaneous with their host CAI formation within the time resolution of the ^{26}Al
1280 chronometer. In light of evidence for an isotopic continuum between regular CAIs and FUN
1281 CAIs indicated by Ca and Ti isotopes (Park et al., 2014), another important implication of the
1282 present work is that mixing with FUN-like precursor material during CAI formation followed
1283 by partial melting may be an important source of isotopic disturbance of the Al/Mg
1284 systematics that was previously unrecognized. In this case, many Mg isotopic disturbances,
1285 notably in melilite, that were attributed to late secondary processes such as alteration or
1286 metamorphism may in fact be of primary nebular origin.

1287

1288

1289 *4.7. O isotope reservoirs during E101.1 formation*

1290

1291 The coupling of O isotopes with Si and Mg isotope compositions indicates several
1292 episodes of ^{16}O-rich CAI proto-material dissolution into a ^{16}O-poor melt. This is clearly the
1293 case for (1) the ^{16}O-rich spinel clusters, which reacted with a ^{16}O-poor host melt, resulting in
1294 local ^{16}O-enrichments in the gehlenitic products of the reaction and (2) the ^{16}O-rich sinuous
1295 pyroxene fragments, which mixed with a ^{16}O-poor parental host melt to produce the
1296 intermediate compositions observed in areas 3 and 4 and in subinclusion 1. The strong ^{16}O-
1297 depletion observed in the Sc-Zr-rich pyroxene, which likely crystallized upon interaction
1298 between the host melt and UR perovskite, some of which being ^{16}O-rich as observed in PerB,
1299 further testifies to a strongly ^{16}O-depleted host melt from which most of the melilite in E101.1
1300 crystallized. The sluggish self-diffusion of O in Ca-rich pyroxene (Ryerson and McKeegan,
1301 1994), requires that this ^{16}O-depletion is primary. The residual Δ^{17}O heterogeneity within
1302 individual areas (Table 2) and the possible oxygen isotope mass fractionation relative to the
1303 CCAM line observed in the Sc-Zr-rich pyroxene and some of the ^{16}O-poor melilite (Fig. 7,
1304 Table 2) are well accounted for by assimilation of several ^{16}O-rich proto-CAIs into a
1305 dominantly ^{16}O-poor melt that had undergone partial evaporation.

1306 All these observations point toward a ^{16}O-poor CAI precursor at the origin of the
1307 E101.1 parental melt (or a strong ^{16}O-depletion occurring during melting), before the host
1308 CAI trapped both the spinel clusters and the sinuous pyroxene xenoliths. The ^{16}O-depletion
1309 must therefore be contemporaneous with the main CAI growth stage by coagulation of proto-
1310 CAIs in the solar protoplanetary disk. The Al/Mg systematics of E101.1 further suggests that
1311 this growth occurred while the solar system ^{26}Al/^{27}Al ratio was canonical or near canonical. In
1312 agreement with increasing evidence (Yurimoto et al., 1998; Aléon et al., 2007; Aléon, 2016;
1313 Kawasaki et al., 2012, 2017; Katayama et al., 2012; Park et al., 2012; Simon et al., 2011,
1314 2016), this conclusion indicates that both ^{16}O-rich (Δ^{17}O ~ -24‰) and ^{16}O-poor (Δ^{17}O ~ -2‰)

reservoirs previously evidenced in CAIs (Krot et al., 2002) co-existed in the earliest solar system. The formation of the WLR further constrains the end of E101.1 formation to within the first 100,000 years. At this late stage E101.1 had already experienced a ^{16}O-depletion, assimilation of ^{16}O-rich materials and had returned to the ^{16}O-rich environment, where the AR formed as in many CAIs (e.g., Krot et al., 2002; Yoshitake et al., 2005) and where pyroxene from Type B CAIs crystallized (Aléon, 2016). As shown for several CAIs and expected in many CAIs due to similar general O isotope systematics, the ^{16}O-depletion was most likely associated with partial melting/crystallization of melilite (Yurimoto et al., 1998; Aléon, 2016; Kawasaki et al., 2017).

Although these observations may be used to constrain the timing and location of oxygen isotope variations in the solar protoplanetary disk, they nevertheless do not shed light on the carrier phases of the oxygen isotope change between solar (McKeegan et al., 2011) and planetary, nor on the physico-chemical processes at the origin of this isotopic difference between solar and planetary reservoirs. Two other observations regarding E101.1 are more pertinent in that respect. First, the primary component related to FUN inclusions is inferred to be dominantly ^{16}O-poor, which is in line with the proposition that FUN inclusions formed from a primary dust component of interstellar origin depleted in ^{16}O relative to the solar composition (Kööp et al., 2016a; Krot et al., 2010). However, it is not clear if the ^{16}O-poor composition of the FUN component of E101.1 is primary or was acquired during melting by isotope exchange with a ^{16}O-poor gas of near terrestrial composition. We note that the UR perovskite grains present in the host inclusion were probably initially ^{16}O-rich, in agreement with the ^{16}O-rich composition of the sinuous pyroxene, suggesting that most UR materials were initially ^{16}O-rich. The association of the UR perovskite precursor with the FUN component and the associated ^{16}O-depletion are the most ancient events that occurred in the history of E101.1 and their record is partially obliterated by subsequent assimilations. We

refer to this stage as the "cryptic stage" reflecting that it is not possible to be more precise as to where, when and how the ^{16}O-depletion occurred.

The sinuous pyroxene fragments contain complex inclusions of secondary phases including wollastonite and oxidized FeO-rich silicates inferred to be andradite and hedenbergite from electron probe analyses by El Goresy et al. (2002). The present discussion is based on this characterization. We show that these secondary FeO-rich minerals are ^{16}O-poor. They are systematically located in the interior of the sinuous pyroxene and they contributed to the FeO content of the quenched melt region. The host inclusion, by contrast, contains numerous metal inclusions, some of which are quite large. Exsolution of silica, phosphates and V-Fe-oxides (Fig. 4d) from the metal grains is evidence of metamorphism, but most metal grains remain unoxidized. Silicates in the vicinity of metal grains are FeO-free. Although it is widely thought that oxidation and FeO-enrichment of CAI minerals occurred on a parent body in most cases (Brearely and Krot, 2013), these observations strongly suggest that the secondary alteration of the sinuous pyroxene in E101.1 occurred in the protoplanetary disk prior to trapping by the reduced host inclusion (El Goresy et al., 2002). Given that small refractory metal nuggets are present in the sinuous pyroxene fragments, this secondary alteration/oxidation was extremely localized. The conditions of formation of these secondary FeO-silicates are unclear and deserve a detailed study. They point toward existence of a high fO_2 reservoir in the region of CAI formation. This reservoir is not expected from thermodynamic equilibrium considerations (Fedkin and Grossman, 2006; Grossman et al., 2008a) and has a near terrestrial oxygen isotopic composition

Finally, the relationship between O isotopes and chemistry in sinuous pyroxene (Fig. 8), which shows ^{16}O depletions associated with less refractory pyroxene (although both variations are small), points toward beginning ^{16}O depletion in the environment of sinuous pyroxene formation during crystallization. Indeed, the self-diffusion of O in solid pyroxene is

1365 sluggish and a solid state secondary re-equilibration, for instance during assimilation of the
1366 sinuous pyroxene, would not be correlated with chemistry. This suggests that the ^{16}O-rich
1367 environment in the disk was not entirely homogeneous and that ^{16}O-rich and ^{16}O-poor
1368 reservoirs somehow interacted with each other. In the vertical zoning model inferred by Aléon
1369 (2016), this may result from propagation of the surface ^{16}O-depletion toward the cool
1370 midplane. In the horizontal zoning models such as those inferred from self-shielding
1371 associated with the transport of isotopically heavy water ice produced in low temperature
1372 regions (e.g., Yurimoto and Kuramoto, 2004; Lyons and Young, 2005; Young, 2007), this
1373 may correspond to the mixing front, where ^{16}O-poor water vapor equilibrates with the ^{16}O-
1374 rich ambient gas. Similar small variations in ^{16}O-rich hibonite CAIs have been found, which
1375 may also point to variable interactions between the ^{16}O-rich and ^{16}O-poor gas associated with
1376 small temperature differences (Kööp et al., 2016a).
1377
1378
1379 *4.8. Protoplanetary disk context of E101.1 formation*
1380
1381 Our observations have shown that E101.1 is a compound CAI formed from the
1382 coagulation of at least three different precursors (Fig. 19). The first precursor is the
1383 ultrarefractory CAI, rich in perovskite, that constitutes the main mass of E101.1. The sinuous
1384 pyroxene was related to some extent to this initial UR CAI. It was ^{16}O-rich and had near
1385 canonical abundance of ^{26}Al. Perovskite contained ^{48}Ca anomalies. Relative abundances of
1386 REE are suggestive of a complex suite of condensation events, including fractional
1387 condensation of an UR precursor. The second precursor is a F(UN) inclusion with low ^{26}Al
1388 content. The exact conditions of association, melting and evaporation of these two precursors
1389 remain unclear because subsequent capture and partial assimilation events obscured these

1390 early high temperature stages. After coagulation of these two precursors and their subsequent
1391 common thermal history, the main E101.1 host still had a very refractory chemical
1392 composition and (i) had experienced a ^{16}O-depletion, (ii) a strong evaporation, (iii) carried
1393 ^{48}Ca isotope anomalies, (iv) had heterogeneous ^{26}Al content. After this cryptic stage (Fig.
1394 19a), the main E101.1 captured spinel-rich proto-CAIs, possibly of the common fine-grained
1395 spinel-rich CAI type and assimilated the sinuous pyroxene-rich UR CAI. In which order these
1396 two capture and partial dissolution events occurred is again not completely clear. Isotopic
1397 mixing evidence favors capture of the spinel-CAIs first and sinuous pyroxene last (Fig. 19a).
1398 Contrary to the cryptic stage, which can only be inferred from considerations on isotopic and
1399 chemical properties of the E101.1 main host, these last two stages are recorded in the
1400 petrography of E101.1 and can be visually identified (Fig. 19b). Finally, the WLR formed by
1401 condensation into a possibly melted and evaporated outer layer of E101.1 and induced a
1402 chemical and isotopic zoning of the outer margins immediately inside the WLR.
1403 It has recently been shown that turbulent transport within the innermost 1 astronomical
1404 unit (AU) of a thermally zoned protoplanetary disk before the end of protostellar envelope
1405 collapse yields highly variable thermal histories for the various precursors (Taillifet et al.,
1406 2014). Extraction of CAIs from the hot zone in such an environment can be realized in at
1407 most a few 1000 years. As a result, the various precursors of E101.1 may have collided
1408 sequentially with each other during such a turbulent journey through the innermost portion of
1409 the hot zone of the earliest solar protoplanetary disk. Although not recognized in regular
1410 CAIs, the growth of mm to cm sized CAIs through such a series of collisions of numerous
1411 precursors may be the standard case of CAI formation since collisions with the nearest
1412 neighbors, i.e., between precursors of similar or only marginally different thermal histories,
1413 are likely to be statistically favored. The growing identification of compound CAIs supports
1414 this conclusion (e.g., El Goresy et al., 2002; Aléon et al., 2005, 2007; MacPherson et al.,

2012; Ivanova et al., 2015; Simon et al., 2017). The numerical study of the collisional evolution of CAIs by coagulation and fragmentation in a turbulent hot inner disk indicates rapid growth of mm- to cm-sized objects at collisional equilibrium in a plastic (probably partially molten) state (Charnoz et al., 2015). Such a collisional evolution agrees with aggregation of multiple precursors in E101.1 in a partially molten state and provides a natural explanation for the observed spatial decoupling between different isotope systems and between isotope compositions and mineral chemistry.

Nevertheless, the UR REE and light isotopic composition in the sinuous pyroxene fragments point to a rapid removal of its precursors from the hottest region of the disk and their rapid transport toward the exterior. It remains to be demonstrated to what extent the lack of re-equilibration with the ambient gas fits with the velocities during turbulent transport and the residence time at a given temperature (Taillifet et al., 2014).

Finally, isotopic equilibration between host and xenoliths during capture and assimilation in a partially molten state is a closed-system behavior that requires isolation of the CAI from the ambient gas, notably because the self-diffusion of O in Ca-Al-rich silicate melts is rapid (Oishi et al., 1974). Mixing relationships are thus expected to be blurred if the partial melt equilibrates with the gas. While this seems not difficult to achieve for Mg and Si due to vastly differing abundances in the CAI and the nebular gas having low partial pressures of Mg and SiO gas, the case of O is more problematic. Physical isolation of melt pockets inside the CAI is unrealistic in light of the distribution of xenolithic fragments and mixed areas, which reach the CAI surface. Chemical isolation is thus required. One way to prevent E101.1 partial melts from equilibrating with the ambient CO or H_2O gas during capture and assimilation (i.e., partial melting) is melting in a diffuse near-vacuum environment with low O abundance and thus low total pressure at solar H/O ratio. Nagahara and Ozawa (2012) calculated that in a closed system with O abundances in the gas about 100 times lower than in

a canonical nebula, the final composition of a melt exchanging with the gas is within a few ‰ of the starting composition. However, temperatures in diffuse regions such as the inner edge of the gas disk are likely to be very high and thus to favor a strong evaporation not indicated by the Mg and Si isotopic composition during assimilation of the sinuous pyroxene. In addition, in an open system where the ambient gas can be considered infinite, the partial melt will ultimately equilibrate with the gas, unless the cooling rate is rapid enough to preserve the initial composition. In this case, however, O isotope mass fractionation may be expected depending on the relative timescales of diffusion in the melt and evaporation (Ozawa and Nagahara, 2001). A closed-system behavior of E101.1 during partial melting and partial assimilation of sinuous pyroxene thus remains difficult to explain and to place in an astrophysical context. For that purpose, a better knowledge of isotope exchange rates with relevant astrophysical species such as CO and H_2O in protoplanetary disk conditions (e.g., Yu et al., 1995; Boesenberg et al., 2005, 2016; DiRocco and Pack, 2015) is required.

5. Summary and conclusions

The multi-isotopic study of E101.1 sheds light on the nature of its various refractory components and on their mixing relationships. Possible precursors have been proposed after disentangling the effects of mixing and partial assimilation. It is found that the final E101.1 CAI results from the coagulation and partial melting of at least three different CAI components:

1. An unusual UR CAI dominated by ^{16}O-rich Al-diopside ($\Delta^{17}O \leq -20‰$) with light Mg and Si isotopic composition (mass fractionation ~ -3.5‰/amu in both cases) resulting from kinetic effects, most likely during condensation out of equilibrium. This Al-diopside is

1465 now present as multiple relict sinuous pyroxene fragments and locally encloses the ^{16}O-poor
1466 FeO-rich minerals (Δ^{17}O up to ~ -4.5 ‰) described in El Goresy et al. (2002).

1467 2. A melilite-rich UR and FUN host CAI with abundant perovskite, enriched in heavy
1468 Mg and Si isotopes by evaporation (δ^{25}Mg and *F*Si up to ~+7‰ and ~+8‰, respectively).
1469 Decoupling of Mg and Si isotopes points toward dissolution of spinel with low δ^{25}Mg after
1470 evaporation. Isotopic mixing with the sinuous pyroxene CAI in some regions indicates that
1471 the precursor was probably an ultra-refractory melt with little SiO_2 and barely any MgO. The
1472 subinclusion 1 identified by El Goresy et al. (2002) is most likely a region of the host that was
1473 partially crystallized as gehlenite at the time of sinuous pyroxene capture and remelted
1474 subsequently. The calculated pre-evaporation composition indicates that the initial precursor
1475 condensed as a hibonite-perovskite-melilite assemblage in agreement with the abundance of
1476 melilite and perovskite and evidence of a link with hibonite-rich FUN inclusions.

1477 3. The origin of spinel clusters is not as clear but we favor an extraneous source based
1478 on several lines of evidence regarding the chemistry, O and Mg isotopes indicating exchange
1479 and partial re-equilibration with the host melilite.

1480 The whole CAI is surrounded by a WLR and an accretionary forsterite-rich rim,
1481 having isotopic systematics indicative of formation by condensation from a ^{16}O-rich gas
1482 (Δ^{17}O ~ -22‰) with interactions with the evaporated interior. The Al/Mg systematics
1483 suggests an early formation (~canonical) of the WLR, approximately contemporaneous of that
1484 of the interior CAI with $(^{26}Al/^{27}Al)_0 \sim (5.2\pm0.1) \times 10^{-5}$, but also secondary perturbations,
1485 which could possibly yield erroneously young WLR formation ages in CAIs if not properly
1486 identified ($(^{26}Al/^{27}Al)_0'$ ratios down to 3.7×10^{-5} in individual spinel grains).

1487 The identification of mixing and interactions between the various precursor CAI
1488 components in E101.1 is facilitated owing to the large isotopic differences between the
1489 lithological units that result from different thermal histories (e.g., condensation vs

evaporation) or from the sampling of different cosmochemical reservoirs (e.g ^{16}O-rich vs ^{16}O-poor or ^{26}Al-rich vs ^{26}Al-poor). Some of these interactions produced isotopic heterogeneities that are also seen in other CAIs with lower amplitude, and remain poorly understood. For instance, many heterogeneities in the Al/Mg systematics are attributed to poorly documented late stage perturbations, but the E101.1 results suggest that they may also result from primary mixing processes between ^{26}Al-rich and ^{26}Al-poor components that are obscured by subsequent partial melting. Compared to the E101.1 precursors that have large isotopic differences, the closer CAI precursors are in chemistry and isotopic composition, the more difficult it is to identify these effects.

The study of E101.1 also sheds light on the origin of O isotopic variations in CAIs. It has been long debated whether CAIs record primary isotopic heterogeneities in the solar protoplanetary disk or underwent secondary perturbations that reset the isotopic composition of some minerals. Recent studies show strong support in favor of the co-existence of ^{16}O-rich and ^{16}O-poor reservoirs early in the protoplanetary disk. The O isotope systematics of E101.1 clearly supports these conclusions and demonstrates that igneous CAIs underwent a ^{16}O-depletion at high temperature contemporaneously with their growth by coagulation.

Acknowledgements

Jean-Noël Rouzaud provided access to the FEG-SEM operated by Damien Deldicque in the geology department at the ENS in Paris. Emeline Charon helped with the ENS FEG-SEM imaging and for a few oxygen isotopes analyses. George Jarzebinski maintained the UCLA IMS 1270 ion probe. Frederic Couffignal and Michel Fialin from the CAMPARIS facility helped with the electron probe analyses. Interaction with Larry Grossman was appreciated,

Ruslan Mendybaev is thanked for providing condensation trajectories from a submitted manuscript. In depth reviews and comments by the AE, Alexander N. Krot, and the three reviewers Andrew M. Davis, Justin Simon and Steven Simon were appreciated. This project was supported by a CSNSM-UCLA international cooperation PICS program from the CNRS, by the PNP-INSU French national program of planetology, and by the NASA Cosmochemistry Program. The UCLA ion microprobe laboratory is partially supported by a grant from the NSF Instrumentation and Facilities Program.

References

Aléon J. (2016) Oxygen isotopes in the early protoplanetary disk inferred from pyroxene in a classical type B CAI. *Earth Planet. Sci. Lett.* **440**, 62-70.

Aléon J., Krot A. N. and McKeegan K. D. (2002) Calcium-aluminum-rich inclusions and amoeboid olivine aggregates from the CR carbonaceous chondrites. *Meteorit. Planet. Sci.* **37**, 1729-1755.

Aléon J., Krot A. N., McKeegan K. D., MacPherson G. J. and Ulyanov A. A. (2005) Fine-grained, spinel-rich inclusions from the reduced CV chondrite Efremovka: II. Oxygen isotopic compositions. *Meteorit. Planet. Sci.* **40**, 1043-1058.

Aléon J., El Goresy A. and Zinner E. (2007) Oxygen isotope heterogeneities in the earliest protosolar gas recorded in a meteoritic calcium-aluminum-rich inclusion. *Earth Planet. Sci. Lett.* **263**, 114-127.

Bodénan J.-D., Starkey N. A., Russell S. S., Wright I. P. and Franchi I. A. (2014) An oxygen isotope study of Wark-Lovering rims on Ttype A CAIs in primitive carbonaceous chondrites. *Earth Planet. Sci. Lett.* **401**, 327-336.

1540 Boesenberg J. S., Young E. D., Ziegler K. and Hewins R. H. (2005) Evaporation and the
1541 absence of oxygen isotopic exchange between silicate melt and carbon monoxide gas at
1542 nebular pressures. *Meteorit. Planet. Sci.* **40**: suppl., A22.
1543 Boesenberg J. S., Young E. D., Kohl I. and Parman S. W. (2016) Oxygen isotopic exchange
1544 between carbon monoxide gas and silicate melt: Implications for the early solar nebula.
1545 *Lunar Planet. Sci. 47*, Lunar Planet. Inst., Houston. #2481(abstr.).
1546 Bolser D., Zega T. J., Asaduzzaman A., Bringuier S., Simon S. B., Grossman L., Thompson
1547 M. S. and Domanik K. J. (2016) Microstructural analysis of Wark-Lovering in the Allende
1548 and Axtell CV3 chondrites: Implications for high-temperature nebular processes. *Meteorit.*
1549 *Planet. Sci.* **51**, 743-756.
1550 Bonal L., Quirico E., Bourot-Denise M., and Montagnac G. (2006) Determination of the
1551 petrologic type of CV3 chondrites by Raman spectroscopy of included organic matter.
1552 *Geochim. Cosmochim. Acta* **70**, 1849-1863.
1553 Boss A. P., Alexander C. M. O'D. and Podolak M. (2012) Cosmochemical consequences of
1554 particle trajectories during FU Orionis outbursts by the early Sun. *Earth Planet. Sci. Lett.*
1555 **345-348**, 18-26.
1556 Brearley A. J. and Krot A. N. (2013) Metasomatism in the early Solar System: The record
1557 from chondritic meteorites. In *Metasomatism and the chemical transformation of rocks*
1558 (Eds. D. E. Harlov and H. Austrheim), Springer-Verlag, Berlin Heidelberg, pp. 659-789.
1559 Bullock E. S., Knight K. B., Richter F. M., Kita N. T., Ushikubo T., MacPherson G. J., Davis
1560 A. M. and Mendybaev R. A. (2013) Mg and Si isotopic fractionation patterns in types B1
1561 and B2 CAIs: Implications for formation under different nebular conditions. *Meteorit.*
1562 *Planet. Sci.* **48**, 1440-1458.
1563 Caillet Komorowski C. L. V., Zinner E. K., McKeegan K. D., Hervig R. and Buseck P. R.
1564 (2007) The White Angel: A unique wollastonite-bearing, mass-fractionated refractory

1565 inclusion from the Leoville CV3 carbonaceous chondrite. *Meteorit. Planet. Sci.* **42**, 1159-
1566 1182.

1567 Charnoz S., Aléon J., Chaumard N., Baillie K. and Taillifet E. (2015) Growth of calcium-
1568 aluminum-rich inclusions by coagulation and fragmentation in a turbulent protoplanetary
1569 disk: Observations and simulations. *Icarus* **252**, 440-453.

1570 Clayton R. N. and Mayeda T. K. (1984) The oxygen isotope record in Murchison and other
1571 carbonaceous chondrites. *Earth Planet Sci. Lett.* **67**, 151-161.

1572 Clayton R. N., MacPherson G. J., Hutcheon I. D., Davis A. M., Grossman L., Mayeda T. K.,
1573 Molini-Velsko C., Allen J. M.,and El Goresy A. (1984) Two forsterite-bearing FUN
1574 inclusions in the Allende meteorite. *Geochim. Cosmochim. Acta* **48**, 535–548.

1575 Clayton R. N., Hinton R. W. and Davis A.M. (1988) Isotopic variations in the rock-forming
1576 elements in meteorites. *Phil. Trans. R. Soc. Lond. A* **325**, 483-501.

1577 Connolly, H. C. Jr., and Burnett D. S. (2003) On type B CAI formation: Experimental
1578 constraints on fO_2 variations in spinel minor element partitioning and reequilibration
1579 effects. *Geochim. Cosmochim. Acta* **67**, 4429-4434.

1580 Cosarinsky M., McKeegan K. D., Hutcheon I. D., Weber P. and Fallon S. (2005a)
1581 Magnesium and oxygen isotopic study of the Wark-Lovering rim around a fluffy type A
1582 inclusion from Allende. *Lunar Planet. Sci. 36*, Lunar Planet. Inst., Houston. #2105(abstr.).

1583 Cosarinsky M., Taylor D. J., McKeegan K. D. and Hutcheon I. D. (2005b) Mg isotopic study
1584 of Wark-Lovering rims in type A inclusions from CV chondrites: formation mechanisms
1585 and timing. *Meteorit. Planet. Sci.* **40**: suppl., A34.

1586 Cosarinsky M., Taylor D. J. and McKeegan K. D. (2006) Aluminum-26 model ages of
1587 hibonite and spinel from type A inclusions in CV chondrites. *Lunar Planet. Sci. 37*, Lunar
1588 Planet. Inst., Houston. #2357(abstr.).

1589 Davis A. M. and Grossman L. (1979) Condensation and fractionation of rare earths in the
1590 solar nebula. *Geochim. Cosmochim. Acta* **43**, 1611-1632.
1591 Davis A. M. and Richter F. M. (2014) Condensation and evaporation of solar system
1592 materials. In *Meteorites and Cosmochemical Processes* (Ed. A. M. Davis), Vol. 1 Treatise
1593 on Geochemistry, 2nd Ed. (Exec. Eds. H. D. Holland and K. K. Turekian), Elsevier, Oxford,
1594 pp. 335-360.
1595 Davis A. M., MacPherson G. J., Clayton R. N., Mayeda T. K., Sylvester P. J., Grossman L.,
1596 Hinton R. W. and Laughlin J. R. (1991) Melt solidification and late-stage evaporation in
1597 the evolution of a FUN inclusion from the Vigarano C3V chondrite. *Geochim. Cosmochim.*
1598 *Acta* **55**, 621-637.
1599 Davis A. M., Richter F. M., Mendybaev R. A., Janney P. E., Wadhwa M. and McKeegan K.
1600 D. (2015) Isotopic mass fractionation laws for magnesium and their effects on ^{26}Al-^{26}Mg
1601 systematics in solar system materials. *Geochim. Cosmochim. Acta* **158**, 245-261.
1602 Davis A. M., Zhang J., Greber N. D., Hu J., Tissot F. L. H. and Dauphas N. (2018) Titanium
1603 isotopes and rare earth patterns in CAIs: Evidence for thermal processing and gas-dust
1604 decoupling in the protoplanetary disk. *Geochim. Cosmochim. Acta* **221**, 275-295.
1605 Di Rocco T. and Pack A. (2015) Triple oxygen isotope exchange between chondrule melt and
1606 water vapor: An experimental study. *Geochim. Cosmochim. Acta* **164**, 17-34.
1607 Dyl K. A., Simon J. I. and Young E. D. (2011) Valence state of titanium in the Wark-
1608 Lovering rim of a Leoville CAI as a record of progressive oxidation in the early Solar
1609 Nebula. *Geochim. Cosmochim. Acta* **75**, 937-949.
1610 El Goresy A., Zinner E., Matsunami S., Palme H., Spettel B., Lin Y. and Nazarov M. (2002)
1611 Efremovka 101.1: A CAI with ultrarefractory REE patterns and enormous enrichments of
1612 Sc, Zr and Y in fassaite and perovskite. *Geochim. Cosmochim. Acta* **66**, 1459-1491.

1613 Esat T. M., Lee T., Papanastassiou D. A. and Wasserburg G. J. (1978) Search for ^{26}Al effects
1614 in the Allende FUN Inclusion C1. *Geophys. Res. Lett.* **5**, 807-810.
1615 Fagan T. J., Krot, A. N., Keil K. and Yurimoto H. (2004) Oxygen isotopic alteration in Ca-
1616 Al-rich inclusions from Efremovka: Nebular or parent body setting? *Meteorit. Planet. Sci.*
1617 **39**, 1257-1272.
1618 Fahey A. J., Zinner E. K., Crozaz G. and Kornacki A. S. (1987) Microdistributions of Mg
1619 isotopes and REE abundances in a Type A calcium-aluminum-rich inclusion from
1620 Efremovka. *Geochim. Cosmochim. Acta* **51**, 3215-3229.
1621 Fahey A. J., Zinner E., Kurat G. and Kracher A. (1994) Hibonite-hercynite inclusion HH-1
1622 from the Lancé (CO3) meteorite: The history of an ultrarefractory CAI. *Geochim.*
1623 *Cosmochim. Acta* **58**, 4779-4793.
1624 Fedkin A. V. and Grossman L. (2006) The fayalite content of chondritic olivine: Obstacle to
1625 understanding the condensation of rocky material. In *Meteorites and the Early Solar*
1626 *System II* (eds. D. S. Lauretta and H. Y. McSween, Jr.). Univ. Arizona Press, Tucson,
1627 Arizona. pp. 279–294.
1628 Galy A., Yoffe O., Janney P. E., Williams R. W., Cloquet C., Alard O., Halicz L., Wadhwa
1629 M., Hutcheon I. D., Ramon E. and Carignan J. (2003) Magnesium isotope heterogeneity of
1630 the isotopic standard SRM980 and new reference materials for magnesium–isotope-ratio
1631 measurements. *J. Anal. Atom. Spec.* **18**, 1352–1356.
1632 Gautason B. and Muehlenbachs K. (1993) Oxygen diffusion in perovskite: Implications for
1633 electrical conductivity in the lower mantle. *Science* **260**, 518-521.
1634 Goswami J. N., Srinivasan G. and Ulyanov A. A. (1994) Ion microprobe studies of
1635 Efremovka CAIs: I. Magnesium isotope composition. *Geochim. Cosmochim. Acta* **58**, 431-
1636 447.
1637 Grossman L., Beckett J. R., Fedkin A. V., Simon S. B. and Ciesla F. J. (2008a) Redox

conditions in the solar nebula: Observational, experimental, and theoretical constraints. In *Oxygen in the Solar System* (eds. G. J. MacPherson, D. W. Mittlefehldt, J. H. Jones, and S. B. Simon). Mineral. Soc. Am., Chantilly, Virginia. pp. 93–140.

Grossman L., Simon S. B., Rai V. K., Thiemens M. H., Hutcheon I. D., Williams R. W., Galy A., Ding T., Fedkin A. V., Clayton R. N. and Mayeda T. K. (2008b) Primordial compositions of refractory inclusions. *Geochim. Cosmochim. Acta* **72**, 3001-3021.

Hinton R W., Davis, A M., Scatena-Wachel D E., Grossman L. and Draus, R J. (1988) A chemical and isotopic study of hibonite-rich refractory inclusions in primitive meteorites. *Geochim. Cosmochim. Acta* **52**, 2573-2598

Holst J. C., Olsen M. B., Paton C., Nagashima K., Schiller M., Wielandt D., Larsen K. K., Connelly J. N., Jorgensen J. K., Krot A. N., Nordlund A. and Bizzarro M. (2013) ^{182}Hf-^{182}W age dating of a ^{26}Al-poor inclusion and implications for the origin of short-lived radioisotopes in the early Solar System. *Proc. Nat. Acad. Sci. USA.* **110**, 8819-8823.

Huss G. R. and Lewis R. S. (1994) Noble gases in presolar diamonds II: Component abundances reflect thermal processing. *Meteoritics* **29**, 811-829.

Ireland T. R. (1988) Correlated morphological, chemical and isotopic characteristics of hibonites from the Murchison carbonaceous chondrite. *Geochim. Cosmochim. Acta* **52**, 2827-2839.

Ireland T. R. (1990) Presolar isotopic and chemical signatures in hibonite-bearing refractory inclusions from the Murchison carbonaceous chondrite. *Geochim. Cosmochim. Acta* **54**, 3219-3237.

Itoh S. and Yurimoto H. (2003) Contemporaneous formation of chondrules and refractory inclusions in the early Solar System. *Nature* **423**, 728-731.

1661 Ivanova M. A., Krot A. N., Nagashima K. and MacPherson G. J. (2012) Compound
1662 ultrarefractory CAI-bearing inclusions from CV3 carbonaceous chondrites. *Meteorit.*
1663 *Planet. Sci.* **47**, 2107-2127.
1664 Ivanova M. A., Lorenz C. A., Shuvalov V. V., Krot A. N., MacPherson G. J. and Bizzarro M.
1665 (2014) Plastically-deformed igneous Calcium-Aluminum-rich Inclusions from CV
1666 carbonaceous chondrites: Clues to a nature of CAI melting events. *Lunar Planet. Sci. 45*,
1667 Lunar Planet. Inst., Houston. #2166(abstr.).
1668 Ivanova M. A., Lorenz C. A., Krot A. N. and MacPherson G. J. (2015) A compound Ca-Al-
1669 rich inclusion from CV3 chondrite Northwest Africa 3118: Implications for understanding
1670 processes during CAI formation. *Meteorit. Planet. Sci,* **50**, 1512-1528.
1671 Jacobsen B., Yin Q.-Z., Moynier F., Amelin Y., Krot A. N., Nagashima K., Hutcheon I. D.,
1672 Palme H. (2008). ^{26}Al-^{26}Mg and ^{207}Pb-^{206}Pb systematics of Allende CAIs: Canonical solar
1673 initial ^{26}Al/^{27}Al ratio reinstated. *Earth Planet. Sci. Lett.* **272**, 353-364.
1674 Katayama J., Itoh S. and Yurimoto H. (2012) Oxygen isotopic zoning of reversely zoned
1675 melilite crystals in a fluffy type A Ca-Al-rich inclusions from the Vigarano meteorite.
1676 *Meteorit. Planet. Sci*. **47**, 2094-2106.
1677 Kawasaki N., Sakamoto N. and Yurimoto H. (2012) Oxygen isotopic and chemical zoning of
1678 melilite crystals in a type A Ca-Al-rich inclusion of Efremovka CV3 chondrite. *Meteorit.*
1679 *Planet. Sci.* **47**, 2084-2093.
1680 Kawasaki N., Itoh S., Sakamoto N. and Yurimoto H. (2017) Chronological study of oxygen
1681 isotope composition for the solar protoplanetary disk recorded in a fluffy Type A CAI
1682 from Vigarano. *Geochim. Cosmochim. Acta* **201**, 83-102.
1683 Keller L. P., Needham A. W. and Messenger S. (2013) A FIB/TEM study of a complex
1684 Wark-Lovering rim on a Vigarano CAI. *76th Annual Meteoritical Society Meeting*,
1685 #5300(abstr.).

1686 Kita N. T., Ushikubo T., Knight K. B., Mendybaev R. A., Davis A. M., Richter F. M. and
1687 Fournelle J. H. (2012) Internal ^{26}Al-^{26}Mg isotope systematics of a Type B CAI: Remelting
1688 of refractory precursor solids. *Geochim. Cosmochim. Acta* **86**, 37-51.

1689 Knight K. B., Kita N. T., Mendybaev R. A., Richter F. M., Davis A. M. and Valley J. W.
1690 (2009) Silicon isotopic fractionation of CAI-like vacuum evaporation residues. *Geochim.*
1691 *Cosmochim. Acta* **73**, 6390-6401.

1692 Kööp L., Davis A. M., Nakashima D., Park C., Krot A. N., Nagashima K., Tenner T. J., Heck
1693 P. R. and Kita N. T. (2016a) A link between oxygen, calcium and titanium isotopes in
1694 ^{26}Al-poor hibonite-rich CAIs from Murchison and implications for the heterogeneity of
1695 dust reservoirs in the solar nebula. *Geochim. Cosmochim. Acta* **189**, 70-95.

1696 Kööp L., Nakashima D., Heck P. R., Kita N. T., Tenner T. J., Krot A. N., Nagashima K., Park
1697 C. and Davis A. M. (2016b) New constraints on the relationship between ^{26}Al and oxygen,
1698 calcium and titanium isotopic variations in the early Solar System from a multielement
1699 isotopic study of spinel-hibonite inclusions. *Geochim. Cosmochim. Acta* **184**, 151-172.

1700 Kööp L., Nakashima D., Heck P. R., Kita N. T., Tenner T. J., Krot A. N., Nagashima K., Park
1701 C. and Davis A. M. (2018) A multielement isotopic study of refractory FUN and F CAIs:
1702 Mass-dependent and mass-independant isotope effects. *Geochim. Cosmochim. Acta* **221**,
1703 296-317.

1704 Krot A. N., Ulyanov A. A., Meibom A. and Keil K. (2001) Forsterite-rich accretionary rims
1705 around Ca,Al-rich inclusions from the reduced CV3 chondrite Efremovka. *Meteorit.*
1706 *Planet. Sci.* **36**, 611-628.

1707 Krot A. N, McKeegan K. D., Leshin L. A. and MacPherson G. J. (2002) Existence of an ^{16}O-
1708 rich gaseous reservoir in the solar nebula. *Science* **295**, 1051-1054.

1709 Krot A. N., MacPherson G. J., Ulyanov A. A. and Petaev M. (2004a) Fine-grained, spinel-
1710 rich inclusions from the reduced CV chondrites Efremovka and Leoville : Mineralogy,
1711 petrology and bulk chemistry. *Metorit. Planet. Sci.* **39**, 1517-1553

1712 Krot A. N., Petaev M. I., Russell S. S., Itoh S., Fagan T. J., Yurimoto H., Chizmadia L.,
1713 Weisberg M. K., Komatsu M., Ulyanov A. A. and Keil K. (2004b) Amoeboid olivine
1714 aggregates and related objects in carbonaceous chondrites: records of nebular and asteroid
1715 processes. *Chem. Erde* **64**, 185-239.

1716 Krot A. N., Nagashima K., Ciesla F. J., Meyer B. S., Hutcheon I. D., Davis A. M., Huss G. R.
1717 and Scott E. R. D. (2010) Oxygen isotopic composition of the Sun and mean oxygen
1718 isotopic composition of the protosolar silicate dust: evidence from refractory inclusions.
1719 *Astrophys. J.* **713**, 1159-1166.

1720 Krot A. N., Nagashima K., Wasserburg G. J., Huss G. R., Papanastassiou D., Davis A. M.,
1721 Hutcheon I. D. and Bizarro M. (2014). Calcium-aluminum-rich inclusions with
1722 fractionation and unknown nuclear effects (FUN CAIs): I. Mineralogy, petrology and
1723 oxygen isotopic compositions. *Geochim. Cosmochim. Acta* **145**, 206-247.

1724 Krot A. N., Nagashima K., van Kooten E. M. M. and Bizzarro M. (2017) High-temperature
1725 rims around calcium-aluminum-rich inclusions from the CR, CB and CH carbonaceous
1726 chondrites. *Geochim. Cosmochim. Acta* **201**, 155-184.

1727 Larsen K. K., Trinquier A., Paton C., Schiller M., Wielandt D., Ivanova M. A., Connelly J.
1728 N., Nordlund A., Krot A. N., and Bizarro M. (2011) Evidence for magnesium isotope
1729 heterogeneity in the solar protoplanetary disk. *Astrophys. J.* **735**, L37

1730 Liu M.-C., McKeegan K. D., Goswami J. N., Marhas K. K., Sahijpal S., Ireland T. R. and
1731 Davis A. M. (2009) Isotopic records in CM hibonites: Implications for timescales of
1732 mixing of isotope reservoirs in the solar nebula. *Geochim. Cosmochim. Acta* **73**, 5051-
1733 5079.

1734 Liu M.-C., Chaussidon M., Göpel C. and Lee T. (2012) A heterogeneous solar nebula as
1735 sampled by CM hibonite grains. *Earth Planet. Sci. Lett.* **327-328**, 75-83.

1736 Lodders K. (2003) Solar system abundances and condensation temperatures of the elements.
1737 *Astrophys. J.* **591**, 1220-1247.

1738 Lyons J. R. and Young E. D. (2005) CO self-shielding as the origin of oxygen isotope
1739 anomalies in the early solar nebula. *Nature* **435**, 317-320.

1740 MacPherson G. J. (2014) Calcium-Aluminum-rich inclusions in chondritic meteorites. In
1741 *Meteorites and Cosmochemical Processes,* (Ed. A. M. Davis), Vol. 1 Treatise on
1742 Geochemistry, 2nd Ed. (Exec. Eds. H. D. Holland and K. K. Turekian), Elsevier, Oxford,
1743 pp. 139-179.

1744 MacPherson G. J. and Davis A. M. (1994) Refractory inclusions in the prototypical CM
1745 chondrite, Mighei. *Geochim. Cosmochim. Acta* **58**, 5599-5625.

1746 MacPherson G. J., Bullock E. S., Janney P. E., Kita N. T., Ushikubo T., Davis A. M.,
1747 Wadhwa M. and Krot A. N. (2010) Early solar nebula condensates with canonical, not
1748 supracanonical, initial $^{26}Al/^{27}Al$ ratios. *Astrophys. J. Lett.* **711**, L117-L121.

1749 MacPherson G. J., Kita N. T., Ushikubo T., Bullock E. S. and Davis A. M. (2012) Well-
1750 resolved variations in the formation ages for Ca-Al-rich inclusions in the early solar
1751 system. *Earth Planet. Sci. Lett.* **331-332**, 43-54.

1752 Mane P., Bose M. and Wadhwa M. (2015) Resolved time difference between Calcium-
1753 Aluminum-rich inclusions and their Wark-Lovering rims inferred from Al-Mg chronology
1754 of two inclusions from a CV3 carbonaceous chondrite. *Lunar Planet. Sci. 46*, Lunar Planet.
1755 Inst., Houston. #2898(abstr.).

1756 Marin-Carbonne J., McKeegan K. D., Davis A. M., MacPherson G. J., Mendybaev R.A. and
1757 Richter F. M. (2012) O, Si and Mg isotopic compositions of FUN inclusion Vigarano
1758 1623-5. *Lunar Planet. Sci. 43*, Lunar Planet. Inst., Houston. #1687(abstr.).

1759 McKeegan K. D., Kallio A. P. A., Heber V. S., Jarzebinski G., Mao P. H., Coath C. D.,
1760 Kunihiro T., Wiens R. C., Nordholt J. E., Moses R. W., Reisenfeld D. B., Jurewicz A. J. G.
1761 and Burnett D. S. (2011) The oxygen isotopic composition of the Sun inferred from
1762 captured solar wind. *Science* **332**, 1528-1532.

1763 Mendybaev R. A., Richter F. M., Georg R. B., Janney P. E., Spicuzza M. J., Davis A. M. and
1764 Valley J. W. (2013) Experimental evaporation of mg- and Si-rich melts: Implications for
1765 the origin and evolution of FUN CAIs. *Geochim. Cosmochim. Acta* **123**, 368-384.

1766 Mendybaev R. A., Williams C. D., Spicuzza M. J., Richter F. M., Valley J. W., Fedkin A. V.
1767 and Wadhwa M. (2017) Thermal and chemical evolution in the early Solar System as
1768 recorded by FUN CAIs: Part II - Laboratory evaporation of potential CMS-1 precursor
1769 material. *Geochim. Cosmochim. Acta* **201**, 49-64.

1770 Mishra R. and Chaussidon M. (2014) Timing and extent of Mg and Al isotopic
1771 homogenization in the early solar system. *Earth Planet. Sci. Lett.* **390**, 318-326.

1772 Nagahara H. and Ozawa K. (2012) The role of exchange reactions in oxygen isotope
1773 fractionation during CAI and chondrule formation. *Meteorit. Planet. Sci.* **47**, 1209-1228.

1774 O'Hara M. J. and Biggar G. M. (1969) Diopside + spinel equilibria, anorthite and forsterite
1775 reaction relationships in silica-poor liquids in the system CaO-MgO-Al_2O_3-SiO_2 at
1776 atmospheric pressure and their bearing on the genesis of melilitites and nephelinites. *Amer.*
1777 *J. Sci.* **267A**, 364-390.

1778 Oishi Y., Terai R. and Ueda H. (1974) Oxygen diffusion in liquid silicates and relation to
1779 their viscosity. In *Mass Transport in Ceramics* (eds. A. R. Cooper and A. H. Heuer).
1780 Plenum press, pp. 297-310.

1781 Onuma K. and Kimura M. (1978) Study of the system $CaMgSi_2O_6$-$CaFe^{3+}AlSiO_6$-$CaAl_2SiO_6$-
1782 $CaTiAl_2O_6$: II. The join $CaMgSi_2O_6$-$CaAl_2SiO_6$-$CaTiAl_2O_6$ and its bearing on the Ca-Al-
1783 rich inclusions in carbonaceous chondrite. *J. Fac. Sci. Hokkaido Univ. Ser. IV* **18**, 215-236.
1784 Ozawa K. and Nagahara H. (2001) Chemical and isotopic fractionations by evaporation and
1785 their cosmochemical implications. *Geochim. Cosmochim. Acta* **65**, 521-540.
1786 Paque J. M., Beckett J. R., Ishii H. A., Aléon-Toppani A., Burnett D. S., Teslich N., Dai Z. R.,
1787 and Bradley J. P. (2009) The formation of boundary clinopyroxenes and associated glass
1788 veins in type B1 CAIs. *Meteorit.Planet. Sci.* **44**, 665-687.
1789 Paque J. M., Sutton S. R., Simon S. B., Beckett J. R., Burnett D. S., Grossman L., Yurimoto
1790 H., Itoh S. and Connolly, H. C. Jr. (2013) XANES and Mg isotopic analyses of spinels in
1791 Ca-Al-rich inclusions: Evidence for formation under oxidizing conditions. *Meteorit.*
1792 *Planet. Sci.* **48**, 2015-2043.
1793 Park C., Wakaki S., Sakamoto N., Kobayashi S. and Yurimoto H. (2012) Oxygen isotopic
1794 composition of the solar nebula gas inferred from high-precision isotope imaging of
1795 melilite crystals in an Allende CAI. *Meteorit. Planet. Sci.* **47**, 2070-2083.
1796 Park C., Nagashima K., Wasserburg G. J., Papanastassiou D. A., Hutcheon I. D., Davis A. M.,
1797 Huss G. R., Bizarro M. and Krot A. N. (2014) Calcium and titanium isotopic compositions
1798 of FUN CAIs: Implications for their origin. *Lunar Planet. Sci. 45*, Lunar Planet. Inst.,
1799 Houston. #2656(abstr.).
1800 Park C., Nagashima K., Krot A. N., Huss G. R., Davis A. M. and Bizzarro M. (2017)
1801 Calcium-aluminum-rich inclusions with fractionation and unidentified nuclear effects
1802 (FUN CAIs): II. Heterogeneities of magnesium isotopes and ^{26}Al in the early Solar System
1803 inferred from in situ high-precision magnesium-isotope measurements. *Geochim.*
1804 *Cosmochim. Acta* **201**, 6-24.

1805 Richter F. M. (2004) Timescales determining the degree of kinetic isotope fractionation by
1806 evaporation and condensation. *Geochim. Cosmochim. Acta* **68**, 4971-4992.
1807 Richter F M., Mendybaev R. A. and Davis A. M. (2006) Conditions in the protoplanetary disk
1808 as seen by the type B CAIs. *Meteorit. Planet. Sci.* **41**, 83-93.
1809 Richter F. M., Janney P. E., Mendybaev R. A., Davis A. M. and Wadhwa M. (2007)
1810 Elemental and isotopic fractionation of type B CAI-like liquids by evaporation. *Geochim.*
1811 *Cosmochim. Acta* **71**, 5544-5564.
1812 Ruzicka A. (1997) Mineral layers around coarse-grained, Ca-Al-rich inclusions in CV3
1813 carbonaceous chondrites: Formation by high-temperature metasomatism. *J. Geophys. Res.*
1814 **102**, 13387-13402.
1815 Ryerson F. J. and McKeegan K. D. (1994) Determination of oxygen self-diffusion in
1816 akermanite, anorthite, diopside, and spinel: Implications for oxygen isotopic anomalies and
1817 the thermal histories of Ca-Al-rich inclusions. *Geochim. Cosmochim. Acta* **58**, 3713-3734.
1818 Sahijpal S., Goswami J. N. and Davis A. M. (2000) K, Mg, Ti, and Ca isotopic compositions
1819 and refractory trace element abundances in hibonites from CM and CV meteorites:
1820 Implications for early solar system processes. *Geochim. Cosmochim. Acta* **64**, 1989-2005.
1821 Sakaguchi I. and Haneda H. (1996) Oxygen tracer diffusion in single-crystal $CaTiO_3$. *J. Solid*
1822 *Sate Chem.* **124**, 195-197.
1823 Schairer J. F. and Yoder, Jr., H. S. (1969) Critical planes and flow sheet for a portion of the
1824 system CaO-MgO-Al_2O_3-SiO_2 having petrological applications. *Carnegie Inst. Wash.*
1825 *Yearb.* **68**, 202-214.
1826 Shahar A. and Young E. D. (2007) Astrophysics of CAI formation as revealed by silicon
1827 isotope LA-MC-ICPMS of an igneous CAI. *Earth Planet. Sci. Lett.* **257**, 497-510.

1828 Sheng Y. J., Wasserburg G. J. and Hutcheon I. D. (1992) Self-diffusion of magnesium in
1829 spinel and in equilibrium melts: constraints on flash heating of silicates. *Geochim.*
1830 *Cosmochim. Acta* **56**, 2535-2546.
1831 Shu F. H., Shang H., Glassgold A. E. and T. Lee (1997) X-rays and fluctuating X-winds from
1832 protostars. *Science* **277**, 1475-1479.
1833 Simon J. I. and DePaolo D. J. (2010) Stable calcium isotopic composition of meteorites and
1834 rocky planets. *Earth Planet. Sci. Lett.* **289**, 457-466.
1835 Simon J. I. and Young E. D. (2011) Resetting, errorchrons and the meaning of canonical CAI
1836 initial ^{26}Al/ ^{27}Al values. *Earth Planet. Sci. Lett.* **304**, 468-482.
1837 Simon J. I., Young E. D., Russell S. S., Tonui E. K., Dyl K. A. and Manning C. E. (2005) A
1838 short timescale for changing oxygen fugacity in the solar nebula revealed by high-
1839 resolution ^{26}Al-^{26}Mg dating of CAI rims. *Earth Planet. Sci. Lett.* **238**, 272-283.
1840 Simon J. I., Hutcheon I. D., Simon S. B., Matzel J. E. P., Ramon E. C., Weber P. K.,
1841 Grossman L. and DePaolo D. J. (2011) Oxygen isotope variations at the margin of a CAI
1842 records circulation within the solar nebula. *Science* **331**, 1175-1178.
1843 Simon J. I., Matzel J. E. P., Simon S. B., Hutcheon I. D., Ross D. K., Weber P. K. and
1844 Grossman L. (2016) Oxygen isotopic variations in the outer margins and Wark-Lovering
1845 rims of refractory inclusions. *Geochim. Cosmochim. Acta* **186**, 242-276.
1846 Simon J. I., Jordan M. K., Tappa M. J., Schauble E. A., Kohl I. E. and Young E. D. (2017)
1847 Calcium and titanium isotope fractionation in refractory inclusions: tracers of condensation
1848 and inheritance in the early solar protoplanetary disk. *Earth Planet. Sci. Lett.* **472**, 277-288.
1849 Simon S. B. and Grossman L. (2004) A preferred method for the determination of bulk
1850 compositions of coarse-grained refractory inclusions and some implications of the results.
1851 *Geochim. Cosmochim. Acta* **68**, 4237-4248.

1852 Simon S. B., Davis A. M. and Grossman L. (1996) A unique ultrarefractory inclusion from
1853 the Murchison meteorite. *Meteorit. Planet. Sci.* **31**, 106-115.
1854 Simon S. B., Davis A. M., Grossman L. and McKeegan K. D. (2002) A hibonite-corundum
1855 inclusion from Murchison: A first-generation condensate from the solar nebula. *Meteorit.*
1856 *Planet. Sci.* **37**, 533-548.
1857 Simon S. B., Sutton S. R. and Grossman L. (2007) Valence of titanium and vanadium in
1858 pyroxene in refractory inclusion interiors and rims. *Geochim. Cosmochim. Acta* **71**, 3098-
1859 3118.
1860 Stolper E. (1982) Crystallization sequences of Ca-Al-rich inclusions from Allende: An
1861 experimental study. *Geochim. Cosmochim. Acta* **46**, 2159-2180.
1862 Taillifet E., Baillié K., Charnoz S. and Aléon J. (2014) Origin of refractory inclusion diversity
1863 by turbulent transport in the inner solar nebula. *Lunar Planet. Sci. 45*, Lunar Planet. Inst.,
1864 Houston. #2086(abstr.).
1865 Taylor D. J., McKeegan K. D. and Krot A. N. (2004) ^{26}Al in Efremovka CAI E44L -
1866 Resolved time interval between interior and rim formation in a highly fractionated compact
1867 type A CAI. *Workshop on Chondrites and Protoplanetary disk*. Lunar Planet. Inst.,
1868 Houston. #9088(abstr.).
1869 Taylor D. J., Cosarinsky M., Liu M.-C., McKeegan K. D., Krot A. N. and Hutcheon I. D.
1870 (2005a) Survey of initial ^{26}Al in type A and B CAIs: evidence for an extended formation
1871 period for refractory inclusions. *Meteorit. Planet. Sci.* **40**: suppl., A151.
1872 Taylor D. J., McKeegan K. D. and Krot A. N. (2005b) High resolution ^{26}Al chronology :
1873 resolved time interval between rim and interior of a highly fractionated compact type A
1874 CAI from Efremovka. *Lunar Planet. Sci. 36*, Lunar Planet. Inst., Houston. #2121(abstr.).

1875 Thrane K., Nagashima K., Krot A. N. and Bizzarro M. (2008) Discovery of a new FUN CAI
1876 from a CV carbonaceous chondrite: Evidence for multistage thermal processing in the
1877 protoplanetary disk. *Astrophys J. Lett.* **680**, L141.
1878 Toppani A., Paque J. M., Burnett D. S., Teslich N., Moberlychan W., Dai Z. R. and Bradley J.
1879 P. (2006) Wark-Lovering rims at the nanometer scale: a transmission electron microscopy
1880 study. *Lunar Planet. Sci. 37*, Lunar Planet. Inst., Houston. #2030(abstr.).
1881 Ushikubo T., Tenner T. J., Hiyagon H. and Kita N. T. (2017) A long duration of the ^{16}O-rich
1882 reservoir in the solar nebula, as recorded in fine-grained refractory inclusions from the
1883 least metamorphosed carbonaceous chondrites. *Geochim. Cosmochim. Acta* **201**, 103-122.
1884 Wark D. and Boynton W. V. (2001) The formation of rims on calcium-aluminum-rich
1885 inclusions: Step I - Flash heating. *Meteorit. Planet. Sci.* **36**, 1135-1166.
1886 Wark D. A. and Lovering J. F. (1977) Marker events in the early evolution of the solar
1887 system: evidence from rims on Ca-Al-rich inclusions in carbonaceous chondrites, *Proc.*
1888 *Lunar Sci. Conf. 8th*, 95-112.Yang H.-Y., Salmon J. F., and Foster W. R. (1972) Phase
1889 equilibria of the join akermanite-anorthite-forsterite in the system CaO-MgO-Al_2O_3-SiO_2
1890 at atmospheric pressure. *Amer. J. Sci.* **272**, 161-188.
1891 Yang L. and Ciesla F. J. (2012) The effects of disk building on the distributions of refractory
1892 materials in the solar nebula. *Meteorit. Planet. Sci.* **47**, 99-119.
1893 Yoshitake M., Koide Y. and Yurimoto H. (2005) Correlations between oxygen-isotopic
1894 composition and petrologic setting in a coarse-grained Ca, Al-rich inclusion. *Geochim.*
1895 *Cosmochim. Acta* **69**, 2663-2674.
1896 Young E. D. (2007) Time-dependent oxygen isotopic effects of CO self shielding across the
1897 solar protoplanetary disk. *Earth Planet. Sci. Lett.* **262**, 468-483.

1898 Young E. D., Simon J. I., Galy A., Russell S. S., Tonui E. and Lovera O. (2005) Supra-
1899 canonical $^{26}Al/^{27}Al$ and the residence time of CAIs in the solar protoplanetary disk.
1900 *Science* **308**, 223-227.
1901 Yu Y., Hewins R. H., Clayton, R. N. and Mayeda T. K. (1995) Experimental study of high
1902 temperature oxygen isotope exchange during chondrule formation. *Geochim.*
1903 *Cosmochim. Acta* **59**, 2095-2104.
1904 Yurimoto H. and Kuramoto K. (2004) Molecular cloud origin for the oxygen isotope
1905 heterogeneity in the Solar System. *Science* **305**, 1763-1766.
1906 Yurimoto H., Ito M. and Nagasawa H. (1998) Oxygen isotope exchange between refractory
1907 inclusion in Allende and solar nebula gas. *Science* **282**, 1874-1877.Zhang X., Ganguly J.
1908 and Ito M. (2010) Ca–Mg diffusion in diopside: tracer and chemical inter-diffusion
1909 coefficients. *Contrib. Mineral. Petrol.* **159**, 175–186.
1910
1911

Figure captions

Fig. 1. Backscattered electron (BSE) images of CAI Efremovka 101.1. a) Regions of interest. b) Ion probe analysis spots.

Fig. 2. Mg Kα X-ray map of the upper portion of E101.1 in log scale. Spinel clusters are connected to the rim of the CAI by trails of spinel grains surrounded by gehlenitic melilite (dark). Black grains are devoid of Mg (perovskite, metal, anorthite, nepheline...). Abbreviations: sp - spinel, sin px - sinuous pyroxene, mel - melilite, fo - forsterite, mtx - matrix.

Fig. 3. Example of spinels (sp) with clinopyroxene (cpx) rims and reaction textures. (A) BSE image of cluster of anhedral spinel, embayed and rimmed by cpx. (B) BSE image of anhedral spinel grains almost completely enclosed in the cpx + sp rim symplectite detailed in D and E. (C) Cluster 3 dominated by subhedral spinels also contains grains with local embayments, anhedral shapes, and cpx ± sp rim. BSE image, dotted ellipse indicates ion probe spot for Mg isotope analysis Mg3. (D) False color RGB TiAlMg map illustrating the distribution of the Ti-bearing cpx rim (red) with spinel μm and sub-μm inclusions around coarser spinel (light blue) in (B). (E) Detail of the cpx + sp rim around spinel in (B) and (D), BSE image. (F) Detail of the perovskite-containing cpx rim around spinel from cluster 2. Dashed white lines in (A), (C) and (E) and arrows in (E) and (F) indicate the border of the cpx ± sp rim.

Fig. 4. BSE images of perovskite-metal (pv-met) nodules rimmed by the Sc-Zr-rich pyroxene. (A) nodule with silicate melt inclusions within metal. (B) V-Ti oxide in pv-met association. (C) perovskite Per B. (D) Detail of top metal grain in C, showing metamorphic exsolution of

1937 silica, phosphate and V-Fe-oxide. Sc-Zr-rich pyroxene shown with dotted lines. Dotted
1938 ellipses indicate O isotope SIMS spots. Abbreviations: met - metal, pv - perovskite, cpx -
1939 pyroxene, mel - melilite, neph - nepheline, an - anorthite, phosph - phosphate, sil - silica.
1940
1941 **Fig. 5**. O isotopic compositions in E101.1. (A) all data. (B) sinuous pyroxene and associated
1942 FeO-rich silicates. Shades of color indicate different degree of mixing between Al-diopside
1943 and FeO-rich minerals within SIMS spots (proportions given). n.d. stands for not determined,
1944 most likely anorthite or possibly wollastonite. (C) minerals in the accretionary rim (AR) and
1945 Wark-Lovering rim (WLR). (D) relatively ^{16}O-poor minerals in E101.1; dash-dotted line is a
1946 mass fractionation line through the most ^{16}O-poor data. TFL - terrestrial mass fractionation
1947 line, CCAM - Carbonaceous Chondrites Anhydrous Minerals mixing line.
1948
1949 **Fig. 6**. Oxygen isotopic compositions of melilite in E101.1. (a) Δ^{17}O as a function of melilite
1950 chemistry. Grey box: typical value of spinel. 2σ errors. (b) Chemical map of melilite
1951 computed from Mg and Al X-ray maps. Bright: akermanitic mel, dark: gehlenite, spinel
1952 overlaid in white. Ellipses are ion probe spots with color coded Δ^{17}O value. (c) Chemistry of
1953 melilite as a function of distance to spinel. Profile 1, 2 and WLR are reported relative to
1954 WLR. Melilite in the vicinity of spinel clusters is reported relative to spinel in the
1955 corresponding cluster.
1956
1957 **Fig. 7**. Apparent oxygen isotope mass fractionation relative to the CCAM line as a function of
1958 Δ^{17}O. All data include perovskite, olivine, nepheline, FeO-rich silicates and glass. 2σ errors.
1959
1960 **Fig. 8**. Oxygen isotopic composition of sinuous pyroxene as a function of chemistry. (a) Δ^{17}O
1961 as a function of SiO_2 content. (b) Δ^{17}O as a function of Al_2O_3 content. Error bars are 2σ.

1962

1963 **Fig. 9**. Oxygen isotopic composition of perovskite as a function of chemistry. Per E and Per B
1964 refer to grains described in El Goresy et al. (2002). The chondritic ZrO_2/Y_2O_3 ratio and that
1965 expected from crystal/liquid fractionation are shown by a red dashed line and a green bar,
1966 respectively. 2σ errors.

1967

1968 **Fig. 10**. $\delta^{26}Mg^*$ as a function of $^{27}Al/^{24}Mg$ ratio. Inset shows close-up view of low Al/Mg
1969 phases. The dashed line indicates the theoretical isochron for a canonical initial $^{26}Al/^{27}Al$ ratio
1970 and the two dotted lines show the theoretical isochrons passing through spinel with the
1971 highest initial $^{26}Al/^{27}Al$ ratio and through melilite with the lowest initial $^{26}Al/^{27}Al$ ratio. 2σ
1972 errors.

1973

1974 **Fig. 11**. Al/Mg systematics of paired spinel and melilite. (A) cluster 2. (B) subinclusion 1. (C)
1975 cluster 3. Error bars are 2σ. 2σ uncertainties on slope and intercept.

1976

1977 **Fig. 12**. $\delta^{25}Mg$ of spinel clusters and associated melilite. In subinclusion 1, only melilite data
1978 in the close vicinity of analyzed spinel are shown. 2σ errors.

1979

1980 **Fig. 13**. Chemical and isotopic profiles in melilite from the rim toward the interior. (A)
1981 melilite chemistry. (B) stable Mg isotopes. (C) inferred initial $^{26}Al/^{27}Al$. (D) stable Si
1982 isotopes. (E) ^{16}O excess. (F) O isotopic mass fractionation (deviation from the CCAM line).
1983 Black dashed line - limit of transition zone between interior and WLR along profile 1 (where
1984 melilite becomes more gehlenitic as illustrated by grey arrow), orange dashed line - limit of
1985 corresponding zone along profile 2 (melilite behavior illustrated by orange arrow). Errors on
1986 the x-axes correspond to the beam size. 2σ errors on the y-axes.

Fig. 14. Schematic description of the events taken into account to unravel E101.1 thermal history based on O, Mg and Si isotopes. The Model arrow illustrate the backwards calculations to find the precursor composition. Steps 1 to 3 are discussed in text. Endmember compositions are given in Table S4.

Fig. 15. Mixing calculation of sinuous pyroxene with host melt. (A) Mg isotopes vs O isotopes. (B) Si isotopes vs O isotopes. (C) Si isotopes vs Mg isotopes. Mixing lines between sinuous pyroxene (assumed to be diopside) and a second component having the isotopic composition of the typical host melilite are shown. Black dashed line: the second component is a refractory CMAS melt. Red lines: the second component is melilite of indicated composition. Mixing proportions are given. 2σ errors.

Fig. 16. Comparison between the E101.1 parental CMAS melt composition (diamonds) and its pre-evaporation composition (circles) with the expectation of the equilibrium condensation sequence (trajectories from Mendybaev et al., 2017) and the composition of regular type A CAIs (open squares) and B CAIs (grey triangles). Red symbols - no Mg considered to come from subsequent spinel assimilation, orange - 50% Mg considered to come from subsequent spinel assimilation, yellow - 67% Mg considered to come from subsequent spinel assimilation. Bold circles: calculated with fractionation factors from Knight et al. (2009). Thin circles: calculated with fractionation factors from Mendybaev et al. (2013).

Fig. 17. Stable Mg and Si isotopic compositions of the rims on E101.1. Orange box - range of Si and Mg isotopes of WLR pyroxene (decoupled analyses), purple band - range of Mg isotopes in WLR spinel.

2012

2013 **Fig. 18**. Comparison between Al/Mg systematics of WLR, theoretical chronology and
2014 influence of solid-state diffusion. 2σ errors on measured data (blue). Exchanged values
2015 (orange) correspond to solid state diffusion of Mg devoid of ^{26}Mg* during 6 months at 1000
2016 K. Exchanged values are indistinguishable from the isochron expected if crystallization
2017 occured 240,000 years after canonical (dash-dotted line)

2018

2019 **Fig. 19**. Main stages of E101.1 formation. (a) schematic history, precursor and captured
2020 xenoliths as characterized by O, Mg and Si isotopes. (b) BSE image of the whole CAI with
2021 captured xenolithic material outlined with dashed lines: red - sinuous pyroxene xenoliths,
2022 black - spinel clusters xenoliths, white - complex frontier region with possible interactions
2023 between sinuous pyroxene, spinel clusters and host. Scale bar 200 μm.

2024

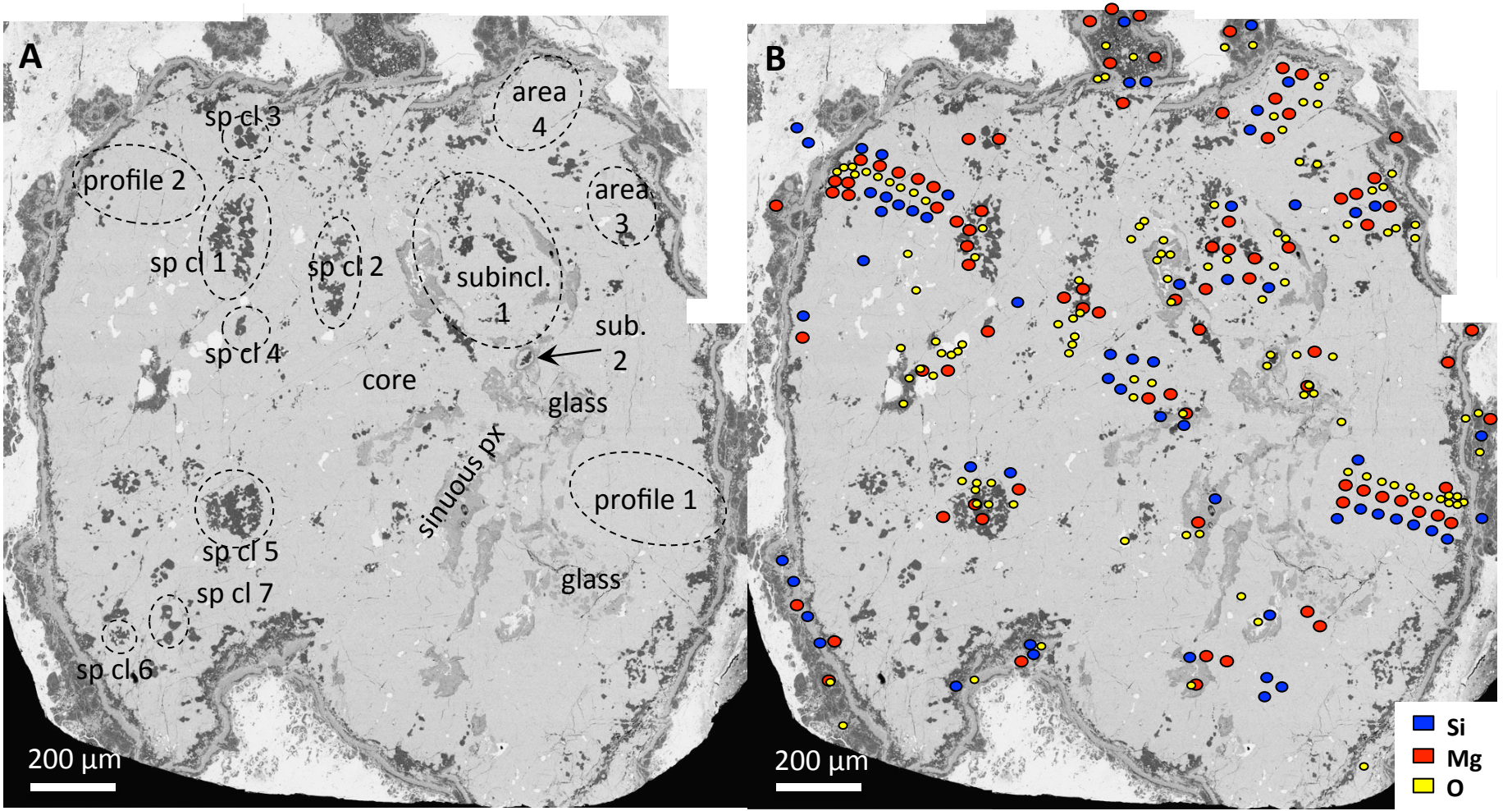
A
sp cl 3
area 4
profile 2
area 3
sp cl 1
sp cl 2
subincl. 1
sub. 2
sp cl 4
core
glass
sinuous px
profile 1
sp cl 5
glass
sp cl 7
sp cl 6
200 µm
B
200 µm
Si
Mg
O

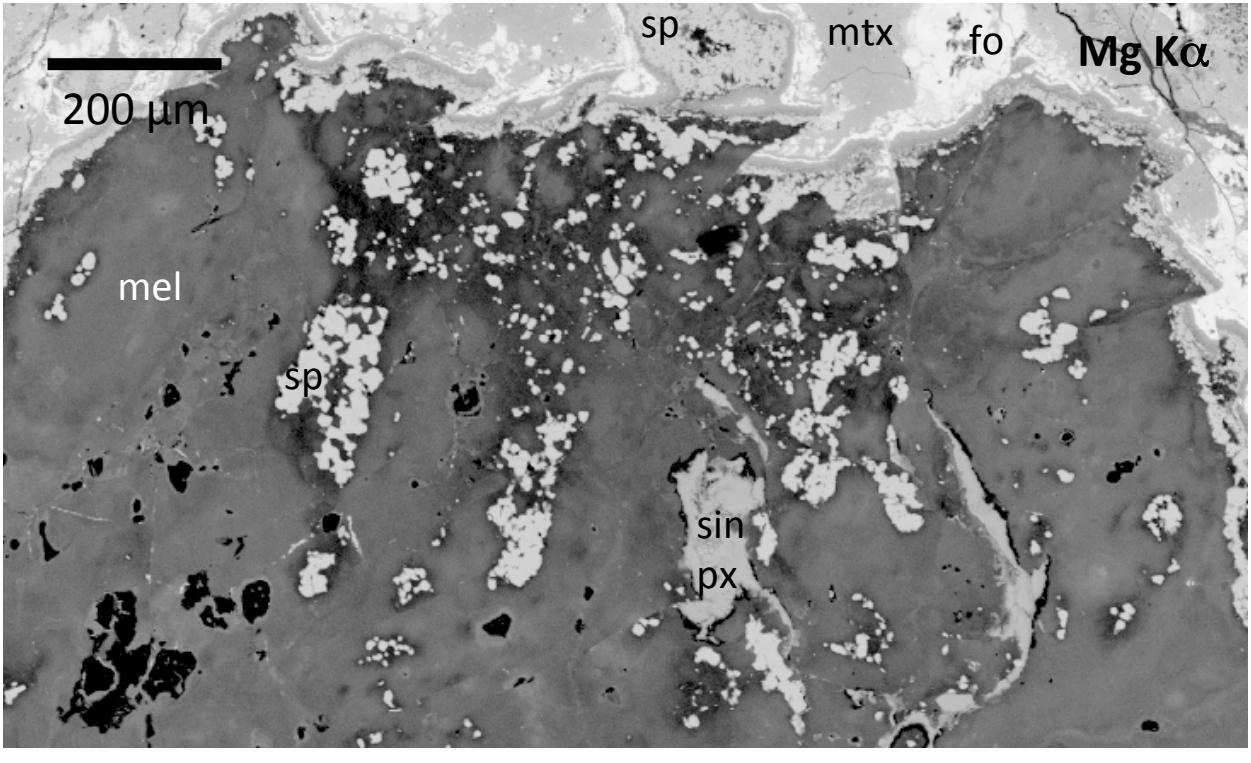
sp
mtx
fo
Mg Kα
200 µm
mel
sp
sin
px

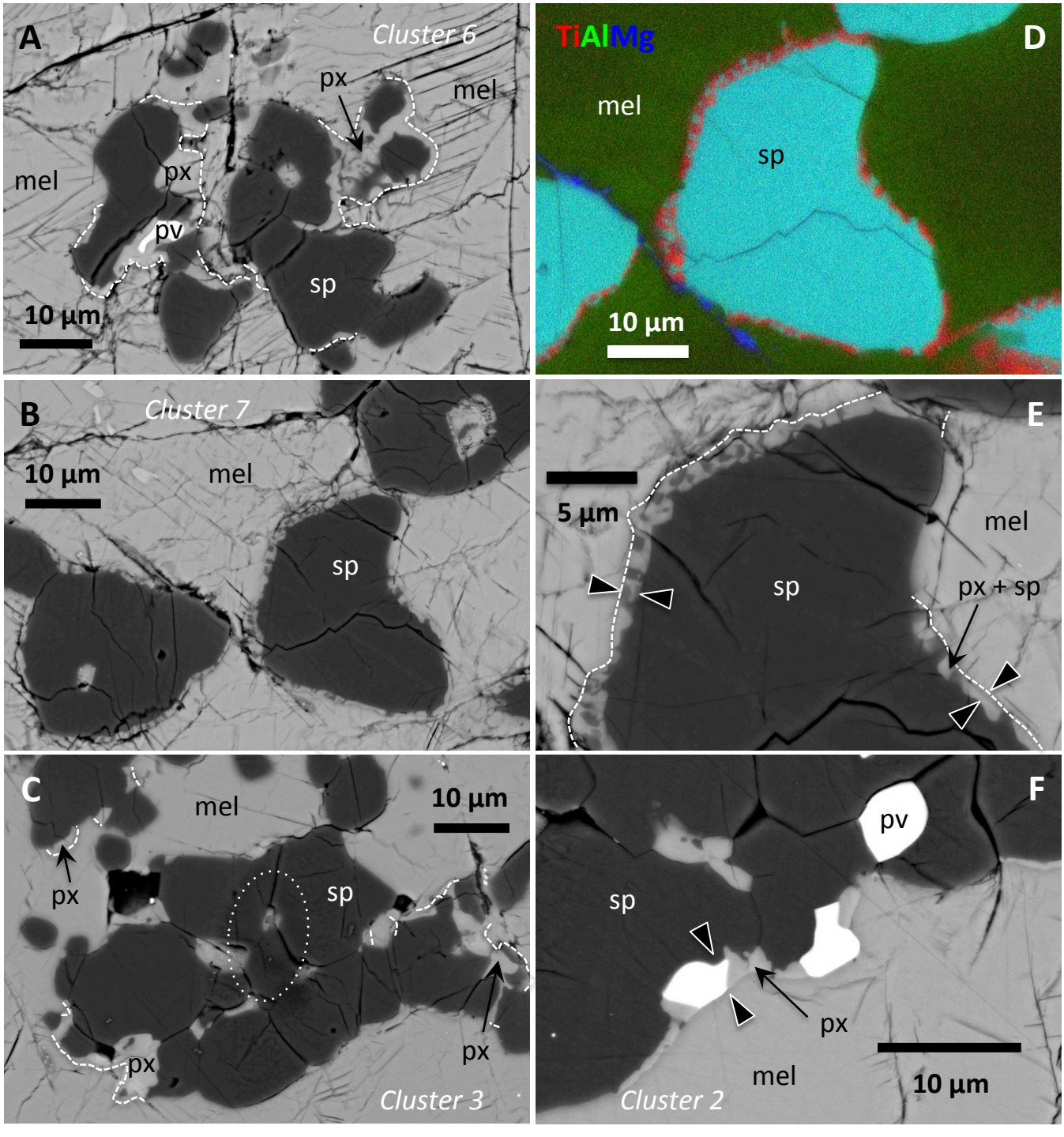
A
Cluster 6
px
mel
mel
px
pv
sp
10 µm
TiAlMg
D
mel
sp
10 µm
B
Cluster 7
10 µm
mel
sp
E
5 µm
mel
sp
px + sp
C
mel
10 µm
px
sp
px
px
Cluster 3
F
pv
sp
px
mel
10 µm
Cluster 2

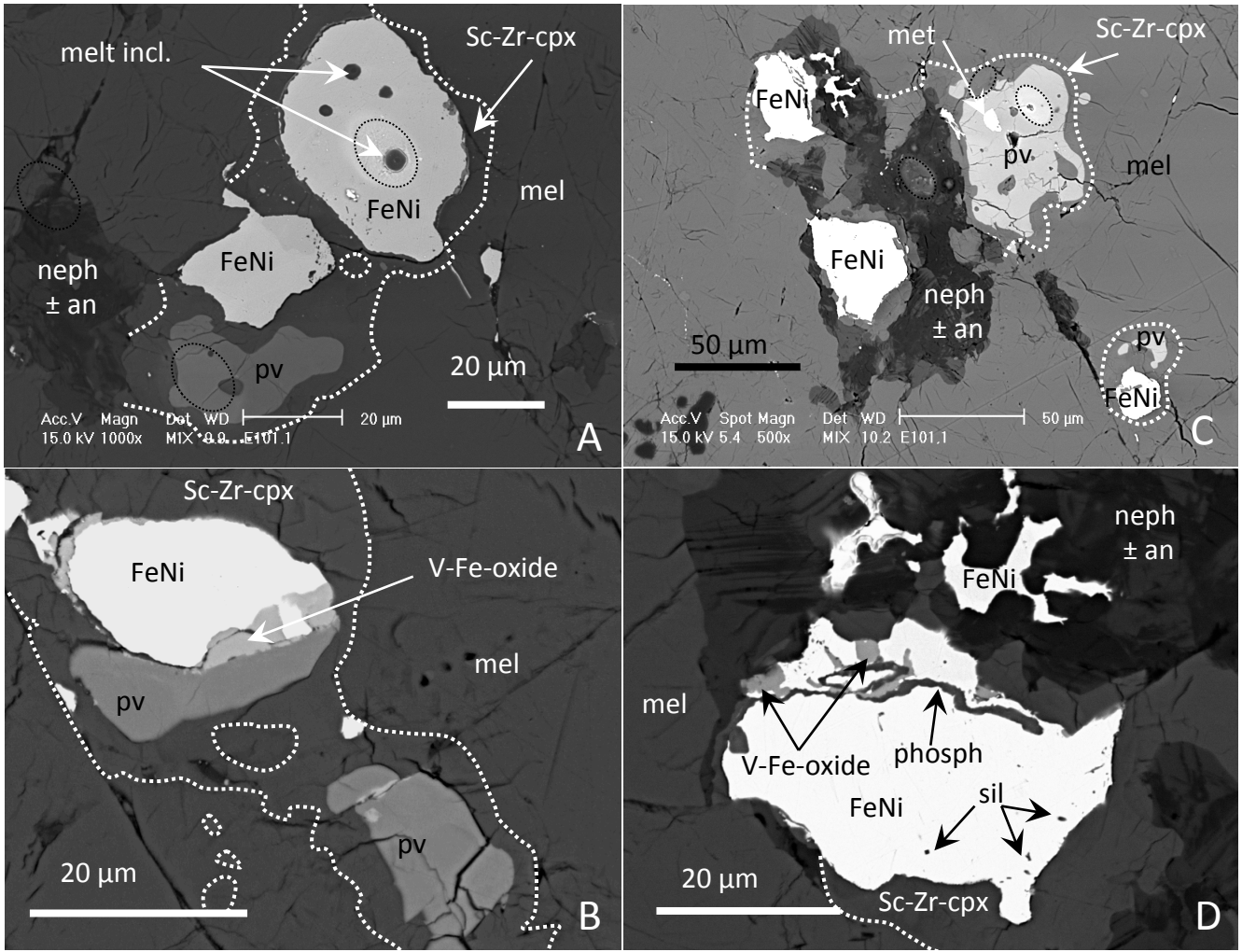
melt incl.
Sc-Zr-cpx
FeNi
mel
FeNi
neph
± an
pv
20 µm
A
Sc-Zr-cpx
FeNi
V-Fe-oxide
mel
pv
pv
20 µm
B
met
Sc-Zr-cpx
FeNi
pv
mel
FeNi
neph
± an
50 µm
pv
FeNi
C
neph
± an
FeNi
mel
V-Fe-oxide
phosph
FeNi
sil
20 µm
Sc-Zr-cpx
D

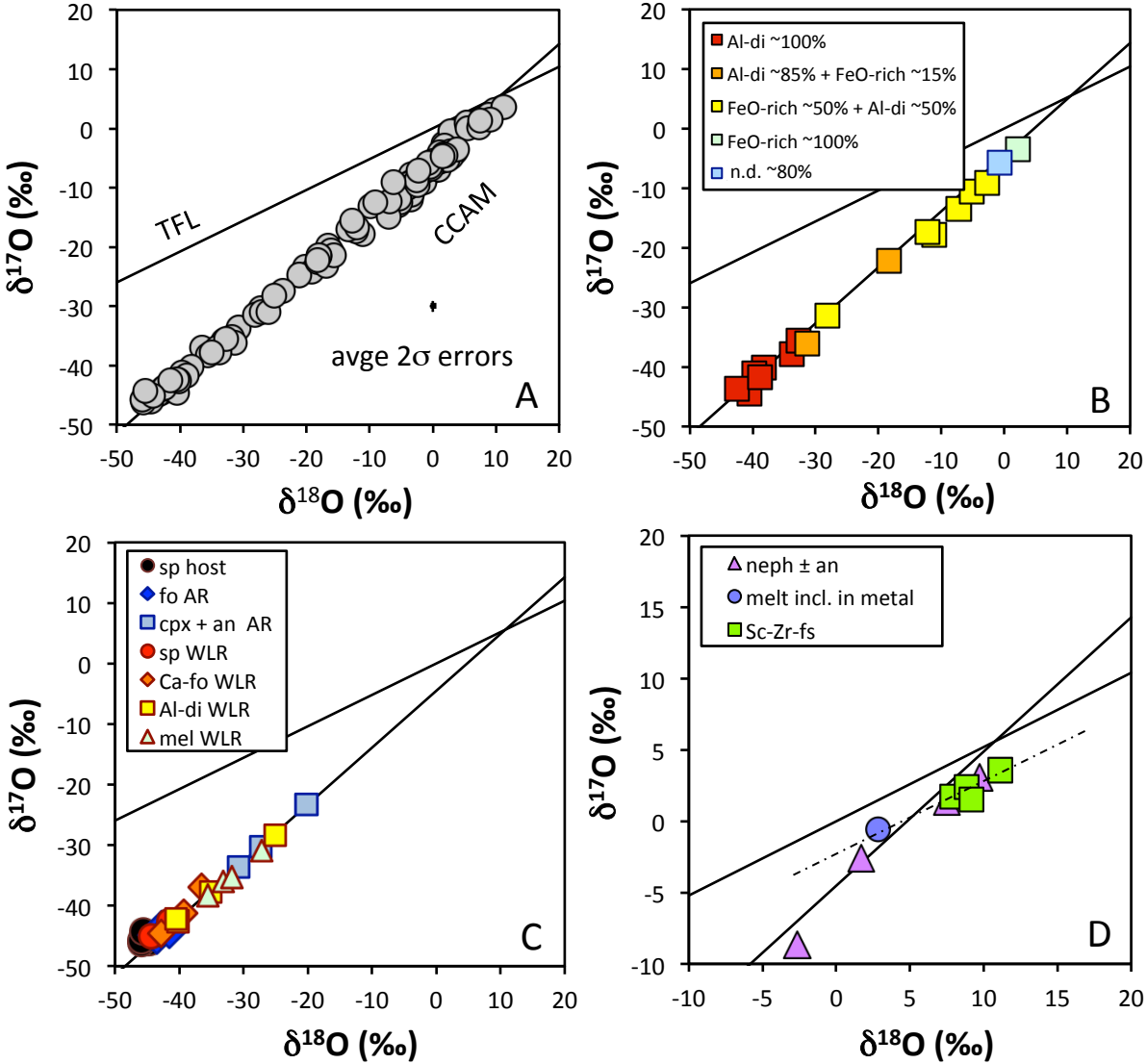
TFL
CCAM
avge 2σ errors
A
δ17O (‰)
δ18O (‰)
Al-di ~100%
Al-di ~85% + FeO-rich ~15%
FeO-rich ~50% + Al-di ~50%
FeO-rich ~100%
n.d. ~80%
B
sp host
fo AR
cpx + an AR
sp WLR
Ca-fo WLR
Al-di WLR
mel WLR
C
neph ± an
melt incl. in metal
Sc-Zr-fs
D

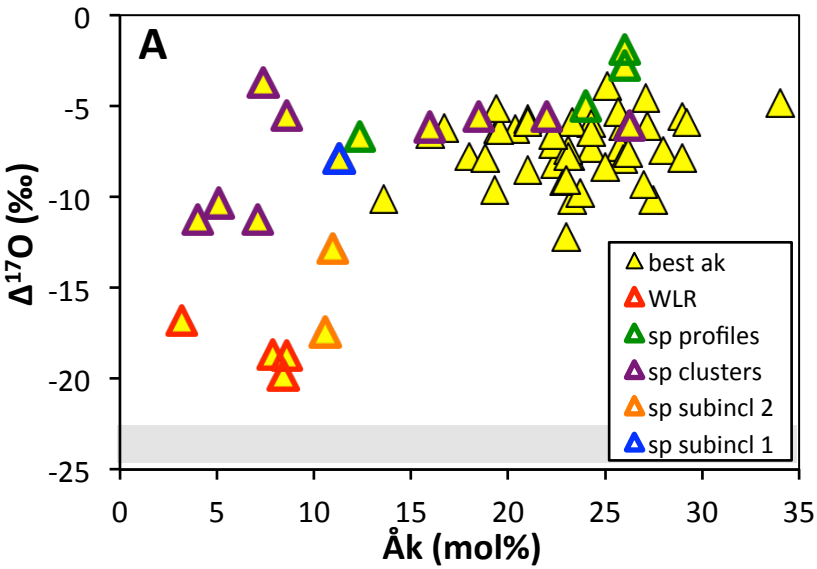
A
Δ17O (‰)
Åk (mol%)
best ak
WLR
sp profiles
sp clusters
sp subincl 2
sp subincl 1

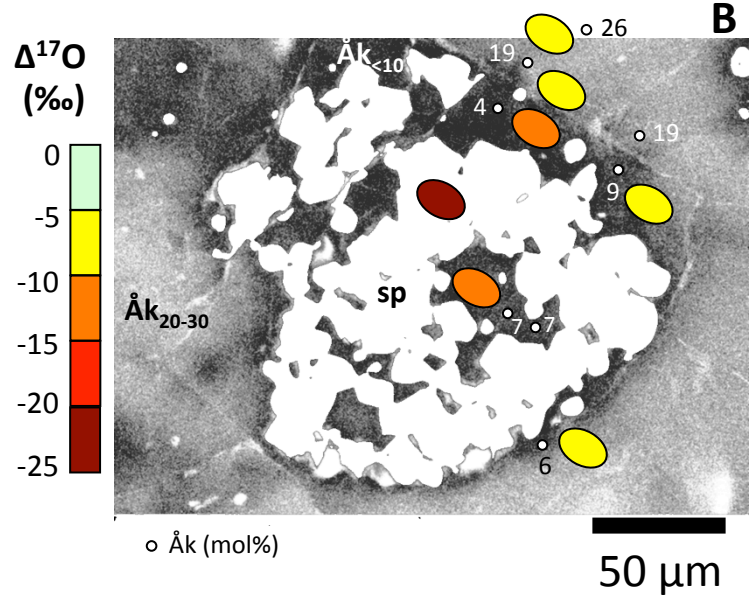
B
Δ17O (‰)
Åk<10
Åk20-30
sp
26
19
4
19
9
7
7
6
Åk (mol%)
50 µm

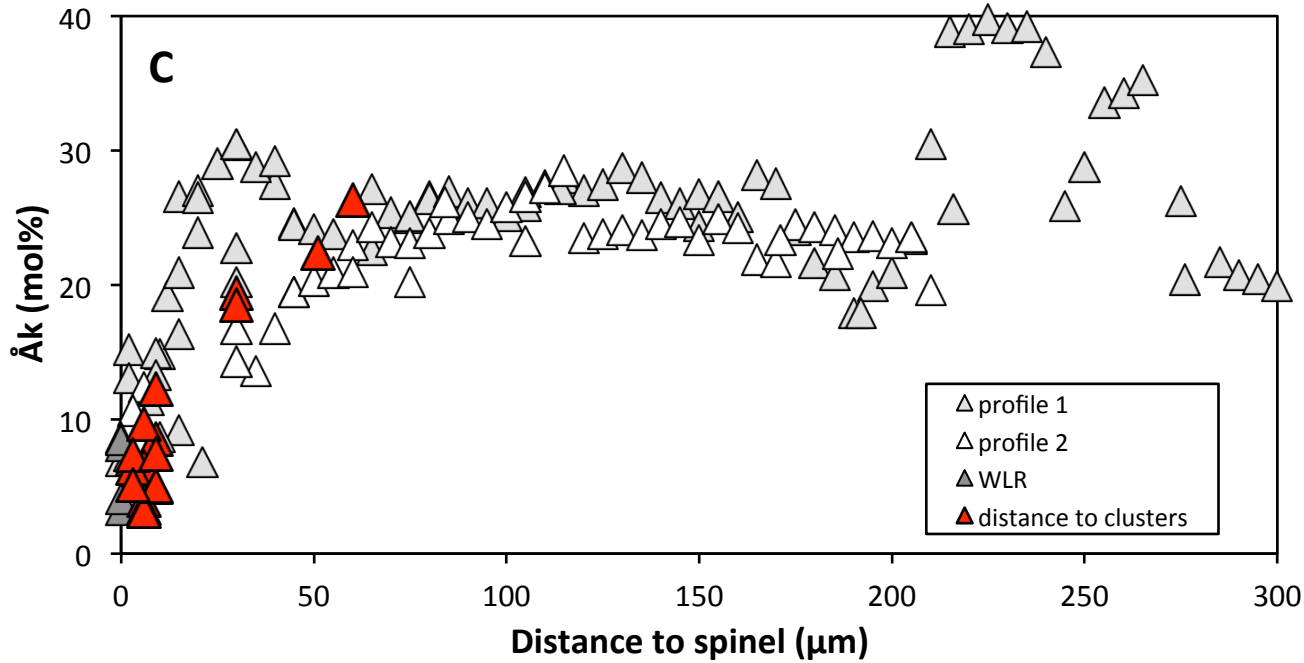
C
Åk (mol%)
Distance to spinel (µm)
profile 1
profile 2
WLR
distance to clusters

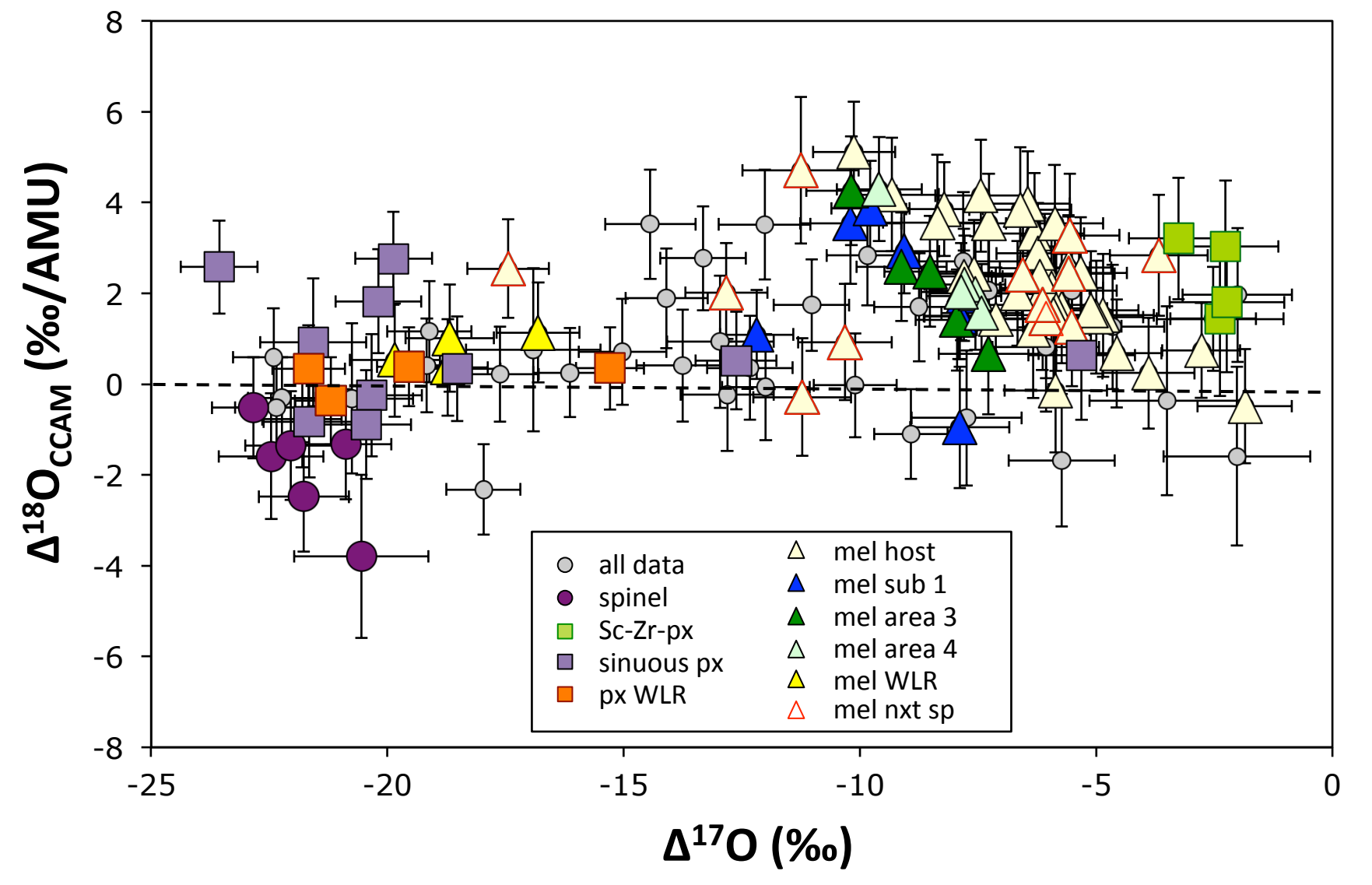
8
6
4
2
0
-2
-4
-6
-8
-25
-20
-15
-10
-5
0
Δ18OCCAM (‰/AMU)
Δ17O (‰)
all data
spinel
Sc-Zr-px
sinuous px
px WLR
mel host
mel sub 1
mel area 3
mel area 4
mel WLR
mel nxt sp

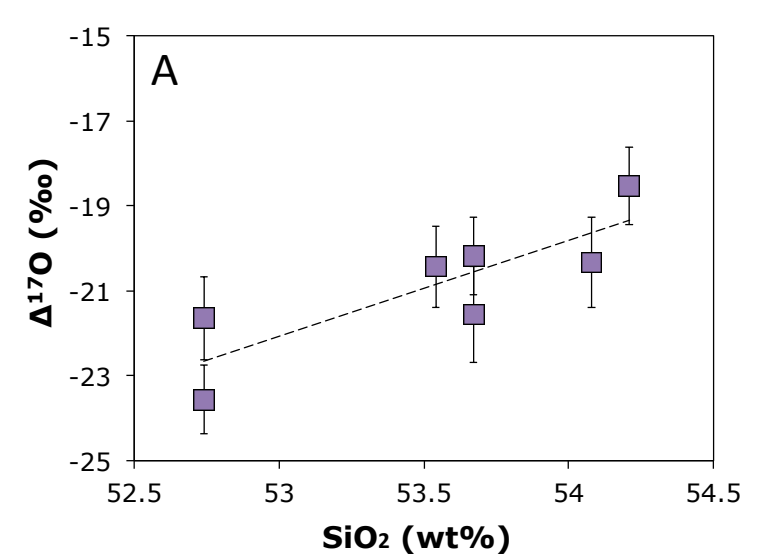
A
-15
-17
-19
-21
-23
-25
Δ17O (‰)
52.5
53
53.5
54
54.5
SiO2 (wt%)

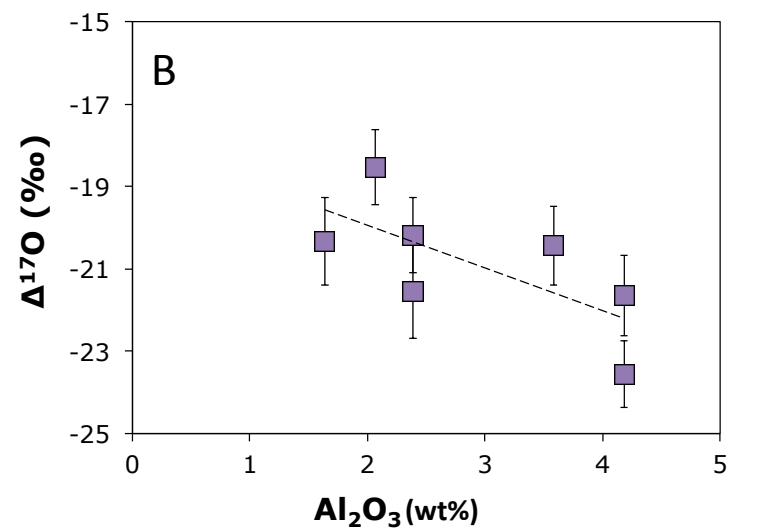
B
-15
-17
-19
-21
-23
-25
Δ17O (‰)
0
1
2
3
4
5
Al2O3 (wt%)

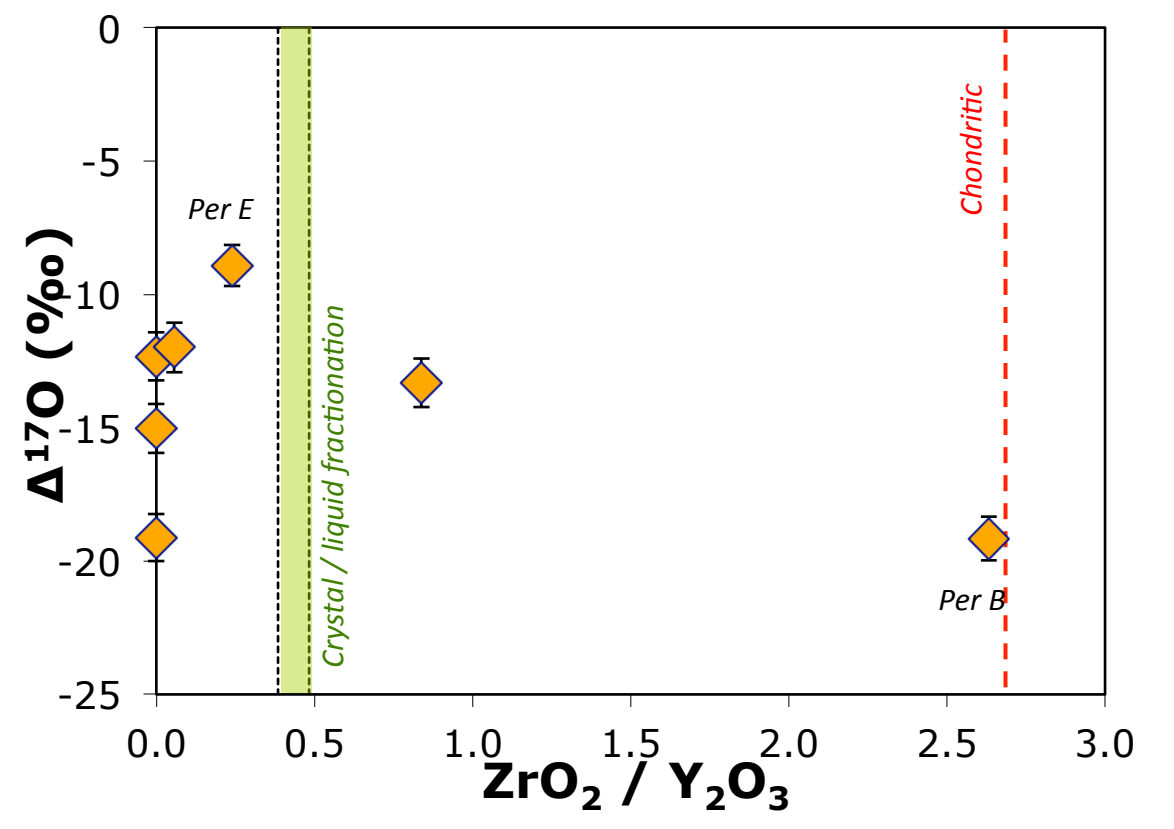
0
-5
-10
-15
-20
-25
Δ17O (‰)
0.0
0.5
1.0
1.5
2.0
2.5
3.0
ZrO2 / Y2O3
Per E
Crystal / liquid fractionation
Chondritic
Per B

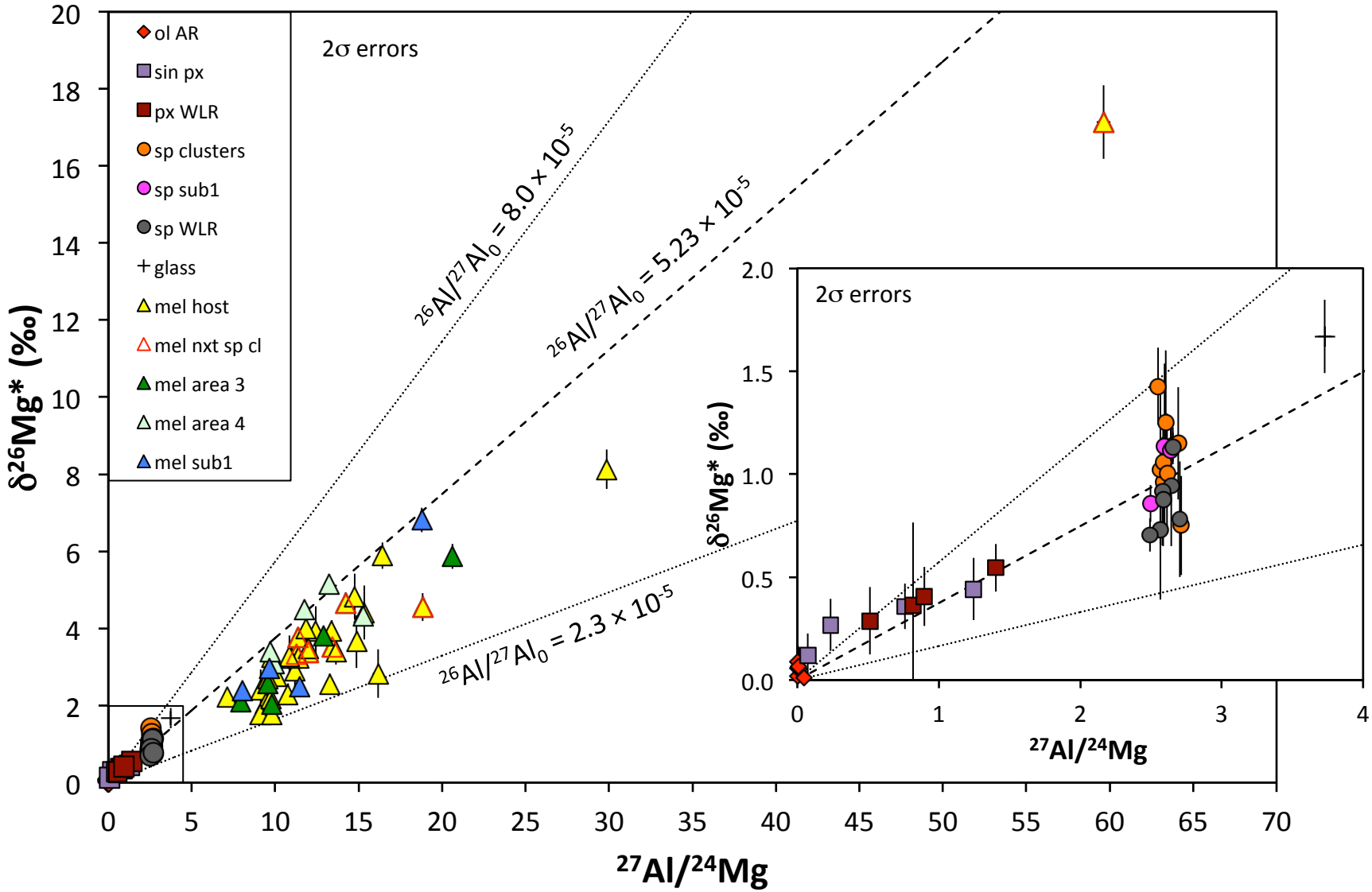
ol AR
sin px
px WLR
sp clusters
sp sub1
sp WLR
glass
mel host
mel nxt sp cl
mel area 3
mel area 4
mel sub1
2σ errors
$^{26}Al/^{27}Al_0 = 8.0 \times 10^{-5}$
$^{26}Al/^{27}Al_0 = 5.23 \times 10^{-5}$
$^{26}Al/^{27}Al_0 = 2.3 \times 10^{-5}$
$\delta^{26}Mg^*$ (‰)
$^{27}Al/^{24}Mg$
2σ errors
$\delta^{26}Mg^*$ (‰)
$^{27}Al/^{24}Mg$

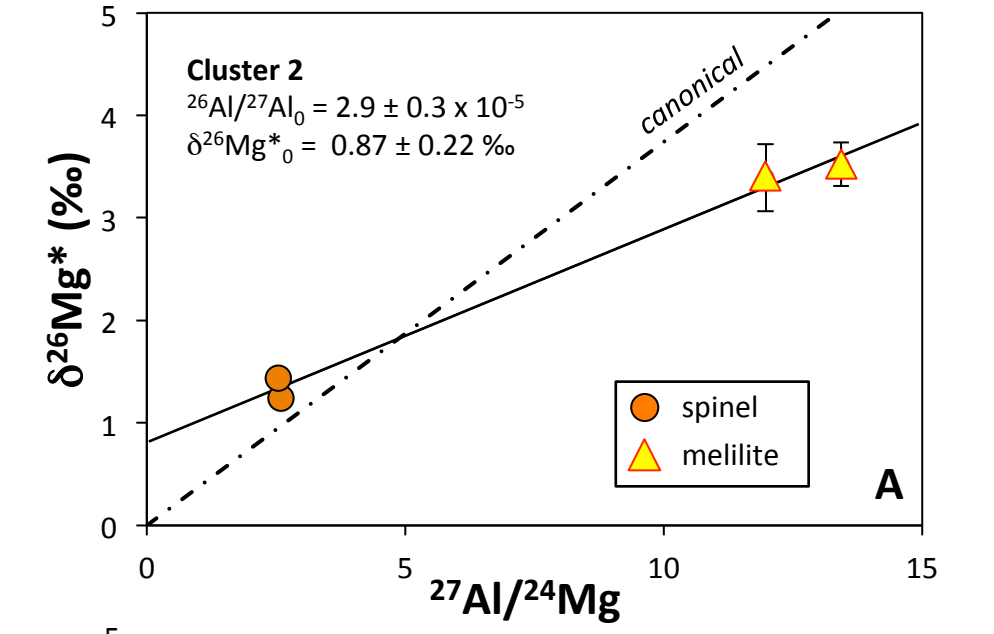
Cluster 2
$^{26}Al/^{27}Al_0 = 2.9 \pm 0.3 \times 10^{-5}$
$\delta^{26}Mg^*_0 = 0.87 \pm 0.22$ ‰
canonical
spinel
melilite
A
$\delta^{26}Mg^*$ (‰)
$^{27}Al/^{24}Mg$
0
1
2
3
4
5
0
5
10
15

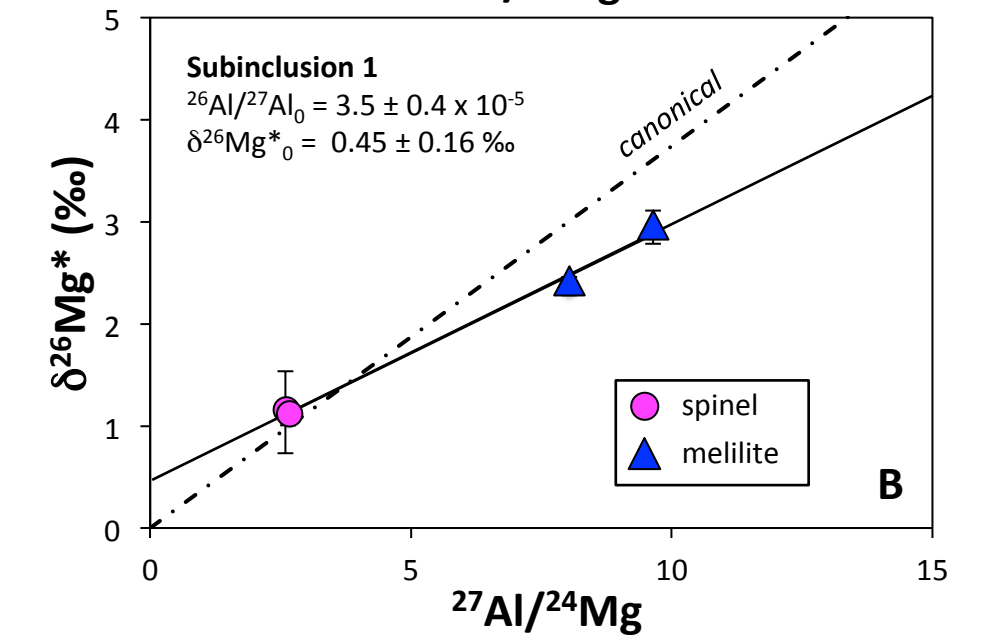
Subinclusion 1
$^{26}Al/^{27}Al_0 = 3.5 \pm 0.4 \times 10^{-5}$
$\delta^{26}Mg^*_0 = 0.45 \pm 0.16$ ‰
canonical
spinel
melilite
B
$\delta^{26}Mg^*$ (‰)
$^{27}Al/^{24}Mg$
0
1
2
3
4
5
0
5
10
15

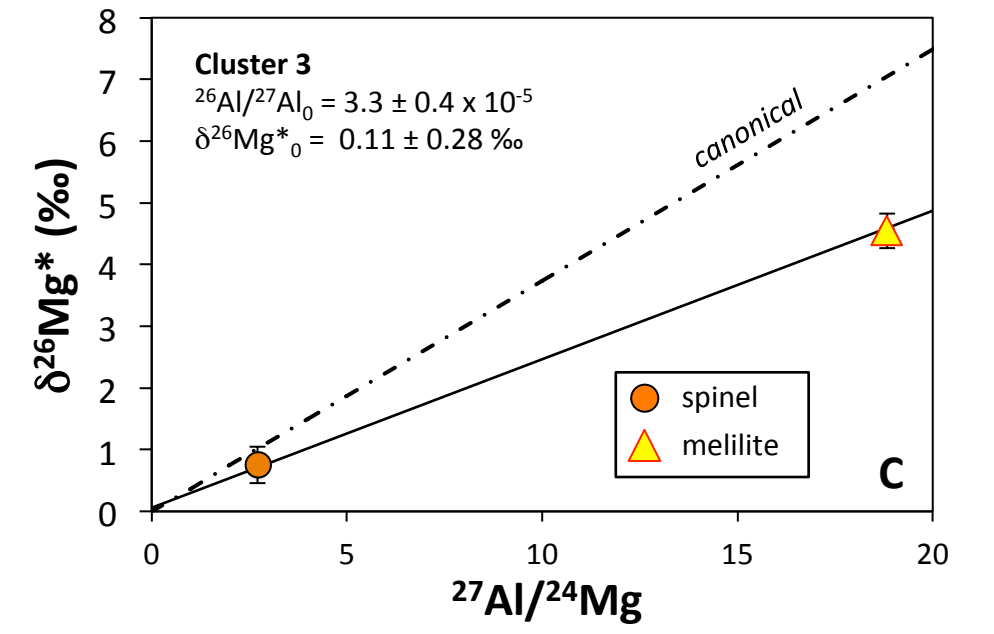
Cluster 3
$^{26}Al/^{27}Al_0 = 3.3 \pm 0.4 \times 10^{-5}$
$\delta^{26}Mg^*_0 = 0.11 \pm 0.28$ ‰
canonical
spinel
melilite
C
$\delta^{26}Mg^*$ (‰)
$^{27}Al/^{24}Mg$
0
1
2
3
4
5
6
7
8
0
5
10
15
20

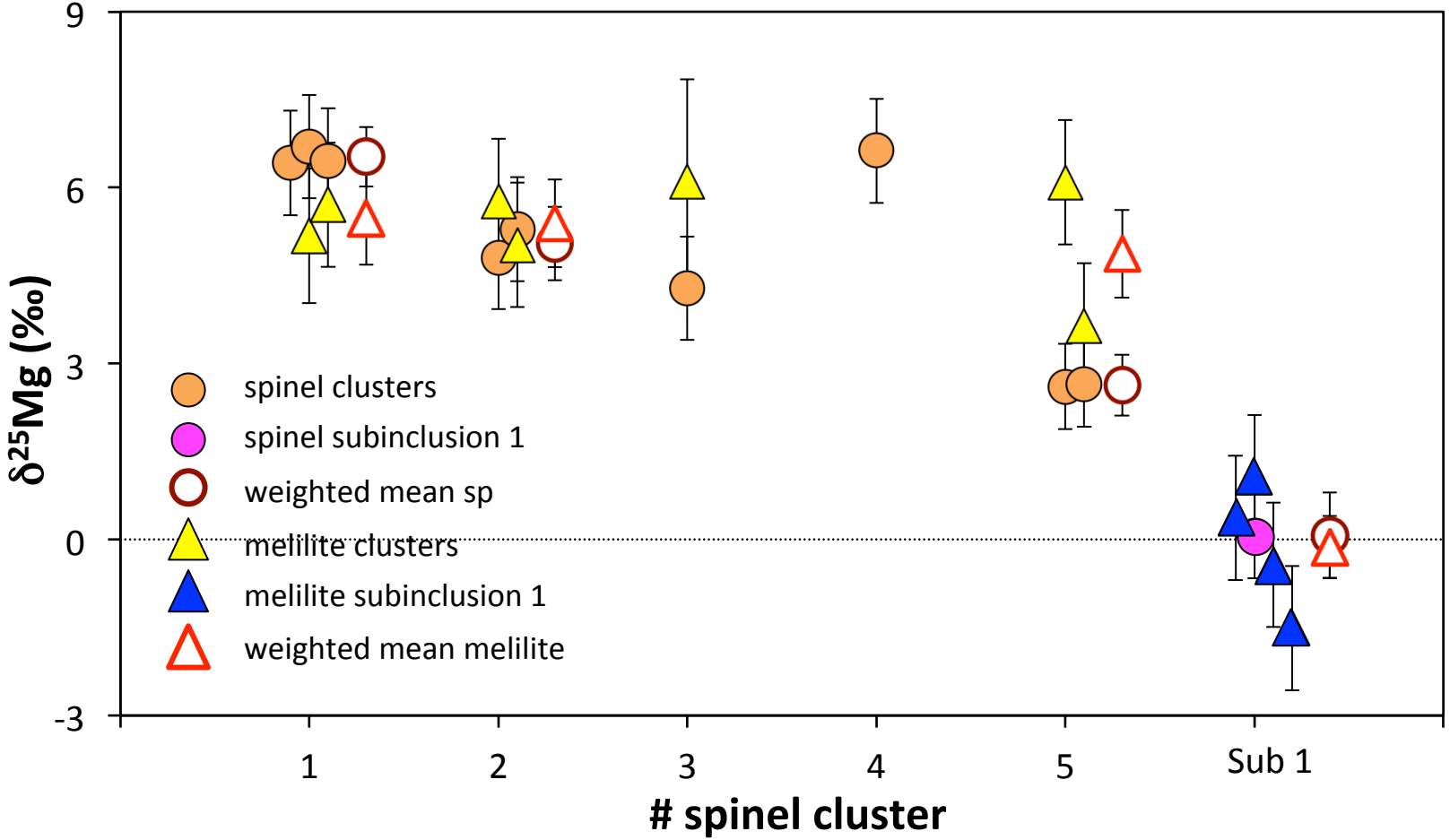
9
6
3
0
-3
δ25Mg (‰)
spinel clusters
spinel subinclusion 1
weighted mean sp
melilite clusters
melilite subinclusion 1
weighted mean melilite
1
2
3
4
5
Sub 1
spinel cluster

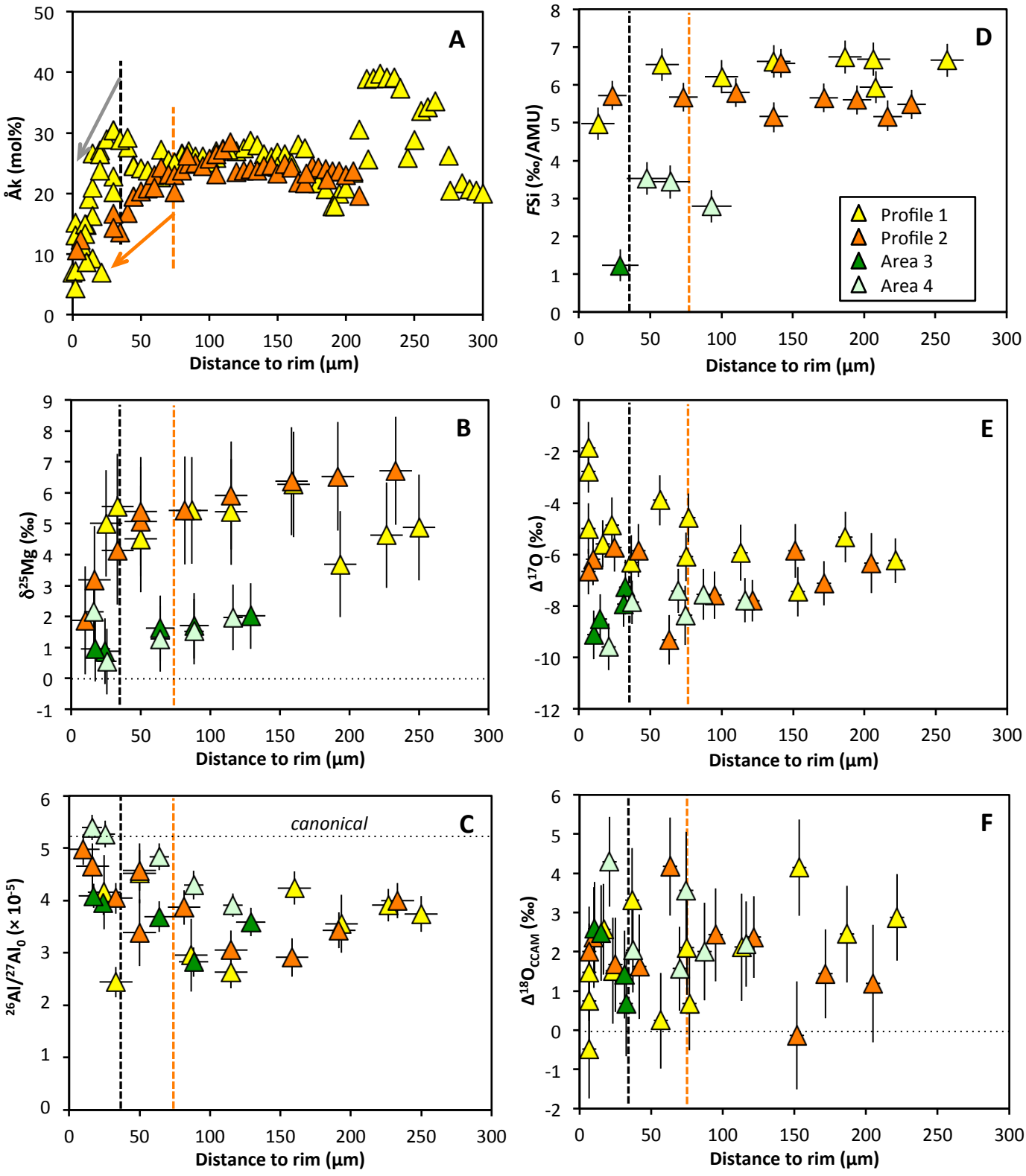
A
Åk (mol%)
Distance to rim (µm)
D
FSi (‰/AMU)
Distance to rim (µm)
Profile 1
Profile 2
Area 3
Area 4
B
δ25Mg (‰)
Distance to rim (µm)
E
Δ17O (‰)
Distance to rim (µm)
C
canonical
26Al/27Al0 (× 10-5)
Distance to rim (µm)
F
Δ18OCCAM (‰)
Distance to rim (µm)

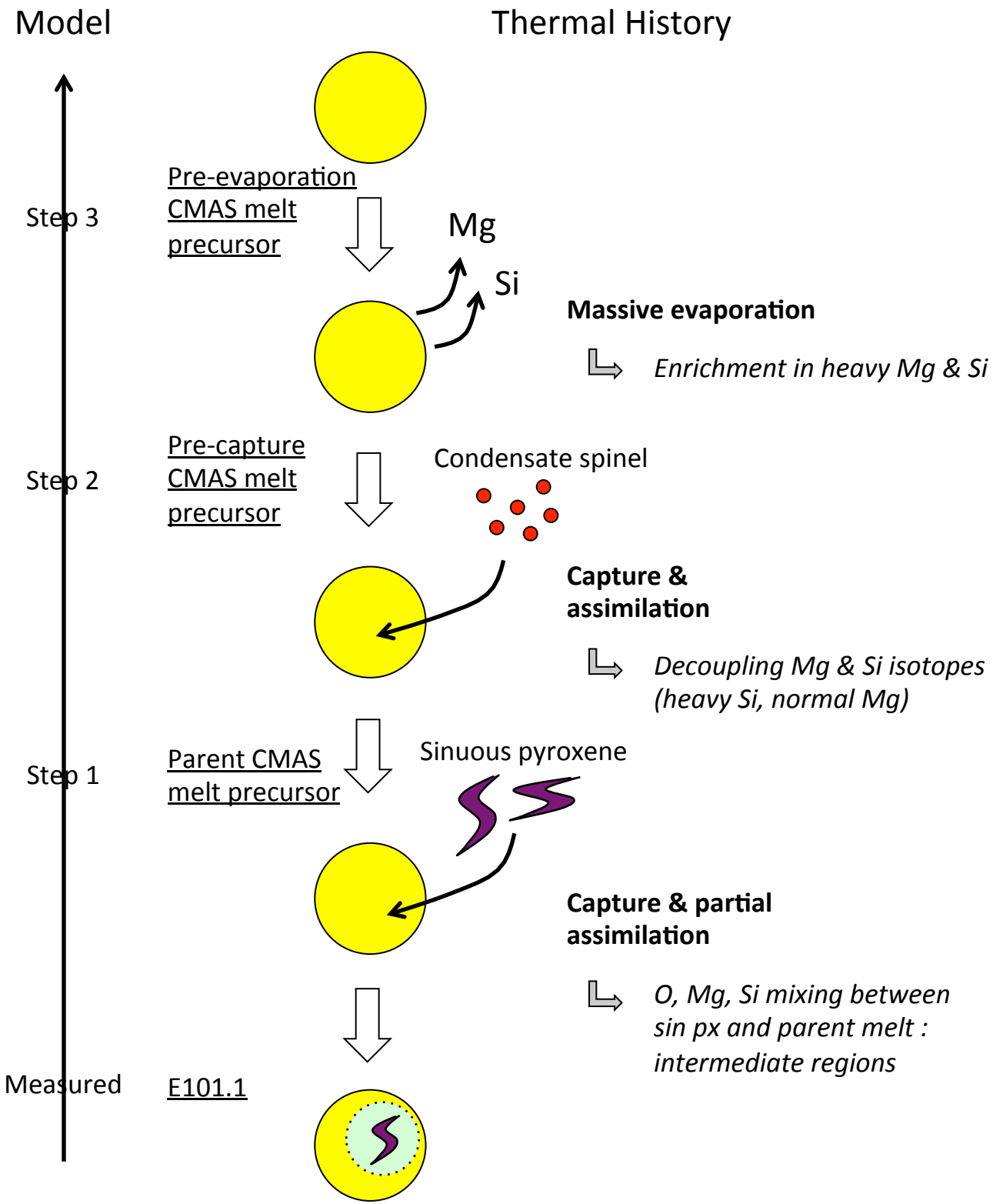
Model
Thermal History
Step 3
Step 2
Step 1
Measured
Pre-evaporation CMAS melt precursor
Mg
Si
Massive evaporation
Enrichment in heavy Mg & Si
Pre-capture CMAS melt precursor
Condensate spinel
Capture & assimilation
Decoupling Mg & Si isotopes (heavy Si, normal Mg)
Parent CMAS melt precursor
Sinuous pyroxene
Capture & partial assimilation
O, Mg, Si mixing between sin px and parent melt : intermediate regions
E101.1

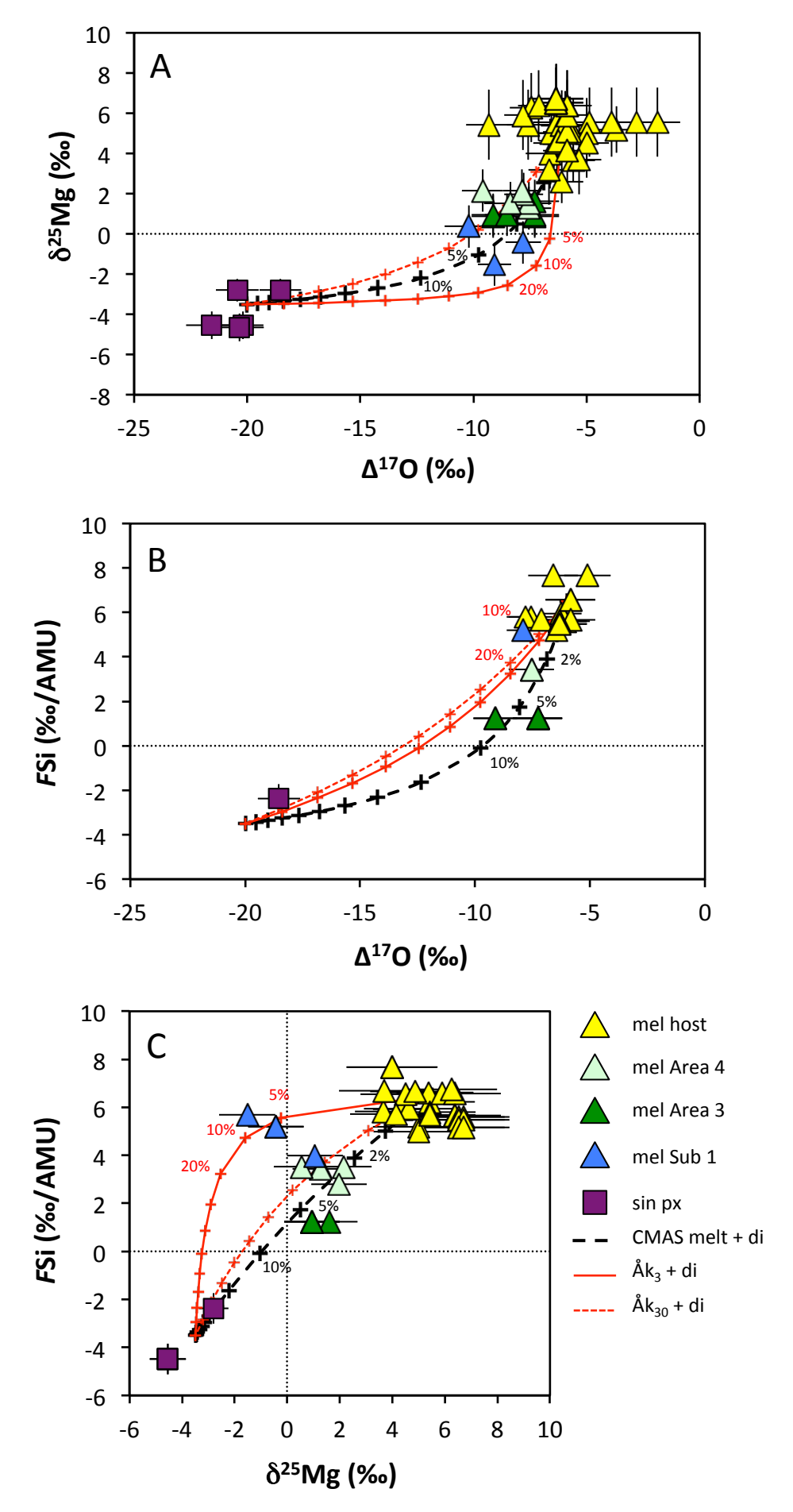
A
B
C
δ25Mg (‰)
Δ17O (‰)
FSi (‰/AMU)
5%
10%
20%
2%
mel host
mel Area 4
mel Area 3
mel Sub 1
sin px
CMAS melt + di
Åk3 + di
Åk30 + di

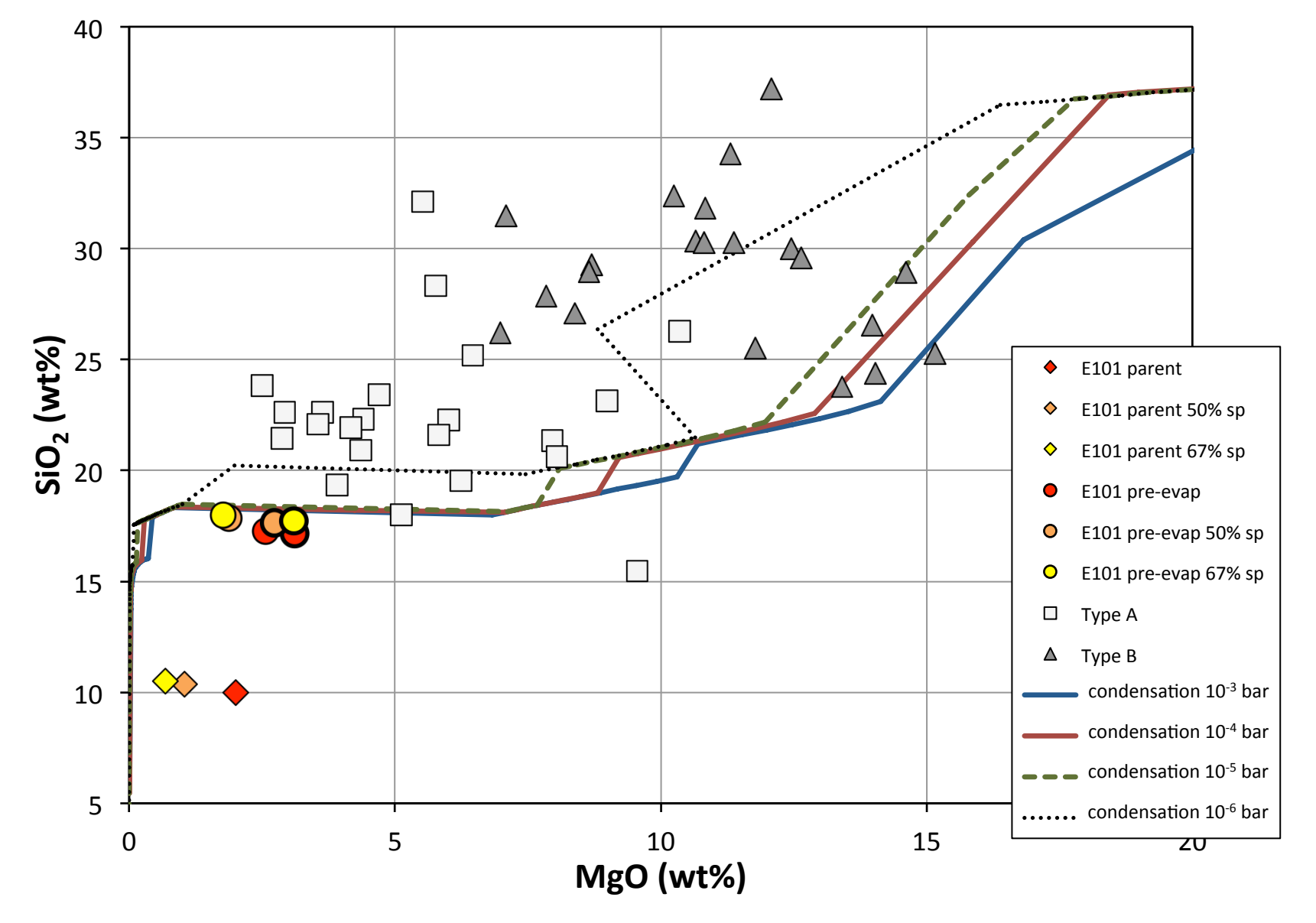
40
35
30
25
20
15
10
5
0
5
10
15
20
SiO2 (wt%)
MgO (wt%)
E101 parent
E101 parent 50% sp
E101 parent 67% sp
E101 pre-evap
E101 pre-evap 50% sp
E101 pre-evap 67% sp
Type A
Type B
condensation 10-3 bar
condensation 10-4 bar
condensation 10-5 bar
condensation 10-6 bar

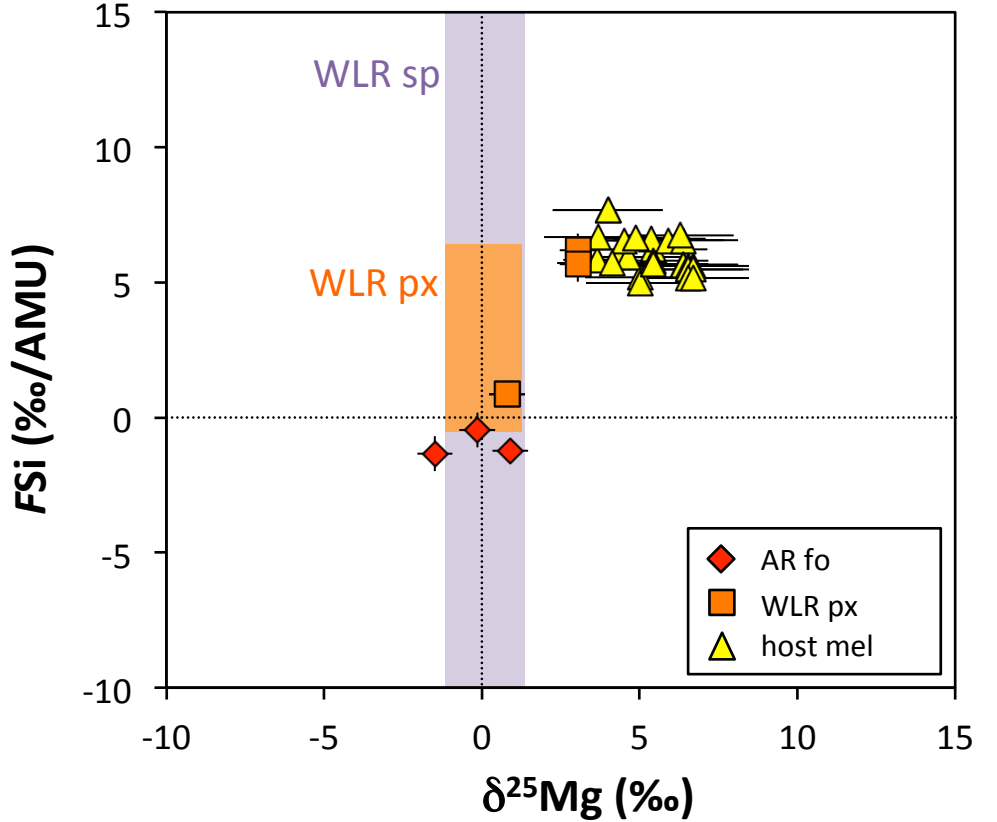
15
10
5
0
-5
-10
-10
-5
0
5
10
15
WLR sp
WLR px
FSi (‰/AMU)
δ25Mg (‰)
AR fo
WLR px
host mel

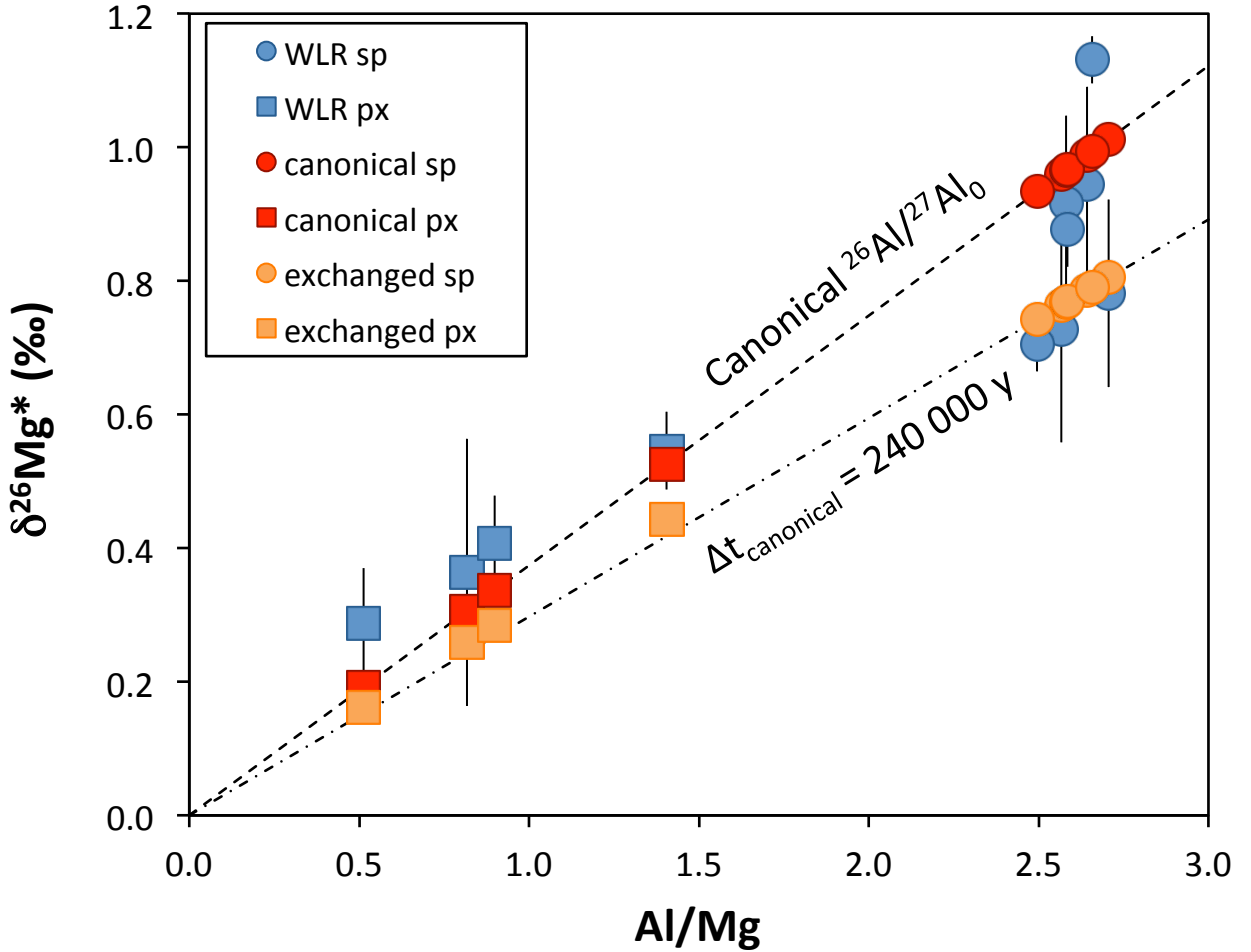
WLR sp
WLR px
canonical sp
canonical px
exchanged sp
exchanged px
Canonical $^{26}Al/^{27}Al_0$
$\Delta t_{canonical}$ = 240 000 y
$\delta^{26}Mg^*$ (‰)
Al/Mg
0.0
0.2
0.4
0.6
0.8
1.0
1.2
0.0
0.5
1.0
1.5
2.0
2.5
3.0

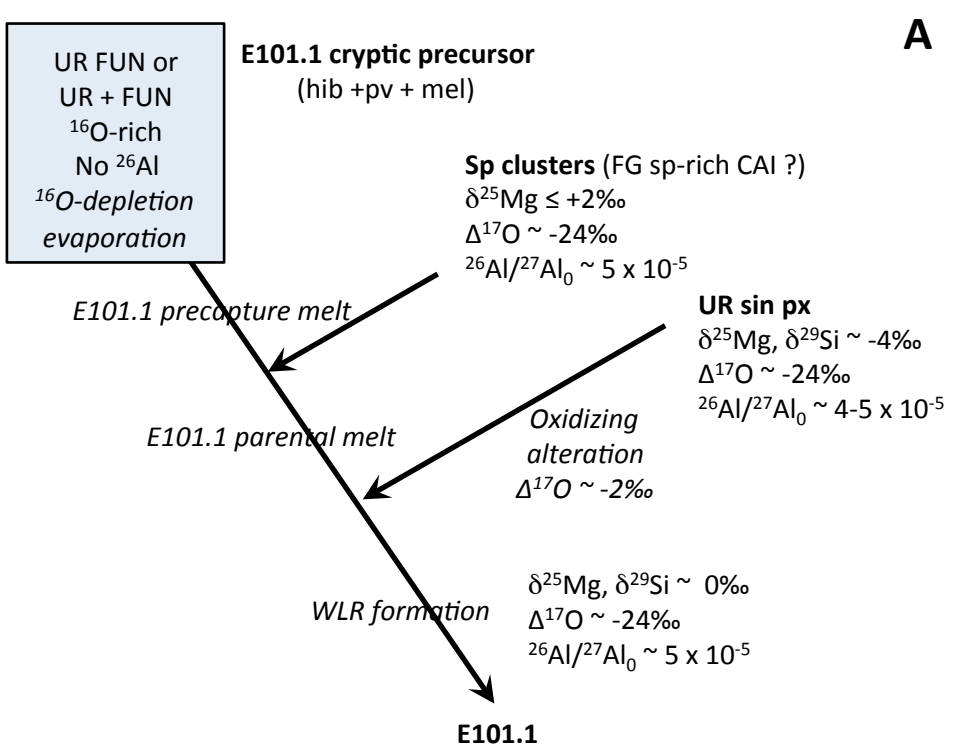
A
UR FUN or
UR + FUN
16O-rich
No 26Al
16O-depletion
evaporation
E101.1 cryptic precursor
(hib +pv + mel)
Sp clusters (FG sp-rich CAI ?)
δ25Mg ≤ +2‰
Δ17O ~ -24‰
26Al/27Al0 ~ 5 x 10-5
E101.1 precapture melt
UR sin px
δ25Mg, δ29Si ~ -4‰
Δ17O ~ -24‰
26Al/27Al0 ~ 4-5 x 10-5
E101.1 parental melt
Oxidizing
alteration
Δ17O ~ -2‰
δ25Mg, δ29Si ~ 0‰
Δ17O ~ -24‰
26Al/27Al0 ~ 5 x 10-5
WLR formation
E101.1

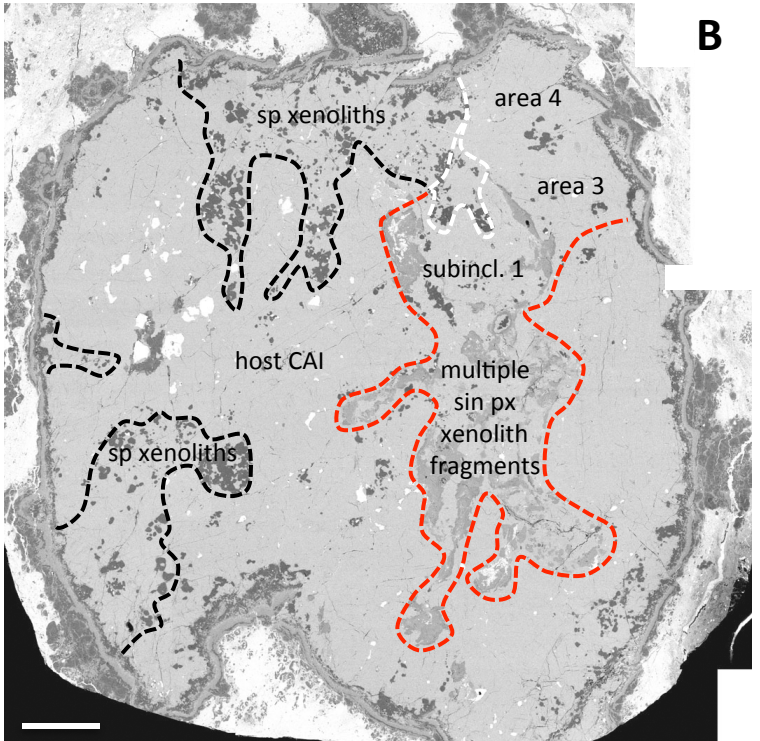
B
sp xenoliths
area 4
area 3
subincl. 1
host CAI
multiple
sin px
xenolith
fragments
sp xenoliths

Table 1: Abbreviations, types of pyroxene, lithological units and model endmembers discussed throughout the manuscript

Denomination	**Meaning**
Abbreviations	
AOA	Amoeboid Olivine Aggregate
AR	Accretionary Rim (forsterite-rich in E101.1)
WLR	Wark Lovering Rim
CAI	Ca-Al-rich Inclusion
UR	Ultra-Refractory
FUN	Fractionated with Unknown Nuclear effects
FG-sp-rich CAI	Fine-Grained spinel-rich CAI with nodular texture
CMAS	$CaO + MgO + Al_2O_3 + SiO_2$ chemical system
IMF	Instrumental Mass Fractionation
RSF	Relative Sensitivity Factor
Types of pyroxene	
WLR pyroxene	Ca-rich clinopyroxene with variable Al and Ti content ranging from very Al and Ti rich to pure diopside
Sinuous pyroxene	Al-diopside
Sc-Zr-rich pyroxene	Ca-rich clinopyroxene with elevated Al, Ti, Sc and Zr content and low SiO_2 content
Lithological units	
Sinuous pyroxene fragments	Sinuous fragments dominated by Al-diopside and locally containing FeO-rich assemblages
Clusters 1 to 7	Coarse-grained spinel clusters in the main host
Core	Central portion of the main host, mostly melilite
Profiles 1 and 2	Chemical and O, Mg, Si isotopic traverses started from the rim and directed towards the center of the inclusion, ~perpendicular to the surface
Areas 3 and 4	Regions between the sinuous pyroxene fragments and the rim, petrographically similar to those sampled by profile 1 and 2 but with different isotopic systematics
Subinclusions 1 and 2	Subcircular melilite + spinel regions nearly enclosed in sinuous pyroxene, proposed to be xenoliths in El Goresy et al. (2002)
Quenched glass	Regions with chemistry intermediate between melilite and pyroxene with Schlieren-like heterogeneities and dendritic melilite micro-crystals, located at the sinuous pyroxene - host melilite interface
Model endmembers	
Step 1 parental melt	Ideal CMAS composition required to match the observed composition of intermediate areas (3, 4 and subinclusion 1) upon mixing with sinuous pyroxene
Step 2 precapture melt	Ideal CMAS composition calculated from step 1 parental melt by substraction of condensate spinel
Step 3 preevaporation composition	Ideal CMAS composition calculated from step 2 precapture melt by correction for evaporation based on Mg and Si isotopes

Table 2 : Summary of O, Mg and Si isotopic analyses in E101.1 lithological units and minerals

	$\Delta^{17}O$ (‰)					$\delta^{25}Mg$ (‰)					$(^{26}Al/^{27}Al)_0$' [10^{-5}]**					*F*Si (‰)				
	#	min	max	wm	wm 2σ	#	min	max	wm	wm 2σ	#	min	max	wm	wm 2σ	#	min	max	wm	wm 2σ
Profile 1 Mel	13	-7.44	-1.86	-5.01	0.27	9	3.69	6.28	5.04	0.57	9	2.44	4.52	3.43	0.13	8	4.98	6.73	6.29	0.15
Profile 2 Mel	10	-9.32	-5.73	-6.93	0.31	10	1.88	6.91	5.06	0.55	10	2.91	4.97	3.95	0.11	9	5.16	6.56	5.66	0.13
Core Mel	3	-6.6	-5.12	-6.07	0.57	2	3.99	5.01	4.50	1.23	2	3.98	4.36	4.15	0.48	4	5.19	7.66	6.59	0.20
area 3 Mel	5	-10.18	-7.28	-8.64	0.43	5	0.88	2.01	1.43	0.47	5	2.83	4.09	3.70	0.11	1			1.24	
area 4 Mel	5	-9.59	-7.42	-8.03	0.4	5	0.54	2.15	1.49	0.47	5	3.91	5.39	4.71	0.11	3	2.8	3.53	3.25	0.25
sub 2 Mel	2	-17.45	-12.82	-15.14																
sub 1 Sp						3	-0.77	0.58	-0.02	0.48	3	4.53	5.84	5.04	0.37					
sub 1 Mel	6	-12.18	-7.8	-8.78	0.36	4	-1.51	1.06	-0.12	0.53	4	2.96	5.04	4.07	0.13	3	3.99	5.69	4.99	0.26
cluster 1 Sp	1			-22.83		3	6.42	6.70	6.53	0.51	3	4.93	5.72	5.30	0.89					
cluster 1 Mel*	2	-10.31	-3.68	-7.15	0.71	2	5.18	5.71	5.47	0.78	2	4.00	4.53	4.22	0.17					
cluster 2 Sp	1			-22.46		2	4.81	5.29	5.05	0.62	2	6.46	7.56	7.30	0.90					
cluster 2 Mel*	1			-6.14		2	5.02	5.77	5.40	0.75	2	3.62	3.90	3.77	0.18					
cluster 3 Sp						1			4.28		1			3.62						
cluster 3 Mel*						1			6.10		1			3.34						
cluster 4 Sp						1			6.63		1			5.30						
cluster 4 Mel*																				
cluster 5 Sp	1			-21.77		2	2.61	2.65	2.63	0.52	2	5.47	5.74	5.62	0.35					
cluster 5 Mel*	6	-11.25	-5.51	-7.33	0.43	2	3.65	6.09	4.87	0.75	2	4.07	4.57	4.32	0.20	2	5.6	5.83	5.71	0.31
Sin Px	7	-23.56	-18.53	-20.98	0.36	4	-4.65	-2.39	-3.40	0.31	4	4.42	13.20	5.21	1.28	3	-4.48	-2.37	-3.09	0.37
Sin Px - FeO	1			-4.65																
WLR all	13	-22.23	-15.29	-19.56	0.23	12	-1.50	3.04	0.50	0.19	12	3.68	6.54	4.78	0.24					
WLR Mel	4	-19.84	-16.81	-18.45	0.45															
WLR Ol	3	-22.23	-17.97	-20.35	0.49	1			-0.37											
WLR Px	4	-21.66	-15.29	-19.32	0.36	4	-1.22	3.04	0.86	0.25	4	4.95	6.54	5.16	0.99	8	-0.34	9.97	2.72	0.16
WLR Sp	2	-22.05	-20.88	-21.46	0.68	7	-1.5	1.25	0.19	0.32	7	3.70	5.70	4.76	0.25					
AR all	6	-22.41	-12.81	-19.00	0.35															
AR Fo	3	-22.41	-21.81	-22.18	0.49	5	-1.49	1.39	-0.02	0.25	5	0.01	0.09	0.06	0.04	4	-1.88	-0.46	-1.34	0.24
CAIs in AR†	3	-17.62	-12.81	-15.83	0.49															

* mel in close contact with sp cluster

** except AR Fo data given as δ^{26}Mg excess in ‰

† CAI-like nodules within the AR

number of analyses

abbreviations, min = minimum, max = maximum, wm = weighted mean, wm 2σ = 2 sigma uncertainty on the weighted mean, sub = subinclusion, sin = sinuous, Mel = melilite, Sp = spinel, Px = pyroxene, Ol = olivine, Fo = forsterite